



UNIVERSITY OF KRAGUJEVAC
FACULTY OF ENGINEERING

Vladimir Dunić

**DEVELOPMENT AND IMPLEMENTATION OF
THERMO-MECHANICAL CONSTITUTIVE MODEL FOR
NUMERICAL ANALYSIS OF SHAPE MEMORY ALLOYS**

Doctoral dissertation

Kragujevac, 2015

"The life give as back only what we gives to others."

Ivo Andrić

I Author
Name and surname: Vladimir Dunić
Date and place of birth: 09.12.1983., Pirot, Republic of Serbia
Current position: Research Associate, Faculty of Engineering, University of Kragujevac
II Doctoral dissertation
Title: Development and implementation of thermo-mechanical constitutive model for numerical analysis of shape memory alloys
Number of pages: 152
Number of figures: 67
Bibliographical data: 94
Institution and place: Faculty of Engineering, Kragujevac
Research field (UDK): Applied mechanics and software engineering [539.4:620.1]:519.6
Supervisor: dr Radovan Slavković, professor, Faculty of Engineering, Kragujevac
Co-supervisor: dr Elzbieta A. Pieczyska, assoc. professor, Institute of Fundamental Technological Research (IPPT), Polish Academy of Sciences (PAN), Warsaw, Poland
III Assessment and defense
Date of the PhD topic registering: 07.04.2014.
Number of the decision document and the date of the acceptance of doctoral dissertation: 01-1/2136-4, 10.07.2014.
Commission for assessing the eligibility of the candidate and the doctoral dissertation:
<ol style="list-style-type: none"> 1. dr Radovan Slavković, prof., Faculty of Engineering, Kragujevac 2. dr Elzbieta A. Pieczyska, assoc. prof., Institute of Fundamental Technological Research (IPPT), Polish Academy of Sciences (PAN), Warsaw 3. dr Miroslav Živković, prof., Faculty of Engineering, Kragujevac 4. dr Nenad Filipović, prof., Faculty of Engineering, Kragujevac 5. dr Aleksandar Sedmak, prof., Faculty of Mechanical Engineering, Belgrade 6. dr Nenad Grujović, prof., Faculty of Engineering, Kragujevac
Commission for assessing and defense of doctoral dissertation:
<ol style="list-style-type: none"> 1. dr Radovan Slavković, prof., Faculty of Engineering, Kragujevac 2. dr Elzbieta A. Pieczyska, assoc. prof., Institute of Fundamental Technological Research (IPPT), Polish Academy of Sciences (PAN), Warsaw 3. dr Miroslav Živković, prof., Faculty of Engineering, Kragujevac 4. dr Nenad Filipović, prof., Faculty of Engineering, Kragujevac 5. dr Aleksandar Sedmak, prof., Faculty of Mechanical Engineering, Belgrade 6. dr Nenad Grujović, prof., Faculty of Engineering, Kragujevac
Date of the doctoral dissertation defense:

DEVELOPMENT AND IMPLEMENTATION OF THERMO-MECHANICAL CONSTITUTIVE MODEL FOR NUMERICAL ANALYSIS OF SHAPE MEMORY ALLOYS

Abstract

Shape memory alloys (SMA) have wider and more frequent application in cases when it is useful to employ their advantages through specific behavior (pseudoelasticity and shape memory effect) in various conditions. As a side effect due to the high thermosensitivity, strong thermomechanical coupling occurs what increases the need for simulation of complex thermomechanical response in realistic problems. The complex stress states and deformation range impose the requirements for accurate analysis of large strain problems. The presented requirements are solved in several steps:

(1) Phenomenological constitutive SMA model (Lagoudas) has been reformulated by derivation of variables to depend on effective values of stress and strain and martensitic volume fraction. Gibbs free energy is reduced to scalar form what provides stress integration in the direction of deviatoric stress for forward transformation or total transformation strain for the reverse transformation.

(2) Simulation of SMA thermomechanical behavior is realized using partitioned approach by coupling of programs for structural analysis - PAK-S and heat transfer PAK-T. Dissipative energy of martensitic phase transformation imposes change of the material temperature as an internal heat source. As a communication interface between the PAK-S and PAK-T, Component Template Library (CTL) is used.

(3) Extension to the large strain problems is based on multiplicative decomposition of the deformation gradient to decompose deformation on elastic and inelastic part. Using the energy conjugated stress and strain measures, easy extension of the algorithm for small strain is provided to solve complex stress states for large strains.

(4) Experimental investigation of TiNi SMA samples under various loading rates is used for verification of thermo-mechanical coupling. Numerical simulation of initiation, development and saturation of the martensitic phase transformation under various loading rates is compared to experimental results to show qualitative and quantitative accuracy of such approach. Extension to large strain problems is realized using the logarithmic strain. Simulation of the chosen examples from literature, the functionality and accuracy of the presented approach is verified.

РАЗВОЈ И ИМПЛЕМЕНТАЦИЈА ТЕРМО-МЕХАНИЧКОГ КОНСТИТУТИВНОГ МОДЕЛА ЗА НУМЕРИЧКУ АНАЛИЗУ ПОНАШАЊА МАТЕРИЈАЛА СА СВОЈСТВОМ ПАМЋЕЊА ОБЛИКА

Сажетак

Материјали са својством памћења облика (енг. Shape Memory Alloys - SMA) налазе све већу и чешћу примену у случајевима када је погодно искористити предности које они пружају кроз своје специфично понашање (псеудоеластичност и ефекат памћења облика) у различитим условима. Као пратећи ефекат, због високе термо-осетљивости јавља се јака термомеханичка спрега што указује на потребу за симулацијом комплексног термомеханичког одзива код реалних проблема. Појава комплексних напонских стања и опсег деформација намеће захтев за тачно решавање проблема великих деформација.

Предочени захтеви су решени у неколико корака:

(1) Феноменолошки конститутивни SMA модел (Лагоудас) је реформулисан извођењем променљивих да зависе од ефективних вредности напона и деформације и удела мартензита у запремини. Гипсова слободна енергија је сведена на скаларни облик чиме је омогућена интеграција напона у правцу девијатора напона за трансформацију унапред, односно укупне деформације трансформације за трансформацију уназад.

(2) Симулација термомеханичког понашања SMA је изведена коришћењем партиционисаног приступа спрезању за повезивање програма за структурну анализу ПАК-С и пренос топлоте ПАК-Т. Дисипативна енергија мартензитне фазне трансформације изазива промену температуре материјала у форми унутрашњег топлотног извора. Као комуникациони интерфејс између програма ПАК-С и ПАК-Т, коришћена је библиотека шаблона за компоненте (Component Template Library - CTL).

(3) Проширење на проблеме великих деформација је базирано на мултипликативној декомпозицији градијента деформације, чиме је деформација раздвојена на еластичну и нееластичну. Коришћењем енергетски конјугованих мера напона и деформације, омогућено је једноставно проширење алгоритма за мале деформације за решавање комплексних напонских стања код великих дефор-

мација.

(4) Експериментално испитивање TiNi SMA узорака за различите брзине оптерећења је употребљено за верификацију термо-механичке спреге. Нумеричка симулација појаве, развоја и засићења мартензитне трансформације за различите брзине оптерећења је поређена са експериментима, чиме је приказана квалитативна и квантитативна тачност оваквог приступа. Проширење на проблеме великих деформација је реализовано коришћењем логаритамске деформације. Применом на одабраним примерима из литературе, верификована је функционалност и тачност такве имплементације.

Acknowledgement

"People who underestimate the teachers work are worthless."

Dositej Obradović

Doctoral dissertation, as the crown of the doctoral study research, is the result achieved by all knowledge acquired during the education and life. At this moment, I would like to thanks to the most important persons and organizations which helped in the achieving of the results.

The biggest gratefulness, I own to my supervisor, Prof. Radovan Slavković, who helped me during my education, by expertise, active engagement and useful professional and life advice, to acquire knowledges and skills necessary for quality reasearch work. Also, expertise and knowledge acquired during the work with Prof. Mirsolav Živković are also very important for successful realization of objectives. Practical advices of Prof. Nenad Grujović, have contributed to a more rational approach to problems and the research work made more pragmatic and efficient.

Cooperation with cosupervisor, Prof. Elzbieta Pieczyska, from the Institute for Fundamental Technological Research, Polish Academy of Sciences (IPPT, PAN), in the framework of KMM-VIN scholarship during the 2013th, is of great importance for the acquired knowledge in the field of experimental investigation of materials. Also, hers commitment and energy, identified during the work with Prof. Pieczyska, have been significant factor for the quality processing and publication of achieved results. Also, I would like to thanks to Prof. Nenad Filipović, Такође бих се захвалио Проф. Ненаду Филиповићу, for support during the studies and participation in KMM-VIN program.

Ministry of Science and Technological Development, Republic of Serbia, has supported my research work in various forms: at the beginning of doctoral studies by scholarship for the best PhD students, later by employment as research associate in the framework of Ministry national projects, by support for participation at conferences and joint international project of Ministry and DAAD. The specific results

presented in the dissertation are the results of active projects: "Development of software for analysis of coupled multiphysics problems" TR32036, and "Application of Biomedical Engineering in Preclinical and Clinical Practice," III41007, and also finished Ministry of Science and DAAD project - "Solving of multiphysics problems using software PAK - SOMUPAK", 2012-2013.

Also, I would like to stress importance of good cooperation with the colleagues at Engineering Software Laboratory, which selflessly helped me during the research by their experience and knowledge, and also by pleasant atmosphere and time spent together having fun.

At the end, I would like to emphasize the biggest thankfulness to my loved ones, ancestors and descendants, for the unconditional support, love and knowledge throughout life and work.

Vladimir Dunić

In Kragujevac,

March 2015.

Contents

List of Figures	12
List of Tables	16
Acronyms	17
List of Symbols	18
1 Introduction	24
1.1 Motivation, goal and structure	24
1.2 About properties, experimental investigation and modeling of Shape Memory Alloys	26
1.3 Application of SMA	32
1.3.1 Medical application	33
1.3.2 Technical application	37
2 Review and analysis of existing approaches to SMA modeling	42
2.1 SMA constitutive modeling approaches	42
2.2 Review of existing SMA models	43
2.3 Research topics and outline of the dissertation	47
3 Improved constitutive model for the analysis of SMA	49
3.1 Kinematics	50
3.1.1 Deformation gradient	50
3.1.2 Polar decomposition of deformation gradient	50
3.1.3 Deformation and strain tensors	52
3.1.4 Generalized strain measure	52
3.1.5 Rates of deformation tensors	53
3.1.6 Objective corotational rates	55
3.1.7 Elastic and inelastic deformation	56
3.1.8 Stress tensors	61

<i>CONTENTS</i>	10
3.1.9 Balance of mechanical energy	63
3.2 Continuum thermodynamics	64
3.2.1 The First law of thermodynamics (Balance of Energy)	64
3.2.2 The Second law of thermodynamics (Entropy inequality principle)	64
3.3 Free energy	66
3.4 SMA constitutive model - Lagoudas	68
3.5 Evolution of the transformation function	70
3.6 Hardening functions	72
4 Numerical implementation of SMA stress integration procedure	75
4.1 Basic assumptions	75
4.2 Local Newton-Raphson algorithm	76
4.3 Stress integration for small strains	77
4.4 Stress integration for large strains	79
5 Thermo-mechanical coupling of structural and heat transfer analysis in SMA	83
5.1 Coupled energy balance equation	83
5.2 Thermomechanical coupling and methods	84
5.2.1 Heat transfer program - PAK-T	85
5.2.2 Structure analysis program - PAK-S	88
5.3 Implementation of partitioned coupling algorithm	91
5.3.1 Mathematical description	91
5.3.2 Implementation	93
6 Verification of coupled thermo-mechanical model by comparison to experimental results	95
6.1 Experimental details of SMA tension tests	95
6.2 Description of FEM model	98
6.3 Experimental and numerical results	99
6.3.1 Strain-controlled tension loading: experimental and numerical results	100
6.3.2 Force-controlled tension loading: experimental and numerical results	101
6.4 Discussion of verification results	106

7 Numerical analysis of problems and modeling of real SMA structures	114
7.1 Numerical analysis of benchmark examples	114
7.1.1 Uniaxial tension loading	114
7.1.2 Multiaxial loading	118
7.2 Large strain examples	124
7.2.1 Simple shear with superposed rigid rotation	124
7.2.2 Cantilever beam with moment at free end	125
7.2.3 Stent unit cell	127
8 Conclusions	135
Bibliography	140
Appendix A Time integration procedure	150

List of Figures

1.1	Scheme of stress-temperature phase diagram for Shape Memory Alloys (SMA)	27
1.2	Temperature-induced phase transformation of SMA	27
1.3	Schematic of the shape memory effect of SMA	29
1.4	Stress-strain-temperature curves of Shape Memory Effect (SME) . . .	29
1.5	Scheme of pseudoelastic loading path of SMA	30
1.6	DSC - curves obtained for two complete heating - cooling runs	30
1.7	Scheme of interface between the austenite and martensite phases . . .	31
1.8	Temperature distribution on the SMA sample surface and temperature profile along the line (specimen length) at the start of the localised martensitic transformation	31
1.9	Orthodontic applications of SMA: Nitinol brace used for alignment purposes in dental practice	33
1.10	Orthodontic applications of SMA: Scheme of NiTi drill used for root canal surgery.	34
1.11	Periodontal SMA implant	34
1.12	Intramedullary NiTi nail for ankle surgery	35
1.13	A self-expanding NiTiNOL stent shown in the relaxed configuration (above) and constrained state (below)	36
1.14	Staple used for bone fixation after the foot surgery	37
1.15	Urethral Stent (a) Picture of the stent, Made of a Nitinol Framework with a Polymeric Coating (b) Representation of an implanted urethral stent (Allium Medical Ltd., Caesarea Industrial Park South, Israel) .	38
1.16	Scheme of SMA connectors for pipe couplings	38
1.17	A concrete beam reinforced with superelastic stranded cables via the method of post-tensioning	39
1.18	Four cables of 45 m long in ELSA (European Laboratory for Structural Assessment). (A) cable; (B) SMA dumper; (C) accelerometer .	40

3.1	Scheme of deformation presented by polar decomposition	51
3.2	Scheme of multiplicative decomposition of the deformation gradient .	58
3.3	Scheme of Cauchy-Green strain tensors in corresponding configurations	59
3.4	Scheme of strain tensors and configurations	61
3.5	Scheme of compatible strain tensors and configurations.	62
5.1	Thermo-mechanical coupling scheme using Component Template Library (CTL) interface	94
6.1	Transmission Electron Microscopy (TEM) image of the TiNi SMA reference state (courtesy of Danuta Stroz)	96
6.2	Scheme of experimental set-up designed for thermomechanical investigation of SMA (GL denotes gauge length of the testing machine extensometer)	96
6.3	Photographs of experimental set-up designed for thermomechanical investigation of SMA	97
6.4	Example of the FEM mesh with boundary and loading conditions for tension tests	98
6.5	Comparison of true stress vs. true strain and temperature change vs. strain curves for TiNi SMA during tension at strain rate 10^{-3}s^{-1} . . .	101
6.6	Comparison of true stress vs. true strain and temperature change vs. strain curves for TiNi SMA during tension at strain rate 10^{-2}s^{-1} . . .	102
6.7	Comparison of true stress vs. true strain and temperature change vs. strain curves for TiNi SMA during tension at strain rate 10^{-1}s^{-1} . . .	103
6.8	Comparison of true stress vs. true strain and temperature change vs. strain curves for TiNi SMA during tension at stress rate 12.5 MPa/s .	104
6.9	Comparison of true stress vs. true strain and temperature change vs. strain curves for TiNi SMA during tension at stress rate 25 MPa/s . .	105
6.10	Comparison of true stress vs. true strain and temperature change vs. strain curves for TiNi SMA during tension at stress rate 50 MPa/s . .	106
6.11	Comparison of experimental curves obtained during TiNi SMA tension at strain rates 10^{-1}s^{-1} , 10^{-2}s^{-1} and 10^{-3}s^{-1}	107
6.12	Comparison of numerical curves obtained during TiNi SMA tension at strain rates 10^{-1}s^{-1} , 10^{-2}s^{-1} and 10^{-3}s^{-1}	108
6.13	Comparison of experimental curves obtained during TiNi SMA tension at stress rates 12.5 MPa/s, 25 MPa/s and 50 MPa/s	109
6.14	Comparison of numerical curves obtained during TiNi SMA tension at stress rates 12.5 MPa/s, 25 MPa/s and 50 MPa/s	110

6.15	Experimental results. Comparison of strain and temperature change versus time curves for TiNi SMA during tension at (a) stress rate 25 MPa/s and (b) strain rate 10^{-2}s^{-1}	112
6.16	Numerical results. Comparison of strain and temperature change versus time curves obtained for TiNi SMA during tension at (a) stress rate 25 MPa/s and (b) strain rate 10^{-2}s^{-1}	113
7.1	The FEM mesh with boundary and loading conditions for uniaxial tension loading examples	115
7.2	Comparison of stress-strain diagrams presenting the SMA pseudoelasticity effect	116
7.3	Comparison of smooth hardening function to the polynomial and cosine for SMA pseudoelasticity effect	117
7.4	Stress-strain diagrams presenting SMA shape memory effect	117
7.5	Comparison of smooth hardening function to the polynomial and cosine for SME	118
7.6	Temperature-induced martensite transformation in SMA	119
7.7	Comparison of smooth hardening function to the polynomial and cosine for the temperature-induced martensite transformation	119
7.8	Stress path in proportional loading	120
7.9	Tension and shear stress-strain diagrams for proportional loading	121
7.10	Axial-shear strain diagrams for proportional loading	121
7.11	Axial stress vs. shear stress diagram presenting non-proportional loading	122
7.12	Axial strain vs. shear strain diagram presenting non-proportional loading	123
7.13	Axial stress vs. strain diagram presenting non-proportional loading	123
7.14	Shear stress vs. strain diagram for non-proportional loading	124
7.15	Representative positions of simple shear loading example with superposed rigid rotation	125
7.16	Comparison of results obtained for SMA shear with superposed rotation against shear with no superposed rotation	126
7.17	Scheme of cantilever beam subjected to end moment	126
7.18	Force – displacement dependence at the loaded SMA cantilever end	127
7.19	Stress distribution along the cantilever length and martensitic volume fraction in chosen steps during the loading	128
7.20	Stress distribution along the cantilever length and martensitic volume fraction in chosen steps during the unloading	129

7.21	Specimen geometry for a stent unit cell of thickness 0.53 mm	130
7.22	Undeformed mesh of one-quarter of the tested stent unit cell	131
7.23	Одзив сила-померање добијена Finite Element Method (FEM) анализом јединичне ћелије стента под псеудоеластичним условом	131
7.24	Contours of martensite volume fraction within the stent unit cell without thermo-mechanical coupling	132
7.25	Temperature field of stent unit cell at initial state	133
7.26	Temperature field of stent unit cell at maximal loading	133
7.27	Temperature field of stent unit cell at unloaded state	134

List of Tables

3.1	Legendre transformation between the thermodynamic potentials . . .	67
4.1	Proposed algorithm for decision about transformation direction . . .	77
4.2	Newton-Raphson algorithm for SMA constitutive model	78
5.1	Classification of nonlinear analysis	90
6.1	Material parameters of SMA in stress- and strain- controlled tension tests in Section 6	99
7.1	Material parameters of SMA used in uniaxial loading examples	115
7.2	Material parameters of CuAlZnMn alloy used in multiaxial loading examples	120
7.3	Material parameters of SMA for stent unit cell	130

Acronyms

AIT Aichi Institute of Technology

CTL Component Template Library

DSC Differential Scanning Calorimetry

FEM Finite Element Method

IFTR Institute of Fundamental Technological Research (pol. Instytut Podstawowych Problemow Techniki - IPPT)

MPI Message Passing Interface

NOL Naval Ordnance Laboratory

PAK Program za Analizu Konstrukcija, in serbian

PAS Polish Academy of Sciences (pol. Polskiej Akademii Nauk - PAN)

PE Pseudoelasticity

SIMT Stress Induced Martensitic Transformation

SMA Shape Memory Alloys

SME Shape Memory Effect

SSH Secure Shell

TCP/IP Transmission Control Protocol and Internet Protocol

TEM Transmission Electron Microscopy

ULH updated-Lagrangian-Hencky

List of Symbols

A_f austenitic finish temperature

A_s austenitic start temperature

E Young modulus

G shear modulus

H maximal effective transformation strain

J volume ratio

K^c convection matrix

K^k conduction matrix

K^r radiation matrix

M_f martensitic finish temperature

M_s martensitic start temperature

T^J nodal temperatures

T_0 reference temperature

T current temperature

V volume in base configuration

Y threshold value of transformation function

Γ total production of entropy per unit time

Ω boundary surface

Φ transformation function

- Π thermodynamic force
- α effective thermal expansion coefficient
- Σ Mandel stress tensor
- $\boldsymbol{\alpha}$ thermal expansion tensor
- $\boldsymbol{\chi}$ motion of the body
- \mathbb{H} fourth-order elasticity tensor
- $\boldsymbol{\sigma}_u$ corotated Cauchy stress tensor (Green-Naghdi)
- $\boldsymbol{\sigma}$ Cauchy stress tensor
- $\boldsymbol{\tau}$ Kirchhoff stress tensor
- $\boldsymbol{\varepsilon}$ deformation tensor
- ζ set of internal state variables
- \boldsymbol{n}_{tr} direction of transformation strain
- \dot{x} velocity
- λ_k principal stretches
- \mathbf{B} matrix of the derivative of the interpolation function
- \mathbf{C}_{el} elastic constitutive matrix
- \mathbf{C} right Cauchy-Green deformation tensor
- \mathbf{E} Green-Lagrange strain tensor
- \mathbf{F}^E elastic deformation gradient
- \mathbf{F}^{IN} inelastic deformation gradient
- \mathbf{F}_{int} internal forces
- \mathbf{F} deformation gradient
- \mathbf{G} material metric tensor
- \mathbf{H}_{int} interpolation functions matrix

- H** right Hencky strain
- K** stiffness matrix
- P** Piola stress tensor
- R** rotation tensor
- S'** deviatoric stress tensor
- S** the second Piola-Kirchhoff stress tensor
- T_B** Biot stress tensor
- T** temperature gradient
- U** right stretch tensor
- V** (**X**, *t*) material description of the velocity field
- X** position vector in reference configuration
- Ω** anti-symmetric spin tensor
- b^E** elastic left Cauchy-Green deformation tensor
- b** left Cauchy-Green deformation tensor
- e'** deviatoric strain tensor
- e_{EA}** Euler-Almansi strain tensor
- e_{tr}** transformation strain
- e** total strain tensor
- g** spatial metric tensor
- h^E** left elastic Hencky strain
- h** left Hencky strain
- k** material's conductivity tensor
- l** spatial velocity gradient
- p_k** principal directions of base configuration

- \mathbf{q}_k principal directions of "unrotated" configuration
- \mathbf{q} heat flux
- \mathbf{r}_s external body load
- \mathbf{u}_n displacement of node vector
- \mathbf{u}_p displacement of material point vector
- $\mathbf{v}(\mathbf{x}, t)$ spatial description of the velocity field
- \mathbf{v} left stretch tensor
- \mathbf{x}_n position vector of node
- \mathbf{x}_p position vector of material point
- \mathbf{x} position vector in current configuration
- \mathcal{K} kinetic energy
- \mathcal{M} effective compliance tensor
- \mathcal{P}_{ext} external mechanical work
- \mathcal{P}_{int} internal mechanical work
- \mathcal{Q} thermal work
- \mathcal{S} entropy possessed by a continuum body occupying a certain region
- \mathcal{U} internal energy
- ν Poisson's ratio
- ω angular velocity
- $\bar{\mathbf{S}}$ effective stress
- $\bar{\mathbf{C}}^E$ elastic right Cauchy-Green deformation tensor
- $\bar{\mathbf{G}}$ intermediate metric tensor
- $\bar{\mathbf{H}}^E$ right elastic Hencky strain
- $\bar{\mathbf{b}}^{IN}$ inelastic left Cauchy-Green deformation tensor

- $\bar{\mathbf{h}}^{-IN}$ left inelastic Hencky strain
- \bar{e}_{tr} effective transformation strain
- ρ density
- σ_m mean stress
- $\tilde{\mathbf{h}}$ Cauchy entropy flux
- \tilde{Q} rate of entropy input
- \tilde{r} entropy sources per unit time and per unit current volume
- ξ martensitic volume fraction
- b_k principal stretches of the left Cauchy-Green deformation tensor
- c_k principal stretches of the right Cauchy-Green deformation tensor
- c_m bulk modulus
- c effective specific heat
- $d\mathbf{X}$ line element in base configuration
- $d\mathbf{x}$ line element in current configuration
- ds infinitesimal surface elements
- $f(\xi)$ hardening functions
- g Gibbs free energy
- h_I weight functions
- h_J interpolation functions
- h enthalpy
- q_S heat flux input on part of the surface
- q_c convective flux
- q_n total heat flux on the surface boundary
- q_r radiative flux

q_{dis} elementary dissipative energy

q heat source

s_0 effective specific entropy

s entropy per unit current volume

u_0 effective specific internal energy

u specific internal energy

v volume in current configuration

w_{int} rate of internal mechanical work per unit reference volume

\mathbf{C}^{IN} inelastic right Cauchy-Green deformation tensor

\mathbf{H}^{IN} right inelastic Hencky strain

\mathbf{n} outward unit normals to the infinitesimal surface elements ds

\mathcal{D}_{int} dissipation of the internal energy

ψ Helmholtz free energy

e_m mean strain

e_{th} thermal strain

Chapter 1

Introduction

1.1 Motivation, goal and structure

During the last several decades Shape Memory Alloys (SMA) have become fascinating materials for researchers and engineers [1]. The reason is possibility to use the advanced properties and effects in industrial applications and various engineering solutions [2]. It is of high importance to understand mechanism of SMA phenomenological effects in order to investigate the material behavior of such materials. Depending on temperature of the SMA during the exploitation, the possible effects could be different for the same material. That makes the alloys multifunctional and very sensitive to the temperature change. The SMA phenomenological effects, thermo-mechanical behavior, properties and some application are discussed in details in [3].

Their high thermal sensitivity can be used as advantage by employing the effects of shape memory in a proper way, if the material properties are known [1,2]. Experimental investigation gives a lot of details about the SMA behavior, but a correct numerical analysis is always useful because the results can predict the exploitation problems and possible damage. Furthermore, the SMA behavior is caused by complex thermo-mechanical state what makes constitutive modeling more challenging.

During the last decades, many researchers all around the world are trying to improve the established procedures for experimental and numerical investigation of SMA with idea to provide more reliable data necessary for correct prediction of the material behavior. In this scope, the thesis concern reformulation and implementation of thermo-mechanical constitutive model for numerical analysis of SMA and its successful application.

Structure of the theses is as follows:

In Chapter 1 - introduction is given in a form of short description of SMA properties and effect described in diagrams and figures. The phenomenological effects, thermo-mechanical behavior, properties and application of SMA are introduced.

In Chapter 2, a review of the existing constitutive models have been discussed. The details about the SMA modeling approaches and the already established numerical procedures are analyzed and compared. A special case of thermo-mechanical experimental research and constitutive models capable to catch the SMA phenomena are discussed. The review of previous works has defined the demands and direction of research.

In Chapter 3, the details about the constitutive SMA modeling are presented. Continuum mechanics and thermodynamic principles provide the base for the correct implementation of the free energy function. The details necessary for proper definition of various strain measures along with the conjugated stress measures for the large strain theory are presented to ensure the extension of the small strain algorithm to large strain problems.

Chapter 4, concerns the details about the implementation of the stress integration procedure which ensures the previously presented theory to be easy incorporated into the Finite Element Method (FEM) program.

In Chapter 5, the algorithm for the partitioned thermo-mechanical coupling of the structural and heat transfer FEM program is presented with a details of implementation.

In Chapter 6, the verification of the coupling algorithm is performed by the comparison of numerical simulation to the results obtained by experimental testing of the SMA. The curves of the stress and temperature change versus strain dependence are presented for the various stress and strain rates. The tests are carried out by the force and the displacement control what influences some differences in the SMA behavior analyzed in this chapter.

In Chapter 7, firstly benchmark examples are defined as control tests of the implemented stress integration procedure. For the uniaxial loading examples the comparison to the literature results is presented. The investigation is extended by several multiaxial loading tests in order to examine functionality of the presented procedure. The successful application of the presented theory is given on the selected realistic SMA problems.

In Chapter 8, final remarks and conclusions noted during the research are presented. Further directions for the research and current challenges in this field are introduced.

Finally, at the end, literature overview is given. Also, one appendix describ-

ing the stress integration procedure presents the algorithm implemented into the structure analysis program.

1.2 About properties, experimental investigation and modeling of Shape Memory Alloys

Due to very advanced characteristics, the SMA belong to the specific group of multifunctional or smart materials with specific requirements, functionality and limitations. The SMA have a possibility to recover the shape and geometry at the specific material temperature. The maximal inelastic deformations registered during the exploitation depend on the SMA kind and can be near 10% of strain. The capability of sensing (conversion of mechanical signal into non-mechanical) and actuation (conversion of non-mechanical signal into mechanical) and possibility to use those properties simultaneously, classified such materials in a special subgroup of active or responsive materials [3].

During the investigation of steel phases and its microstructures, a several phases are noticed as possible, such as austenite and martensite. The martensite phase got the name in honor of German metallurgist Adolf Martens (1850-1914), who investigated phase change in steel [1, 4]. The martensitic transformation is defined as the phase transformation which occurs by moving of atoms as shear mechanism [4] without diffusion of atoms [5]. In the beginning, the martensite transformation in steels was observed as irreversible. Buehler et al. [6] investigated in 1963, the reversibility of the martensitic transformation in NiTi alloy and its influence on the mechanical properties. They have found that the main factors which control the phase transformation are "alloy composition, temperature and mode of plastic deformation". The research was conducted at the Naval Ordnance Laboratory (NOL), so the NiTi alloy got the name NiTiNOL in that honor. A few years later, Buehler and Wiley were awarded a patent for the development of the NiTi alloy series [7].

During the further research, it was also found that [1–3, 6, 7]:

- NiTi alloy contains 49–57% nickel and the ideal composition of NiTiNOL can only vary between 38% and 50% titanium by weight,
- the alloying elements such as Co or Fe added to NiTi causes decrease of transformation temperatures,
- there are High Temperature SMA (TiPd, TiPt, TiAu) with transformation temperatures above 100 °C,

- alloying element Cu makes stress hysteresis much narrower.

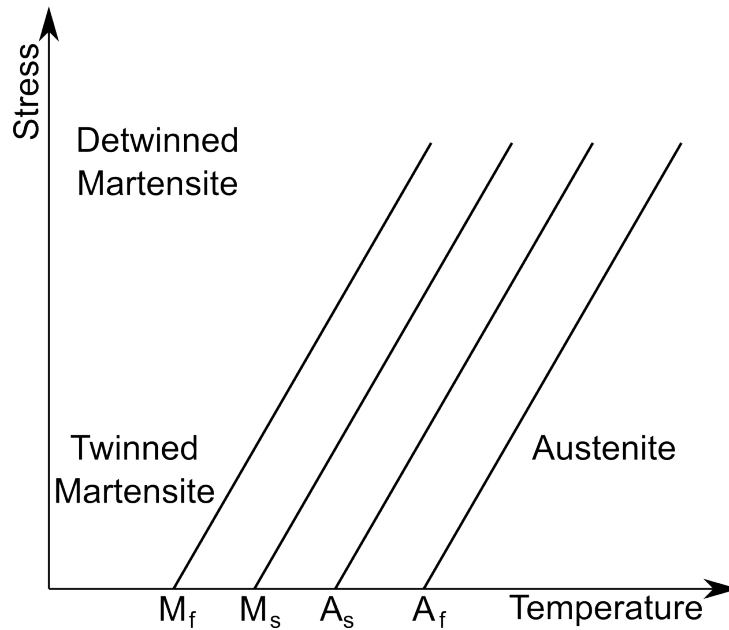


Figure 1.1: Scheme of stress-temperature phase diagram for SMA: M_s - martensite start, M_f - martensite finish, A_s - austenite start, A_f - austenite finish [3]

The concentration of the phases is an important factor for the alloy behavior (Figure 1.1). The phases ratio can be controlled by various external factors described by variables such as: stress, temperature, concentration, magnetic field, etc. In this sense, the SMA can be observed in two possible phases with different crystal lattice: austenite (A) and martensite (M). The austenite is a phase available at high temperatures, while the martensite belongs to the low temperature phase. The transformation between the phases occurs by shear lattice distortion i.e. homogeneous slip of the neighboring planes and the corresponding changes in the distance between the planes [5]. The orientation direction of each crystal is called a variant. Martensitic variants can be organized as a twinned (combination of martensitic variants) and a detwinned martensite (specific variant is dominant) [3].

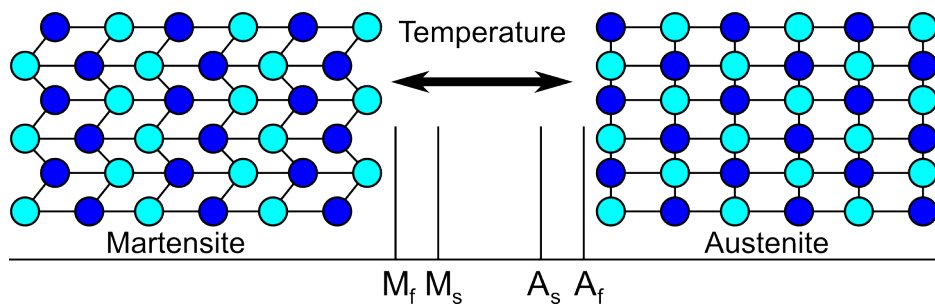


Figure 1.2: Temperature-induced phase transformation of SMA [3]

A temperature change of the SMA material causes the transformation of the crystal lattice (Figure 1.2). Cooling of the material induces the forward martensitic transformation, which includes changes of the crystal lattice from austenite to twinned martensite. Heating of the material causes the reverse martensitic transformation from martensite to austenite. The start and finish temperatures are of great importance for martensitic transformation. The martensite and austenite temperature are denote by M and A and start and finish points are defines by indices "s" and "f" (from start and finish, respectively). During the both direction of transformation, there are two characteristic temperatures when the transformation is initiated and is completed (martensitic start M_s and finish M_f and austenitic start A_s and finish A_f temperature) [3].

A mechanical loading can also change the crystal lattice. If the load is applied at the low temperature (twinned martensite), some variants can be reoriented and detwinned what causes material shape change (Figure 1.3). By heating above the austenitic finish temperature A_f reverse phase transformation occurs and the crystal lattice transforms from the detwinned martensite to the austenite (Figure 1.3). After cooling below martensitic finish temperature M_f the twinned martensite is formed again. This effect is known as Shape Memory Effect (SME) or pseudoplasticity (Figure 1.4). If the material temperature is above the austenitic finish temperature A_f , the loading induces the transformation to detwinned martensite from the stable austenite, which exists at that temperature. After unloading, the crystal lattice structure is returned to the austenitic phase (Figure 1.5). This effect is known as Pseudoelasticity (PE) [1–3].

Crystal structure of austenite is cubic crystal $B2$, while martensite can have different structures what depends on alloying elements. In NiTi alloys, martensitic phase has monoclinic $B19'$ structure. Direct transformation $B2 \rightarrow B19'$ is not so often because, frequently, there is martensitic R -phase ($B2 \rightarrow R \rightarrow B19'$). For example, by addition of Cu or Pd the martensite can form orthorhombic $B19$ structure or R -phase [3, 4].

Using the Differential Scanning Calorimetry (DSC) is possible to determined martensitic temperatures (start and finish) for forward and reverse transformation during heating and cooling of the material. As it can be noticed in Figure 1.6, cooling curve shows that the R -phase transition starts at $\approx 283K$ and a single, wide peak is visible on the curve [8].

The martensitic transformation occurs by moving of atoms (lattice shearing) along a specific plane called habit plane or lattice invariant plane which forms interface between the martensite and austenite [3, 9]. There are two lattice invariant shear

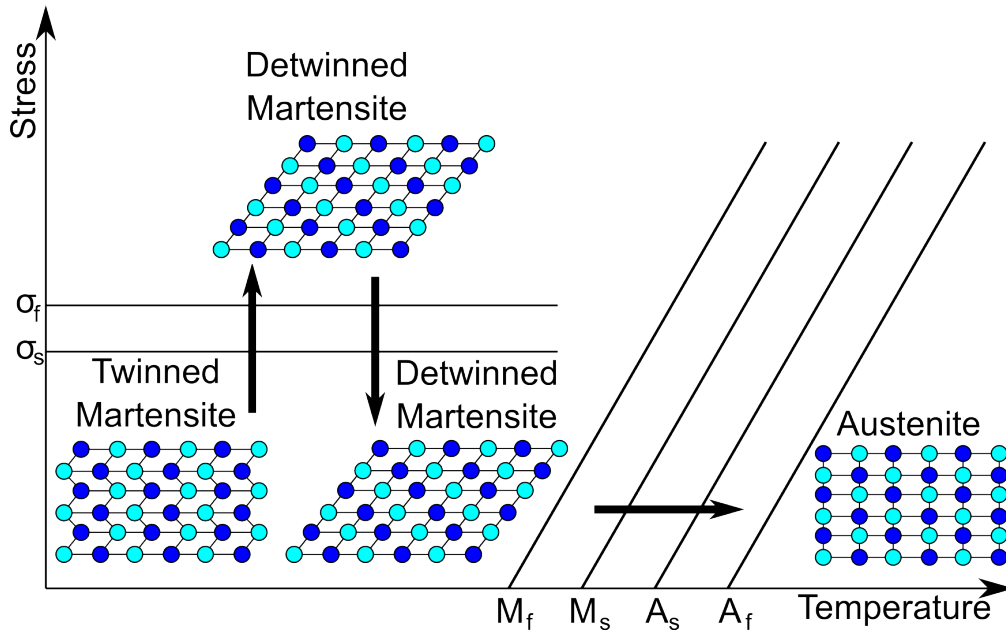


Figure 1.3: Schematic of the shape memory effect of SMA [3]

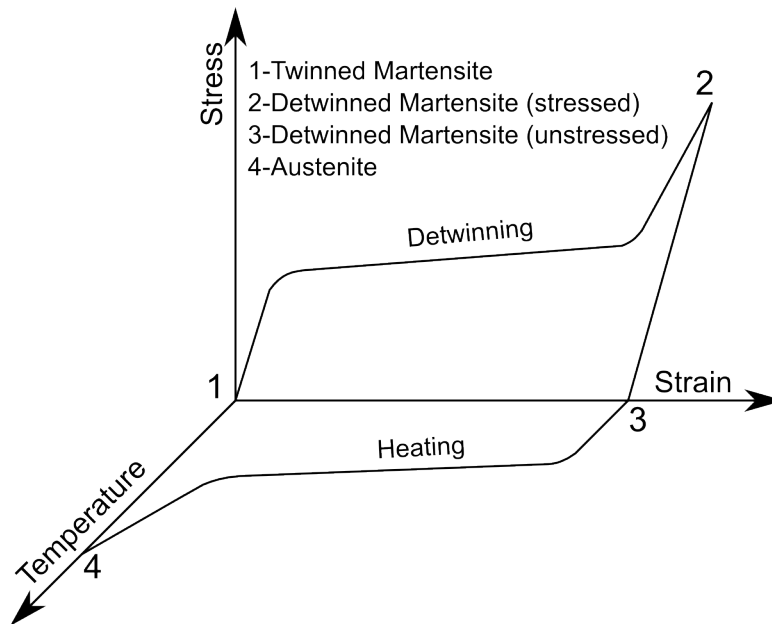


Figure 1.4: Stress-strain-temperature curves of SME [3]

mechanisms: slip and twinning. In SMA, the twinning is more often mechanism. The details are given in Figure 1.7.

Also, as it was observed by Shaw and Kyriakides and Hallai and Kyriakides in [10,11], the forward and reverse martensitic transformation did not occur homogeneously in the specimens. The transformation occurs by nucleation and propagation of fronts due to exothermic nature for transformation from austenite to martensite and endothermic nature for transformation from martensite to austenite. Those

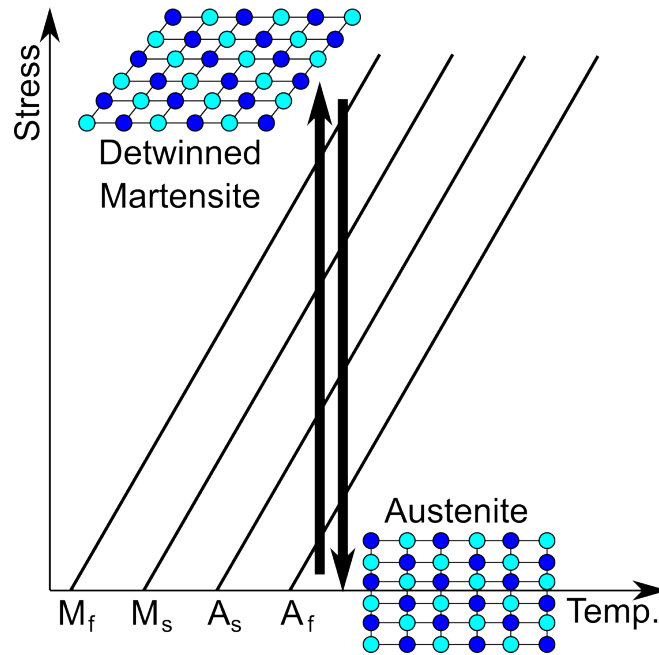


Figure 1.5: Scheme of pseudoelastic loading path of SMA [3]

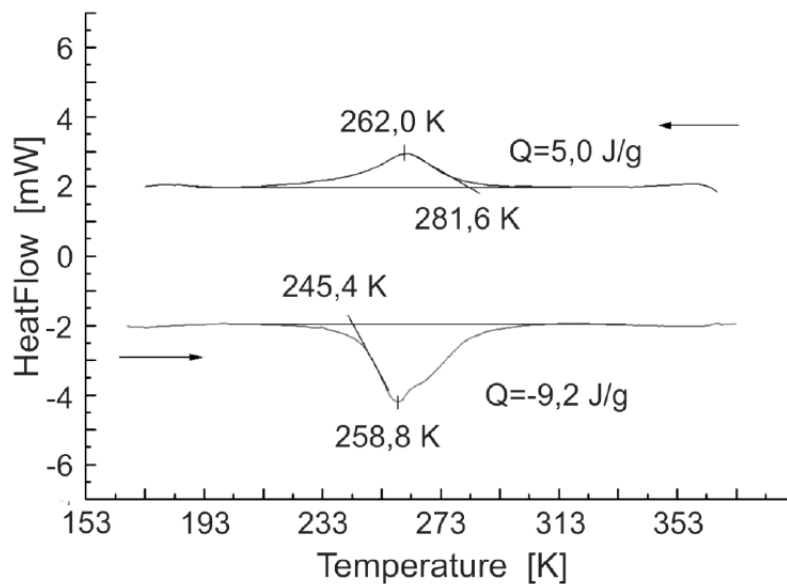


Figure 1.6: DSC - curves obtained for two complete heating - cooling runs (courtesy of Danuta Stroz, University of Silesia, Poland) [8]

fronts are developing in form of bands similar to observed in mild steel "Lüders bands". Pieczyska et al. recorded by infrared camera two directions of the transformation bands accompanying pseudoelastic TiNi SMA deformation [8, 12–14]. The temperature difference between the bands and the other material (Figure 1.8) has been investigated by Pieczyska et al. in [15].

The experimental results of TiNi SMA subjected to tension in [8] were extended

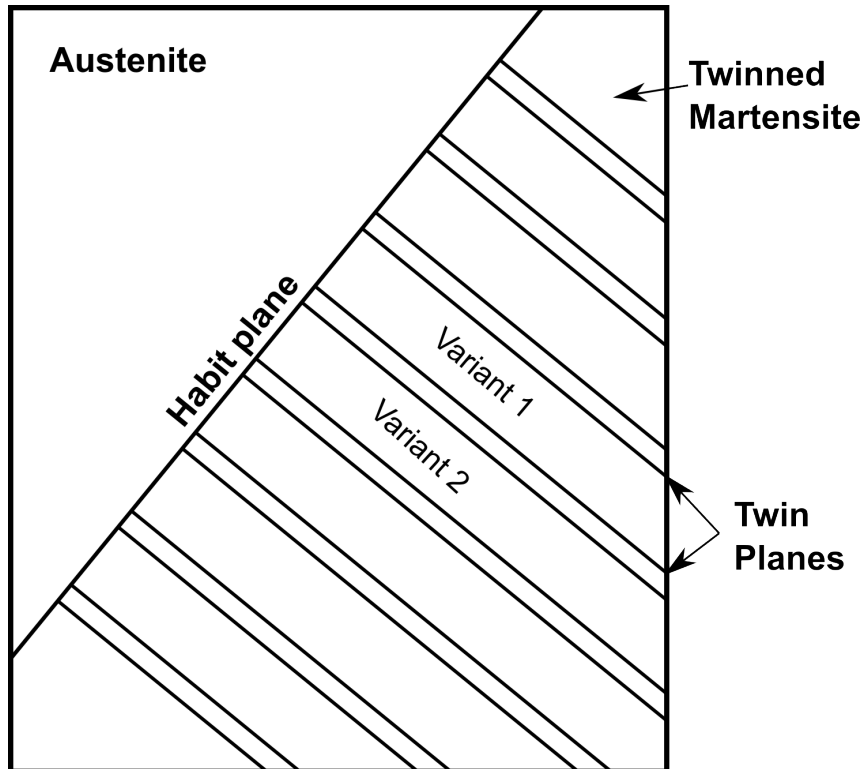


Figure 1.7: Scheme of interface between the austenite and martensite phases [3]

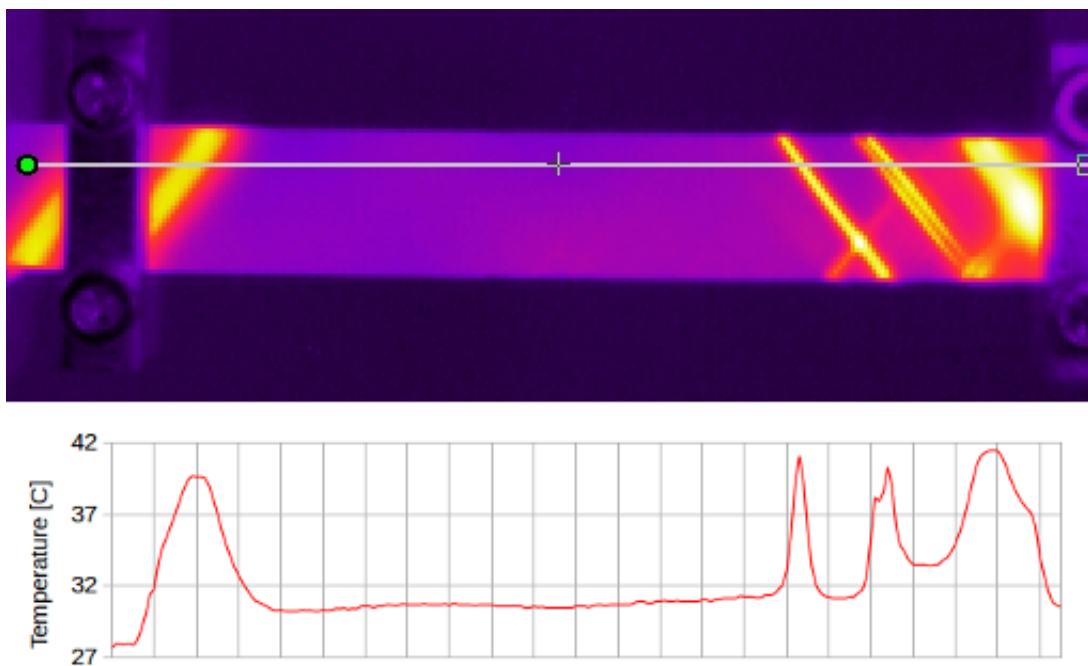


Figure 1.8: Temperature distribution on the SMA sample surface and temperature profile along the line (specimen length) at the start of the localised martensitic transformation [15]

by numerical modeling and published by Dunić et al. in [16]. Complex research on shape memory materials subjected to various loading is presented by Tobushi et al. in [17]. Pseudoelastic behavior of ferromagnetic SMA single crystal subjected to compression loading - unloading cycles presented by Pieczyska in [18].

1.3 Application of SMA

As the active material, SMA are attracting the attention of engineers and scientist in many fields. A possibility to convert thermal energy in mechanical work, reliability and multifunctionality of the SMA, candidate such alloys to be employed in realistic engineering solutions. SMA are very interesting in aerospace, aircraft and medical industries, transportation, naval and oil industry. SMA are also applied in daily used devices as i.e. in coffee makers, rice cookers, air-conditioners, headphones, flexible eyeglasses etc., but the most popular applications are still in various kind of biomedical devices.

Although the NiTi is the most expensive and more difficult to produce, it is still the most popular and the most studied SMA alloy, because of the best properties: strong pseudoelasticity and SME, higher stability in cyclic application, high strength and ductility, electrical sensitivity, resistance to corrosion and the most important for biomedical application - good biocompatibility. However, presence of Ni is questionable, especially for some medical doctors, because the fear of possible Ni release, which has been proved to cause toxic, carcinogenic, and immune-sensitizing effects [19]. But, after many investigations, it was found that NiTi alloys are very corrosion resistant and that fear is unreasonable, because Ti oxidized more rapidly than Ni, protecting the surface by TiO_2 film acting as barrier to Ni release [19]. If the exploitation conditions are extreme (like in a human body), spacial surface modification techniques are used as additional protection [19].

By addition of various alloying elements to NiTi (Cu, Co, Fe, Nb, Mo), a set of SMA with improved hysteresis, corrosion resistance, transformation temperatures, fatigue behavior is provided [20].

Various SMA behaviors can be classified in two groups: primary and secondary effects. Some of those effects can be used for application of SMA. The primary effects are [20]:

- Shape Memory Effect,
- Pseudoelasticity.

The secondary effects can be also relevant in some practical application:

- Tension-compression asymmetry,
- Generation of recovery stresses,
- High damping capacity (i.e. ability to dissipate vibration energy of structures subject to dynamic loading),
- Work production capacity.

1.3.1 Medical application

The most common commercial application of SMA are connected with biomedical application using the pseudoelasticity effect. Biocompatibility after the surface treatment of SMA based on NiTi and its good properties give unique advantage for biomedical use (orthodontic, cardiovascular, orthopedic, surgical instruments etc.) [20].

Orthodontic application

The first application of NiTi in medical purpose, since 1970s [19], is in orthodontic arch wires production (Figure 1.9). Made of NiTiNOL, they have been used as more effective solution for alignment purpose. The main advantage in comparison to steel arch wires is ability to operate in pseudoelastic plateau where stress changes can be neglected for large strain increment. That allows small force which can move the teeth during the longer period without additional readjustment. Moreover, due to almost constant temperature in the mouth cavity, it is possible to provide constant force for large strains. Various kinds of SMA can be produced to allow optimal force for different needs [3,20]. Application of SMA, allows readjustment of the wires only a few times a year instead of every 3-4 weeks for stainless steel wires [19].



Figure 1.9: Orthodontic applications of SMA: Nitinol brace used for alignment purposes in dental practice



Figure 1.10: Orthodontic applications of SMA: Scheme of NiTi drill used for root canal surgery [3].

Beside this, there are other orthodontic applications of SMA such as NiTi drills used for root canal surgery procedures Figure 1.10 and for periodontal implants Figure 1.11 [19].

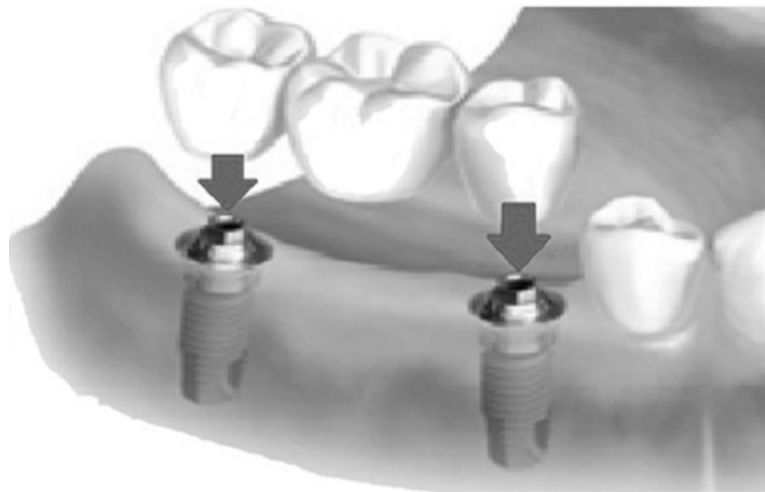


Figure 1.11: Periodontal SMA implant [19]

Orthopedic application

To obtain an effective union between disjointed bone segments, it is essential to provide stable fixation and proper compression action between the bone segments. Accordingly, fractured bones are treated with a fixation device that should strengthen the bone and keep the correct alignment during healing. Moreover, the fixation should be minimally invasive, biocompatible, and should induce a biologically appropriate compression for healing. SMAs can provide all these requirements in a very efficient way by various SMA staples, fixations, implants, correction nails etc. [19].

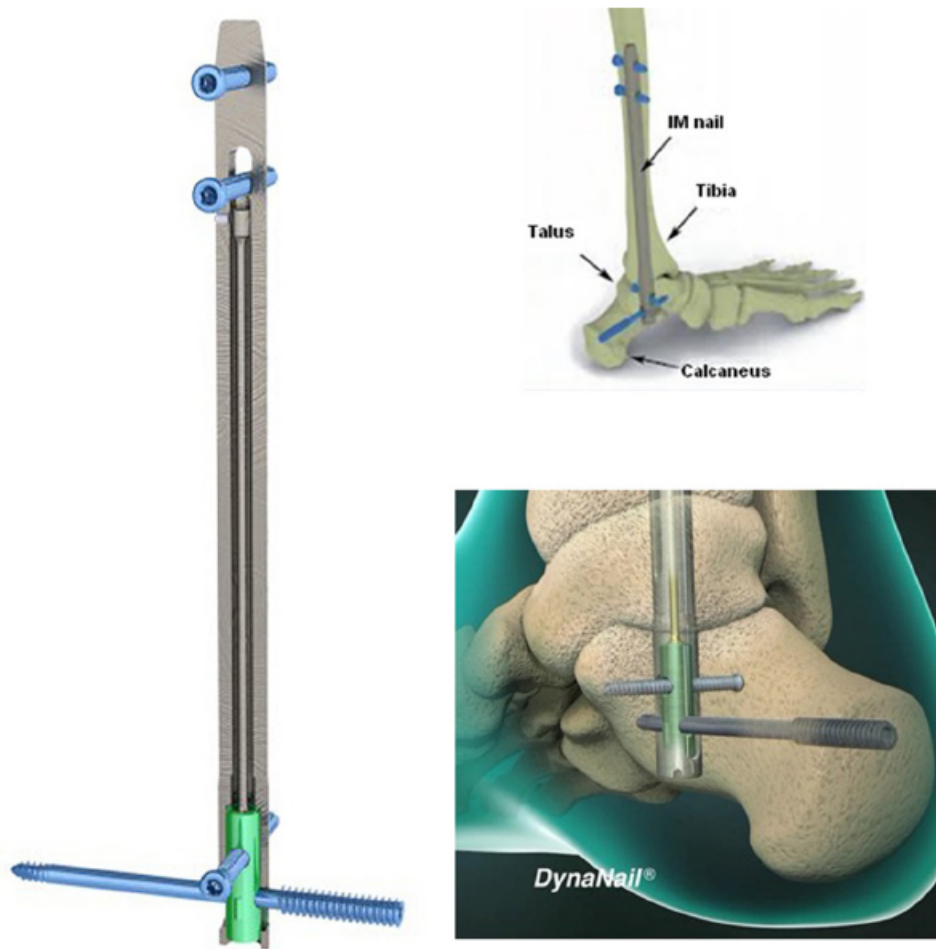


Figure 1.12: Intramedullary NiTi nail for ankle surgery [19]

Cardiovascular application

Cardiovascular application of SMA is of great importance because of minimal invasive surgery and increasing number of cardiovascular problems (atherosclerosis, hypertension, coronary heart disease, heart stroke) with high death rate [21]. The cardiovascular devices can be categorized in three possible groups: (1) catheters and guidewires; (2) embolic filters; and (3) stents. The best known cardiovascular application is the self-expanding NiTi stent (Figure 1.13). It is used to support the circumference of tubular passages in the body. When the stents are made of stainless steel, often they do not fit well or the vessel can be damaged after the implantation. On the other hand NiTi stent is self-expandable, so after the implantation the temperature exceeds A_f and the stent expands to its original larger diameter. The force is not large because it works in pseudoelastic plateau, so the walls of the vessel are gently moved [20].

The most important property of the stent is the fatigue life which is influenced

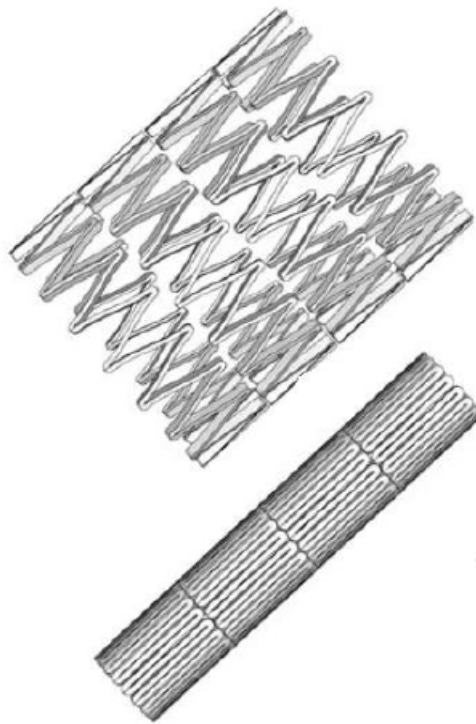


Figure 1.13: A self-expanding NiTiNOL stent shown in the relaxed configuration (above) and constrained state (below) [3]

by the pulsating blood response and by everyday life activities. In fact, stent can experience up to 40 million loading-unloading cycles each year, making the fatigue lifetime a major design criterion [19].

Other medical application

Among those presented popular applications of SMA, this materials also can be used in medical purpose in [19]:

- General surgery - devices used for surgical interventions need to be flexible and able to apply constant forces over a large deformation range (laparoscopic surgery devices, foot staple used in foot surgery Figure 1.14 [22]),
- Colorectal surgery - expansion devices, sutureless anastomosis (ColonRing) [19],
- Otolaryngology - stapes prosthesis in human ear,
- Neurosurgery - stents, coils, guidewires,
- Офтальмологији - flexible eyeglasses frame,

- Urology - urethral stents and prostatic stents Figure 1.15,
- Gynecology - implant for birthcontrol, devices for breast tumor location,
- Physiotherapy - to activate atrophied muscles using the gloves with TiNi wires.

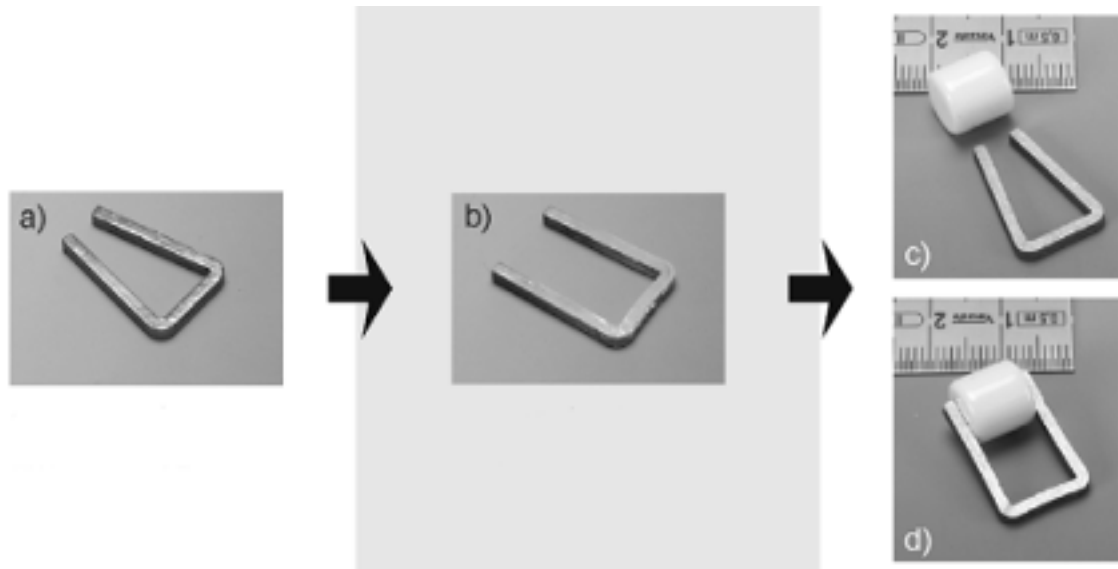


Figure 1.14: Staple used for bone fixation after the foot surgery [22]

The example of foot staple used in foot surgery is used to fix bone segments after the shortening of bones. During the shortening, the bone is cut into the segments. Afterwards, the remaining bone segments have to be fixed to help them grow together [22]. The function of the staple is shown in detail in Figure 1.14. As it can be observed, at first, the initial sample is cooled down below the martensite finish temperature M_f , then, it is opened mechanically by bending the legs of the staple into the desired position [22]. Then the staple is heated above the austenite finish temperature A_f . It will recover the original shape if no obstacles are placed between the staple's legs [22]. Inserting the bone between the legs leads to a clamping effect between the staple and the bone [22].

1.3.2 Technical application

Beside the popular medical application, SMA has become interesting for use in many other areas. The number of commercial applications is growing each year, with the largest application represented by actuators and motors [23]. The market of "smart materials" has annual growth rate of 12.8% in period 2011–2016 [23].

One of the first applications of SMA was pipe couplings [24]. The advantage of such connectors is the high durability, the easy installation, the lightweight of the



Figure 1.15: Urethral Stent (a) Picture of the stent, Made of a Nitinol Framework with a Polymeric Coating (b) Representation of an implanted urethral stent (Allium Medical Ltd., Caesarea Industrial Park South, Israel) [19]

coupling devices, and the capability to connect different materials [24]. The coupling principle is simple Figure 1.16: the connectors are manufactured in the austenite phase and the connector inner size is smaller than the devices to be coupled [24]. The connectors are cooled to a temperature below austenite start. In this temperature region, the martensitic transformation can be induced by mechanical loading. After unloading, there are residual inelastic deformations in the coupling device [24]. Now, the assembling can be done Figure 1.16 by heating of the coupling device above the austenite finish temperature what leads to a strong connection [24]. One of the well known companies which produces such devices is AeroFit Inc. in USA [25].

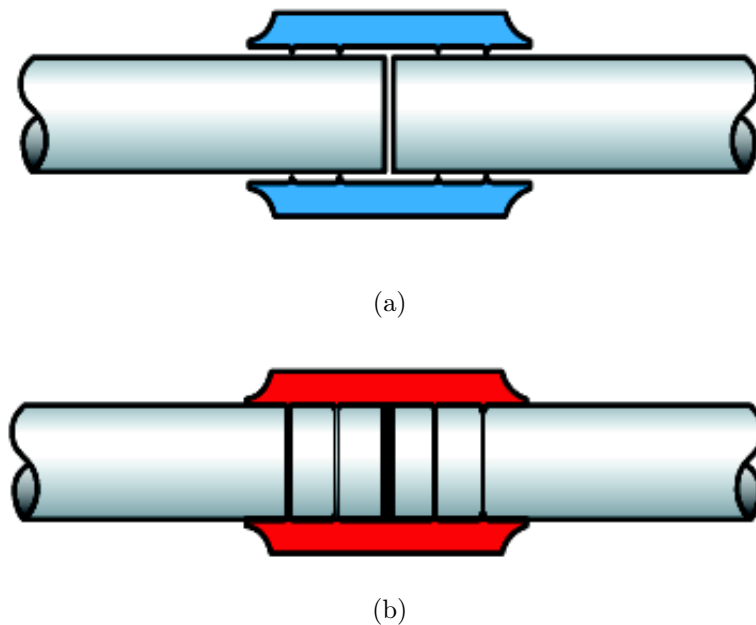


Figure 1.16: Scheme of SMA connectors for pipe couplings [25]

Also, as important field of interest, recently, SMA application has been extended

to control of civil structures [26]. This application should improve response of civil structures to external disturbances and unexpected loading toward structural safety [26]. The main desired functional properties are actuation, sensing, energy dissipation, self accommodation, structure healing etc. [23]. Such improvements are necessary in order to extend the structure lifetime and serviceability and the control during the earthquakes. As it was stated by Song et al. in [26], the control of civil structures can be active, passive and semi-active in a form of actuators, passive energy dissipaters and dampers for civil structure control.



(a) A large crack during a loading test



(b) The crack closes after the loading test

Figure 1.17: A concrete beam reinforced with superelastic stranded cables via the method of post-tensioning [26]

Active and semi-active structural control

For the active control of civil structures, the applying of forces to the controlled structure is necessary. The semi-active systems are similar to active systems, but use less energy to control the structure. The SME is useful in application of SMA as active and semi-active controllers of civil structures. Self-rehabilitation of civil structures (Figure 1.17) using low-temperature SMA is an example of active structural control. An example of semi-active control of civil structures is a tuning of natural frequency of civil structures using the SMA wires for vibration suppression [26].

Passive structural control

A passive control by response of SMA system is needed when an external force induces the motion of the structure. The passive structure control is based on the high damping capacity of SMA. A review of research on the damping properties of SMA and dependence of the damping capacity on temperature, loading frequency and the number of loading cycles is given in [26]. The SMA devices for passive structural control can be set on lower temperatures (martensitic SMA) what cause SME and on higher temperatures (austenitic SMA) with a pseudoelastic properties. The martensitic SMA have a larger damping capacity but external heat is necessary to restore its original shape. The austenitic SMA have a smaller damping capacity, but a strong force needed to restore the initial position of the structure. This classifies the SMA passive control devices in two groups: ground isolation systems and energy dissipation systems.



Figure 1.18: Four cables of 45 m long in ELSA (European Laboratory for Structural Assessment). (A) cable; (B) SMA dumper; (C) accelerometer [23, 27]

The examples of the ground SMA isolation systems described by Song et al. [26]

are: bars for highway bridges, wire re-centering devices for civil buildings, spring isolation system and tendon isolation system for a multi-degree-of-freedom shear frame structure. In the same paper, Song et al. [26] gave the examples of the energy dissipation systems: braces for frame structures, damping elements for cable-stayed bridges Figure 1.18 or simply supported bridges, connection elements for columns and structural reinforcement for earthquake retrofit.

Chapter 2

Review and analysis of existing approaches to SMA modeling

Nowadays, the money and time are missing resources, so it is obligatory to predict behavior of materials in order to optimize their functionality and reliability of construction. The complex thermomechanical response and the thermal sensitivity of the SMA make the research to be very challenging. Hence, variety of constitutive models have been introduced in order to predict the behavior accurately. This chapter presents a review of existing models and approaches.

2.1 SMA constitutive modeling approaches

Depending on the scale of investigation, three major groups of the SMA constitutive models can be distinguished [28, 29]: micromechanics-based models, micro-macro and macro (phenomenological) models.

Micromechanical or micro- models need investigation of SMA microstructure at the grain level (nucleation, interface motion, twinning etc.). Regions or grains of martensite are modeled as unique subdomains. That causes existence of a large number of internal variables what makes difficulties in engineering application, but the fundamental phenomena of material behavior are more understandable.

Phenomenological or macro- models can capture the behavior of materials at the macro-scale [30]. Such constitutive models are based on the experimental data. The constitutive laws employ the phenomenological continuum thermodynamics with internal variables to successfully describe behavior of SMA. Usually, the martensitic volume fraction is used as an internal variable. Such material models are more suitable for implementation and application because of simplicity and quick compu-

tations, but the microscopic details cannot be taken into account.

Micro-macro models are a combination of the micro- and macro- models. Based on modeling of single grain with a homogenization as the necessary solution for easier application, it is possible to predict the behavior of the material at macro-scale. The thermodynamic laws are applied to estimate martensitic transformation. The micro-structure behavior is used to describe interaction energy due to the transformation. This is an advantage but some difficulties are still present because a number of internal variables is still large.

2.2 Review of existing SMA models

Because, the idea of the research is to simulate macro (phenomenological) behavior of SMA, as the appropriate approach for the numerical implementation and the application on real problems the phenomenological approach is chosen in this research. The main focus in the review of existing SMA models will be on such kind of models, although, a few micro- and micro- macro models will be also mentioned.

The phenomenological SMA models can be classified in two groups [20]: models with and without internal variables. Models without internal variables are described by strain, stress, temperature and entropy without the variables which define phase mixture. There are two kind of such models: polynomial potential and hysteresis model [20]. Models with internal variables can describe material internal structure. The constitutive equations can be derived to depend on internal variables and a set of mechanical (stress or strain) and thermal (temperature or entropy) variables. In this thesis, continuum thermodynamics with internal variables is used as the appropriate solution for 3D SMA constitutive equations.

Models with internal variables based on the continuum thermodynamics

Many researchers from around the world are working on development of SMA constitutive models. The most popular topics are certainly: hardening during the transformation, asymmetric response in tension and compression, modeling of martensite detwinning, two-way SME, the effect of reorientation, the accumulation of plastic strains during the cyclic loading and the influence of thermo-mechanical coupling [3].

Although the 1D models are still interesting for SMA wire application, the complex geometries, like in the case of stents, and industrial applications of SMA motivated development of 3D phenomenological models. One of the first was presented by Liang and Rogers in 1992 [31]. That model was thermomechanical based on micro- and macro- mechanics and one internal variable: the martensitic volume

fraction. As the benchmark example, the torsion of a SMA rod is used. Raniecki and Lexcellent [32] in 1994 proposed a model capable to simulate complex stress states. The model was based on observation of uniaxial stress states. A combination of thermodynamic laws and a relation between the second invariant of stress and strain deviators was used for derivation of the model. A free energy function for pseudoelasticity models was presented with ideal pseudoelastic flow, with isotropic linear, and nonlinear transformation hardening. As the extension of this work, Leclercq and Lexcellent [33] in 1996 increased number of internal variables to simulate SMA behavior. They used two internal parameters: "the volume fraction of self-accommodating (pure thermal effect) and oriented (stress induced) product phase". During the same year, Boyd and Lagoudas [34] presented the thermodynamical constitutive model for monolithic SMA. They used a free energy function and a dissipation potential to model PE and SME. They considered three cases based on the number of internal state variables.

During the 1998, Raniecki and Lexcellent [35] continued their research proposing the thermodynamic theory for pseudo-elastic behavior of SMA which takes into account tension-compression asymmetry. During the same year, Souza et al. [36] proposed 3D phenomenological model to describe the mechanical behavior of polycrystalline solids under stress loading. A transformation strain tensor is introduced to take into consideration Stress Induced Martensitic Transformation (SIMT).

Qidwai and Lagoudas (2000) [37, 38] derived "constitutive relations in stress-temperature space using Lagrangian formulation". They investigated various transformation functions with idea to propose the most proper one. A numerical implementation of SMA thermomechanical constitutive model was given using closest point projection and the convex cutting plane return mapping algorithm which was already used in plasticity. In 2001, Auricchio [39] presented efficient and robust algorithm for 3D SMA model for large strains intended for analysis of SMA-based devices. During the same year, Thamburaja and Anand [40] investigated super-elastic behavior of SMA in tension-torsion. That is a polycrystalline model, where each element is a crystal with the orientation, texture etc. "The macroscopic stress-strain responses are calculated as volume averages over the entire aggregate."

Also, Lexcellent et al. [41] done research under biaxial proportional loading experimentally on a CuZnAl and CuAlBe alloys to define initial phase transformation surface. Auricchio and Petrini in 2002 [42] and 2004 [43, 44] continued research to capture asymmetric behavior of SMA and thermo-mechanical coupling effect. In paper published in 2002 they considered 3D model proposed by Souza et al. [36] and suggested improvements needed for development and implementation of algorithm

into FEM framework. In 2004 they presented model which can take into account thermo-mechanical coupling in order to simulate such problems. Between those two papers (2003), Helm and Haupt [45] developed the phenomenological model able to capture multiaxial loading behavior of SMA with the one- and two-way SME, pseudo-elastic and pseudo-plastic behavior. The model is based on a free energy function and evolution equations for internal variables. In 2007, Popov and Lagoudas in [46] introduced polycrystalline 3D SMA model based on modified phase diagram. The model uses three internal variables to predict the martensitic transformation and detwinning what makes it suitable for numerical analysis of complex thermomechanical loading problems. Panico and Brinson in 2007 [9] proposed a macroscopic phenomenological model able to capture effects of multiaxial and non-proportional loading alongside an evolution of twinned and detwinned martensite. The inelastic strain is split into two parts: derived from creation of detwinned martensite and reorientation of previously existing martensite variants.

Zaki and Moumni (2007) [47] used two internal variables: the martensite volume fraction and martensite orientation strain tensor to take into account self-accommodation, orientation and reorientation of martensite with one-way SME and pseudoelasticity. Also, they presented a procedure for material parameters identification in order to compare the numerical and experimental results.

Reese and Christ during the 2008 [48] presented a new phenomenological constitutive model extended to large strain problems. The reason for this is increasing requirement to simulate NiTi stents. A year later in [22], they proposed a new thermomechanically coupled material model for SMA. The relations are presented for the large strain case. A multiplicative decompositions of the deformation gradient is used. The thermomechanical coupling is realized in a monolithic approach.

Thamburaja in 2010 [49] presented the thermo-mechanically coupled polycrystalline SMA constitutive model for large strain problems. The model is capable to simulate behavior of SMA under multiaxial loading conditions. Arghavani et al. [50] introduced a phenomenological constitutive model for SMA based on irreversible thermodynamics and internal variables: the amount of martensite and the direction of variants. Using this variables, multiaxial non-proportional loadings can be captured more accurately. Later in [51], Arghavani et al. extended the Panico and Brinson [9] small strain model to solve finite strain problems by using a multiplicative decomposition of deformation gradient and an additive decomposition of inelastic strain rate tensor into transformation and reorientation parts. During the same year, Hartl et al. [52] considered "the generation and evolution of irrecoverable viscoplastic strains in an SMA material". There are situations when such strains

appear when they are subjected to high temperatures. They proposed a constitutive model which can take into account that behavior.

In 2012 Lagoudas et al. [28] published work about the thermomechanical SMA constitutive model. The improvements with respect to the Boyd and Lagoudas [34] work are the smooth transition and dependence of thermodynamic force on applied stress magnitude. Recently there were a few ideas of small strain constitutive models reformulation to be able to solve large strain problems [53, 54]. Stupkiewicz and Petryk [54] recently presented a model of pseudoelasticity in SMA and a methodology for extension of the model from the small-strain to finite-deformation regime. They have employed the multiplicative decomposition of the deformation gradient and exponential mapping of the logarithmic transformation strain. Also, Teeriahoo [53] suggested the similar idea for the theory presented by Lagoudas [3]. He used the Eulerian rate type formulation with an additive decomposition of the stretching tensor.

Loading rate influence on SMA behavior

A special review will be presented for the influence of loading rate on the SMA behavior. As it was observed by Pieczyska et al. [8, 13, 14], the behavior of SMA is different for various loading rates. The stress-strain response hardens more and the hysteresis loop becomes wider for the higher strain rates. In order to simulate such behavior, Mirzaeifar et al. [55] used an explicit finite difference scheme to investigate the response of SMA in tension, taking into account the effect of generated latent heat accompanying the transformation. They considered several case studies with different specimen geometry, loading and unloading rates, as well as boundary conditions. Morin et al. [56] examined the strain rate dependence of the SMA mechanical pseudoelastic response by using the FEM and studied influences of the strain rate and the environment conditions. Grandi et al. [57] performed a number of numerical tests, which investigated the SMA mechanical behaviour in various conditions. Yang and Dui also examined in [58] TiNi alloys under tensile loading. They focused on the strain localization and propagation phenomena. Among others, the rate-dependent stress-strain hysteresis was discussed by taking into account the specimen temperature changes. Three kinds of boundaries at the testing specimen ends were discussed.

TiNi SMA was experimentally analyzed under tension for various stress and strain rates by Pieczyska et al. [8]. The nucleation and development of stress-induced martensitic transformation were investigated based on the temperature distribution on the specimen surface, measured by a fast and sensitive infrared camera. Details

about stress-strain dependences were analyzed with respect to the loading manner. Creation of numerous fine transformation bands was observed at different stages of the martensitic forward and reverse transformation. The obtained effects, related to the transformation, were discussed depending on the loading conditions.

Dunić et al. [16] investigated comparison of experimental data to the numerical simulation results. The comparison have been done for SMA tension tests under different loading rates. It was shown that the results are reproduced quantitatively and qualitatively by the numerical FEM model, which verifies the accuracy of the proposed investigation method.

2.3 Research topics and outline of the dissertation

The previous works and the increasing need for simulation of complex thermo-mechanical response in realistic problems inspired the author to focus on several topics important for accurate and efficient numerical analysis of the SMA behavior.

The purpose of the thesis is to successfully reformulate and numerically implement a simple phenomenological constitutive model for the SMA presented by Lagoudas and to capture experimentally measured results and observed effects. In this scope, the model developed and implemented by Lagoudas et al. [3, 52] has been reformulated by derivation of all variables to depend on effective values of stress and strain, and internal parameter which describe fraction of martensite in volume. Gibbs free energy is used as the thermodynamic potential.

To successfully simulate thermo-mechanical behavior of SMA, a partitioned coupling approach is applied to couple programs for structural [59] and heat transfer analysis [60]. A dissipative energy of martensitic phase transformation is employed as variable which influences change of material temperature as an internal thermal source.

The partitioned approach is realized using the block Gauss-Seidel algorithm [61, 62]. As a communication interface between the programs for structural and heat transfer analysis, Component Template Library (CTL) [63] is used as middleware. The software coupled in this way, allows thermo-mechanical analysis of SMA and investigation of loading rate influence on the material behavior. Because the SMA are very thermo-sensitive materials, this improvement is necessary for the accurate simulation. The comparison of numerical and experimental results [8] of the SIMT occurring in the same TiNi SMA has been studied. The experimental tests of the SMA are performed under different loading rates and the initiation, development and saturation of the phase transformation is observed.

The experiments have been carried out at the Institute of Fundamental Technological Research (pol. Instytut Podstawowych Problemow Techniki - IPPT) (IFTR), Polish Academy of Sciences (pol. Polskiej Akademii Nauk - PAN) (PAS) and at the Aichi Institute of Technology (AIT), Japan [8, 13, 14, 17]. The SIMT development and saturation in various loading conditions are also numerically simulated. The obtained thermomechanical results are compared to the experimental data with focus on the rate-dependent response to present the ability and accuracy of such an approach to quantitatively and qualitatively reproduce the experimental results.

Extension to the large strain problems has been realized by suggestions given in [53, 64, 65]. The solution is based on multiplicative decomposition of the deformation gradient. The logarithmic strain is employed for the simulation of several selected examples to verify functionality and accuracy of such implementation.

Chapter 3

Improved constitutive model for the analysis of SMA

Those who fall in love with practice without science are like a sailor who enters a ship without a helm or a compass, and who never can be certain whither he is going.

Leonardo da Vinci

The strain nature determines a theory which needs to be used to accurately describe behavior of the materials. Small strain theory is applicable for the small strains and the small rotations, so the undeformed and deformed configurations of the body are assumed to be identical. Finite or large strain theory is needed for the large strains and the large rotations, where the undeformed and deformed configurations are different.

This chapter gives an overview of some basic principles of continuum mechanics (kinematics, conservation laws and constitutive equations) and thermodynamics. The kinematics is needed to describe geometry of motion and deformation without consideration of causes. The conservation laws describe how external forces influence the motion. The constitutive equations define behavior of the material by mathematical equations.

Continuum mechanics is a tool capable to explain physical phenomena without knowledge of material micro-structure. So, for the good understanding of the macroscopic behavior of materials, the motion and deformation need to be explained. The details necessary for correct definition of strain measure for the large strain theory is given, as well as energetically conjugated stress measures. Presented continuum mechanics and thermodynamics are used to describe SMA behavior based on the

Lagoudas model [3] with the applied modification for more efficient implementation and application. The logarithmic strain is used and the updated-Lagrangian-Hencky (ULH) formulation [59, 64, 66].

3.1 Kinematics

3.1.1 Deformation gradient

A studying of the deformation of the continuum body between the reference and current configuration, defined the necessity to introduce a deformation gradient as two point tensor. The deformation gradient is given as [66–69]:

$$\mathbf{F} = \frac{\partial \mathbf{x}}{\partial \mathbf{X}}, \quad (3.1)$$

where \mathbf{X} is the position vector in reference configuration and \mathbf{x} the position vector in current configuration. Also, the ratio of the current volume (v) and the reference volume (V) is described by the determinant of deformation gradient \mathbf{F} [67]:

$$J = \det \mathbf{F} = \frac{dv}{dV} > 0. \quad (3.2)$$

3.1.2 Polar decomposition of deformation gradient

The deformation gradient can also be decomposed by the polar decomposition into a left \mathbf{v} and a right \mathbf{U} stretch tensor and a rotation tensor \mathbf{R} as:

$$\mathbf{F} = \mathbf{R}\mathbf{U} = \mathbf{v}\mathbf{R}, \quad (3.3)$$

with the following properties:

$$\mathbf{R}^{-1} = \mathbf{R}^T, \quad \mathbf{U} = \mathbf{U}^T, \quad \mathbf{v} = \mathbf{v}^T. \quad (3.4)$$

The rotation tensor measures the local rotation. The relation $\mathbf{F} = \mathbf{R}\mathbf{U}$ is known as the right polar decomposition, while $\mathbf{F} = \mathbf{v}\mathbf{R}$ is the left polar decomposition [67]. Using the spectral decomposition [70], the right stretch tensor \mathbf{U} can be presented as:

$${}^t_0\mathbf{U} = \sum_k {}^t_0\lambda_k {}^t\mathbf{p}_k \otimes {}^t\mathbf{p}_k, \quad (3.5)$$

where λ_k are the principal stretches and \mathbf{p}_k are corresponding principal directions obtained by the eigenanalysis of \mathbf{C} [64]. In the similar manner, it is possible to

define the left stretch tensor [70]:

$${}^t_0\mathbf{v} = \sum_k {}^t_0\lambda_k {}^t\mathbf{q}_k \otimes {}^t\mathbf{q}_k, \quad (3.6)$$

with the same principal stretches λ_k . The vectors \mathbf{p}_k and \mathbf{q}_k are the unit length and denote the eigenvectors of \mathbf{C} and \mathbf{b} . These vectors form two orthonormal bases (right and left) with the relation:

$$\mathbf{q}_k = \mathbf{R}\mathbf{p}_k. \quad (3.7)$$

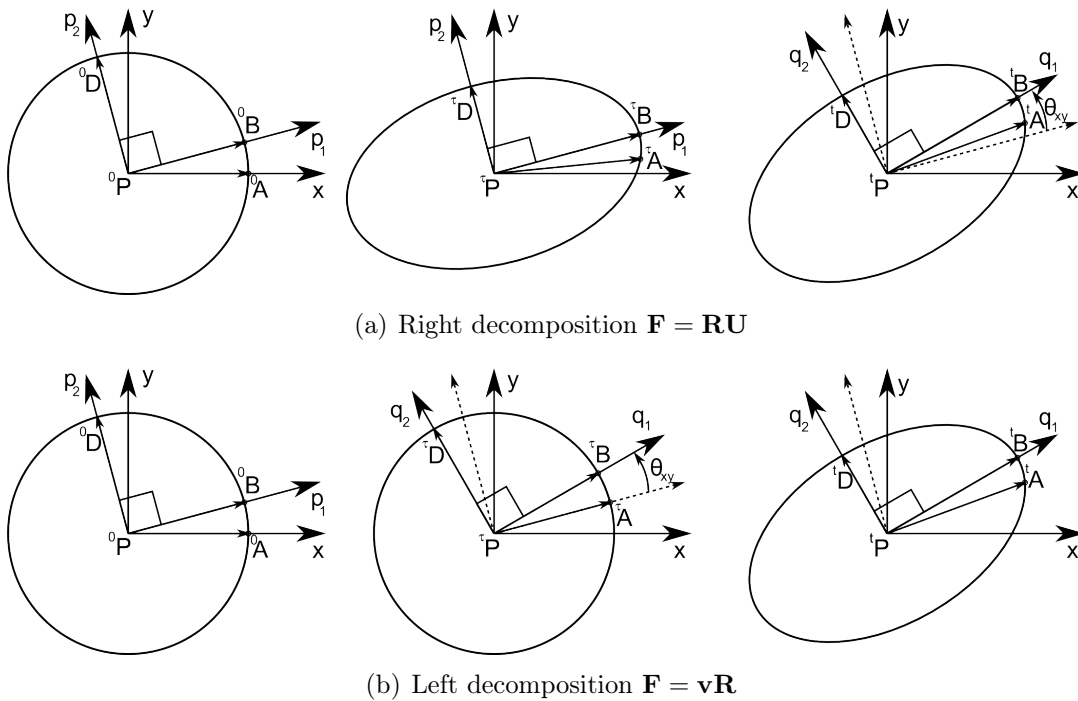


Figure 3.1: Scheme of deformation presented by polar decomposition [64]

In Figure 3.1 is given the deformation sequence in the x,y plane, where the third principal vector is normal to the plane. In Figure 3.1(a), by applying the stretch \mathbf{U} , the circular material surrounding point P deforms into the ellipse with the principal directions \mathbf{p}_k . As it can be noticed, all vectors (i.e. $\vec{P}\vec{A}$) containing the point P change lengths and directions except the vectors $\vec{P}\vec{B}$ and $\vec{P}\vec{D}$ which change length only. The final position of the material is obtained by the rigid rotation for the angle θ_{xy} . The proposed sequence could be changed (Figure 3.1(b)), so that the first rotate is made by rotation tensor \mathbf{R} for the angle θ_{xy} and then stretch by the left stretch tensor \mathbf{v} [64].

3.1.3 Deformation and strain tensors

Beside the deformation gradient, it is also possible to define other strain measures. The right Cauchy-Green (or Green) tensor \mathbf{C} and the left Cauchy-Green (or Finger) tensor \mathbf{b} can be defined as [66, 67, 69]:

$$\mathbf{C} = \mathbf{F}^T \mathbf{F} = \mathbf{U}^2, \quad (3.8)$$

$$\mathbf{b} = \mathbf{F} \mathbf{F}^T = \mathbf{v}^2. \quad (3.9)$$

Both tensors are symmetric and positive definite what means that:

$$\mathbf{C} = \mathbf{F}^T \mathbf{F} = (\mathbf{F}^T \mathbf{F})^T = \mathbf{C}^T, \quad (3.10)$$

$$\mathbf{b} = \mathbf{F} \mathbf{F}^T = (\mathbf{F} \mathbf{F}^T)^T = \mathbf{b}^T. \quad (3.11)$$

According to (3.4), the stretch tensors can be related to the associated deformation tensors as [66, 67]:

$$\mathbf{U} = \mathbf{C}^{\frac{1}{2}}, \quad (3.12)$$

$$\mathbf{v} = \mathbf{b}^{\frac{1}{2}}. \quad (3.13)$$

The strain tensors also represent the finite strain measures. The strain tensors can be represented as the function of the right Cauchy-Green deformation tensor as [66, 67]:

$$\mathbf{E} = \frac{1}{2} (\mathbf{C} - \mathbf{I}) = \frac{1}{2} (\mathbf{F}^T \mathbf{F} - \mathbf{I}), \quad (3.14)$$

which is known as the Green-Lagrange strain tensor. The strain tensor also can be represented as a function of the left Cauchy-Green deformation tensor as [66, 67]:

$$\mathbf{e}_{EA} = \frac{1}{2} (\mathbf{I} - \mathbf{b}^{-1}) = \frac{1}{2} (\mathbf{I} - \mathbf{F}^{-T} \mathbf{F}^{-1}). \quad (3.15)$$

This tensor is well known as Euler-Almansi strain tensor.

3.1.4 Generalized strain measure

According to Hill [71], there is a function family $g(\lambda_k)$ of the principal stretches λ_k which can define a strain measure. The generalized strain in the principal directions \mathbf{p}_k is defined as [64]:

$$\mathbf{E} = \sum g(\lambda_k) \mathbf{p}_k \otimes \mathbf{p}_k. \quad (3.16)$$

This strain corresponds to the configuration reached by applying the stretch \mathbf{U} . In the current configuration, the principal stretches λ_k have directions of the left basis \mathbf{q}_k , so it is possible to define the generalized strain measure as [64, 70]:

$$\hat{\mathbf{E}} = \sum g(\lambda_k) \mathbf{q}_k \otimes \mathbf{q}_k, \quad (3.17)$$

where the function g need to satisfy the conditions [64]:

$$g(1) = 0, \quad (3.18)$$

$$\left(\frac{\partial g}{\partial \lambda} \right)_{\lambda=1} = g'(1) = 1. \quad (3.19)$$

A general formula for the family of functions is given as [64]:

$$g(\lambda_k)^n = \frac{1}{2n} (\lambda_k^{2n} - 1). \quad (3.20)$$

For the special case $n = 0$ [64]:

$$g(\lambda_k)^0 = \ln \lambda_k, \quad (3.21)$$

the Hencky strain is obtained in the direction of the right or the left basis. The Hencky strain of the right \mathbf{H} and left \mathbf{h} Cauchy-Green strain tensors are respectively [70]:

$$\mathbf{H} = \frac{1}{2} \ln \mathbf{C} = \ln \mathbf{U} = \sum_{k=1}^3 (\ln \lambda_k) \mathbf{p}_k \otimes \mathbf{p}_k, \quad (3.22)$$

$$\mathbf{h} = \frac{1}{2} \ln \mathbf{b} = \ln \mathbf{v} = \sum_{k=1}^3 (\ln \lambda_k) \mathbf{q}_k \otimes \mathbf{q}_k, \quad (3.23)$$

where $\lambda_k = c_k^{\frac{1}{2}} = b_k^{\frac{1}{2}}$ are the principal stretches or the principal values of strain tensors. The principal directions of the left and right stretch tensor differ only for rotation.

3.1.5 Rates of deformation tensors

Within this subsection, it will be shown how some of the strain tensors change with time by knowing the motion [67]:

$$\mathbf{x} = \boldsymbol{\chi}(\mathbf{X}, t), \quad (3.24)$$

where $\boldsymbol{\chi}$ is the motion of the body. The velocity gradient or time rate of change of the deformation gradient is [67]:

$$\dot{\mathbf{F}} = \frac{\partial}{\partial t} \left(\frac{\partial \boldsymbol{\chi}(\mathbf{X}, t)}{\partial \mathbf{X}} \right) = \frac{\partial}{\partial \mathbf{X}} \left(\frac{\partial \boldsymbol{\chi}(\mathbf{X}, t)}{\partial t} \right) = \frac{\partial \mathbf{V}(\mathbf{X}, t)}{\partial \mathbf{X}}, \quad (3.25)$$

where $\mathbf{V}(\mathbf{X}, t)$ is material description of the velocity field. Spatial velocity gradient \mathbf{l} is defined as [67]:

$$\mathbf{l}(\mathbf{x}, t) = \frac{\partial \mathbf{v}(\mathbf{x}, t)}{\partial \mathbf{x}}, \quad (3.26)$$

where $\mathbf{v}(\mathbf{x}, t)$ is spatial description of the velocity field. Now, it is possible to express the spatial velocity gradient through the material velocity gradient as [67]:

$$\mathbf{l} = \dot{\mathbf{F}}\mathbf{F}^{-1}. \quad (3.27)$$

The spatial velocity gradient can be additively decomposed into the symmetric and anti-symmetric (skew) part as [67]:

$$\mathbf{l} = \mathbf{d} + \mathbf{w}, \quad (3.28)$$

where \mathbf{d} and \mathbf{w} are the rate of the deformation tensor and spin (or vorticity) tensor respectively [67]:

$$\mathbf{d} = \frac{1}{2} (\mathbf{l} + \mathbf{l}^T), \quad \mathbf{d} = \mathbf{d}^T, \quad (3.29)$$

$$\mathbf{w} = \frac{1}{2} (\mathbf{l} - \mathbf{l}^T), \quad \mathbf{w} = -\mathbf{w}^T. \quad (3.30)$$

Now, it is possible to express time derivatives of some strain tensors. Material derivative of the Green-Lagrange strain tensor is [67]:

$$\dot{\mathbf{E}} = \frac{1}{2} \left(\dot{\mathbf{F}}^T \mathbf{F} + \mathbf{F}^T \dot{\mathbf{F}} \right) = \mathbf{F}^T \frac{1}{2} (\mathbf{l}^T + \mathbf{l}) \mathbf{F} = \mathbf{F}^T \mathbf{d} \mathbf{F}. \quad (3.31)$$

This derivative is also known as material strain rate tensor. Also, base on (3.8) and (3.14) the time rate of change of the right Cauchy-Green strain tensor is [67]:

$$\dot{\mathbf{C}} = 2\dot{\mathbf{E}} = 2\mathbf{F}^T \mathbf{d} \mathbf{F}. \quad (3.32)$$

Similarly, the derivative of the left Cauchy-Green strain tensor can be represented as [67]:

$$\dot{\mathbf{b}} = \mathbf{l} \mathbf{b} + \mathbf{b} \mathbf{l}^T. \quad (3.33)$$

3.1.6 Objective corotational rates

In the continuum mechanics, the constitutive relations are required to satisfy the principle of the material objectivity (the principle of material frame-indifference) [72]. Corotational rate of the Eulerian, objective, symmetric second-order tensor \mathbf{a} is defined as [53, 72, 73]:

$$\dot{\mathbf{a}} = \dot{\mathbf{a}} + \mathbf{a}\boldsymbol{\Omega} - \boldsymbol{\Omega}\mathbf{a}, \quad (3.34)$$

where $\dot{\mathbf{a}}$ is the material time derivative, $\boldsymbol{\Omega}$ is an anti-symmetric spin tensor. The form of the spin tensor specifies kind of corotational rate [72]. Two well known corotational rates are [72]:

Jaumann

$$\boldsymbol{\Omega} = \mathbf{w}, \quad (3.35)$$

and Green-Naghdi:

$$\boldsymbol{\Omega} = \dot{\mathbf{R}}^T \mathbf{R}, \quad (3.36)$$

where \mathbf{R} is rotation tensor obtained by polar decomposition. Xiao et al. and Xiao [73, 74] have shown that the corotational rate can be represented as a function of the spin tensor as:

$$\boldsymbol{\Omega} = \mathbf{w} + \sum_{i \neq j}^n h \left(\frac{b_i}{b_j} \right) \mathbf{q}_i \mathbf{d} \mathbf{q}_j, \quad (3.37)$$

where h is function of spin which defines objective corotational rate, while b_k and \mathbf{q}_k are eigenvalues and corresponding eigenprojections of the left Cauchy-Green strain tensor \mathbf{b} . The spin function for the logarithmic rate is [53, 75]:

$$h(z) = \frac{1+z}{1-z} + \frac{2}{\ln z}, \quad (3.38)$$

where z is positive real variable, so h has a property [75]:

$$h(z^{-1}) = -h(z). \quad (3.39)$$

In that case, logarithmic spin is [53, 73]:

$$\boldsymbol{\Omega}^{log} = \mathbf{w} + \sum_{i \neq j}^n \left(\frac{b_j + b_i}{b_j - b_i} + \frac{2}{\ln b_i - \ln b_j} \right) \mathbf{q}_i \mathbf{d} \mathbf{q}_j, \quad (3.40)$$

while the logarithmic rate of the Eulerian logarithmic strain is [53, 73]:

$$\mathbf{h}^{log} = \dot{\mathbf{h}} + \mathbf{h}\boldsymbol{\Omega}^{log} - \boldsymbol{\Omega}^{log}\mathbf{h} = \mathbf{d}. \quad (3.41)$$

Here, it can be noticed that observer in a rotating frame defined by the logarithmic spin $\mathbf{\Omega}^{log}$ will observe that the rate of change of the logarithmic strain $\ln \mathbf{v}$ is exactly identical with the stretching \mathbf{d} [74]. Furthermore, the logarithmic spin is the only with such properties.

According to [53], if there is Euler second order tensor \mathbf{P} , corotational rate $\mathring{\mathbf{A}}$ associated with the same rotation tensor \mathbf{R} as the integration, then:

$$\int_{corot} \mathring{\mathbf{A}} ds = \mathbf{A}. \quad (3.42)$$

By integrating (3.41) using the logarithmic corotational integration the Hencky strain is [53]:

$$\mathbf{h} = \int_{corot} \mathbf{h}^{log} ds, \quad (3.43)$$

i.e. the logarithmic corotational integration of \mathbf{d} is the Eulerian Hencky strain [53].

3.1.7 Elastic and inelastic deformation

Transformation strain is inelastic and it can be investigated similarly as plastic strain. So, for the small strain case, total strain can be decomposed to elastic and inelastic part by additive decomposition [73]:

$$\mathbf{e} = \mathbf{e}^E + \mathbf{e}^{IN}, \quad (3.44)$$

where:

$$\dot{\mathbf{e}} = \dot{\mathbf{e}}^E + \dot{\mathbf{e}}^{IN}. \quad (3.45)$$

Here, $\dot{\mathbf{e}}^E$ and $\dot{\mathbf{e}}^{IN}$ are the elastic and inelastic strain rate.

Small strain theory cannot be used for the correct numerical analysis simulation when the large strains or rotations appear. The large strain problem is arguing topic, what is represented by the number of bibliographical data (441) given by Xiao in [73]. Extension to the large (finite) strain theory can be introduced in a few different approaches.

The first approach is direct extension of the small strain theory by additive decomposition of the strain rate tensor [73]:

$$\mathbf{d} = \mathbf{d}^E + \mathbf{d}^{IN}, \quad (3.46)$$

where \mathbf{d}^E and \mathbf{d}^{IN} are elastic and inelastic stretching in current configuration. In

this case, hypo-elastic behavior of the material can be represented by the Hook law as:

$$\mathbf{e}^E = \frac{\boldsymbol{\sigma}}{2\mu} - \frac{\nu}{1+\nu} \frac{\text{tr}\boldsymbol{\sigma}}{2\mu} \mathbf{I}, \quad (3.47)$$

or in the rate formulation:

$$\dot{\mathbf{e}}^E = \frac{\dot{\boldsymbol{\sigma}}}{2\mu} - \frac{\nu}{1+\nu} \frac{\text{tr}\dot{\boldsymbol{\sigma}}}{2\mu} \mathbf{I}. \quad (3.48)$$

Direct extension of the previous equation can be proposed by change of the elastic strain rate $\dot{\mathbf{e}}^E$ with \mathbf{d}^E . Obtained equation is not objective, so the objective stress tensor need to be defined. If the objective rate of the Kirchhoff stress $\dot{\boldsymbol{\tau}}$ is introduced, the direct extension of the equation (3.48) to large strain theory can be given as [73]:

$$\mathbf{d}^E = \frac{\dot{\boldsymbol{\tau}}}{2\mu} - \frac{\nu}{1+\nu} \frac{\text{tr}\dot{\boldsymbol{\tau}}}{2\mu} \mathbf{I}, \quad (3.49)$$

or:

$$\dot{\boldsymbol{\tau}} = \mathbb{H}\mathbf{d}^E, \quad (3.50)$$

where \mathbb{H} is the fourth-order elasticity tensor which generally depends on $\boldsymbol{\tau}$. Such approach may not be integrable without additional care that all incremental relations between the stress and strain have to be objective. This situation may result in unwanted behavior such as hysteretic dissipation inappropriate for an elastic model [76].

The second approach is hyperelastic behavior of elastic response using the multiplicative decomposition of deformation gradient to decompose deformation gradient into elastic and inelastic part. Based on the Lee paper [77], it is possible to introduce multiplicative decomposition of the total deformation gradient as [64, 67, 68]:

$$\mathbf{F} = \mathbf{F}^E \mathbf{F}^{IN}, \quad (3.51)$$

where \mathbf{F}^E and \mathbf{F}^{IN} are elastic and inelastic deformation gradient. The main idea is introduction of the conceptual intermediate configuration which has local character and can be obtained by relaxation from deformed to stress-free state. According to Figure 3.2, it can be noticed that [73]:

$$d\bar{\mathbf{x}} = \mathbf{F}^{IN} d\mathbf{X}, \quad (3.52)$$

$$d\mathbf{x} = \mathbf{F}^E d\bar{\mathbf{x}}, \quad (3.53)$$

$$d\mathbf{x} = \mathbf{F} d\mathbf{X}. \quad (3.54)$$

So, does not undergo inelastic deformation to intermediate configuration and than elastically transformed to current configuration.

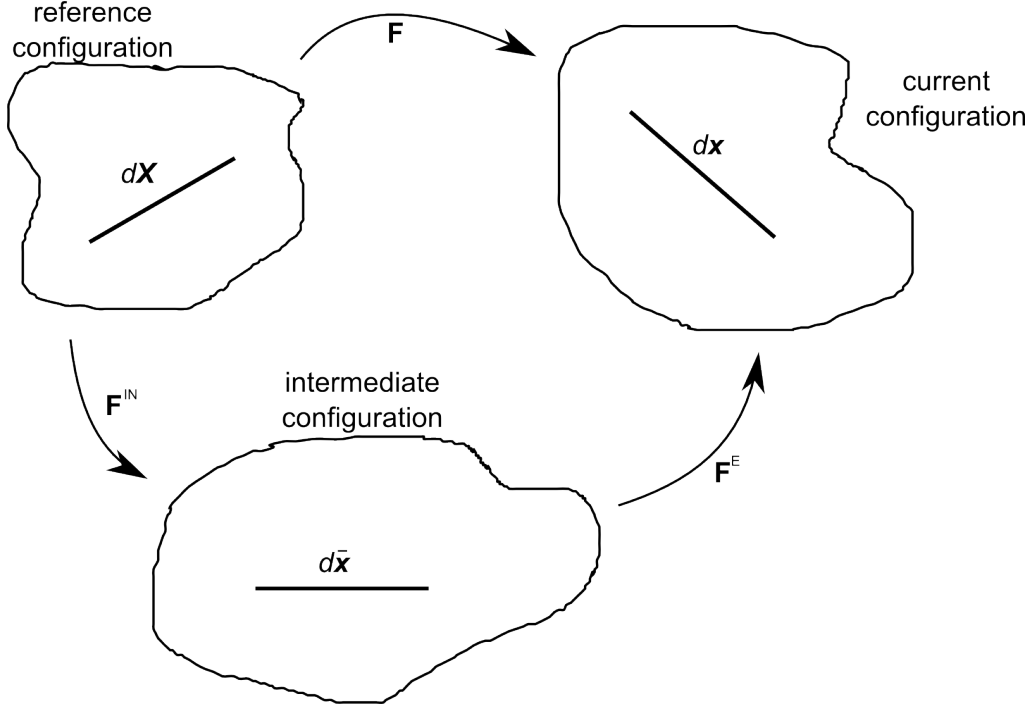


Figure 3.2: Scheme of multiplicative decomposition of the deformation gradient

General hyperelastic behavior is considered formulated relative to the material (Lagrangian), spatial (Eulerian) or intermediate configuration. Introduction of intermediate configuration needs clear understanding of strain tensors in corresponding configurations. In each configuration, a metric tensor can be defined, so material metric tensor is denoted with \mathbf{G} , spatial with \mathbf{g} and the metric tensor in intermediate configuration is $\bar{\mathbf{G}}$ [76]. Applying the push forward and pull back operations on metric tensors between the mentioned configurations, we obtain corresponding strain tensors in chosen configurations [70].

In the material description, the local inelastic state of the material is characterized by the Lagrangian strain tensor \mathbf{E} and inelastic Lagrangian strain [76]:

$$\mathbf{E}^{IN} = \frac{1}{2} (\mathbf{C}^{IN} - \mathbf{G}), \quad (3.55)$$

where, the right Cauchy-Green inelastic strain tensor is obtained by pull back transformation of metric tensor in the intermediate configuration by inelastic deformation gradient \mathbf{F}^{IN} :

$$\mathbf{C}^{IN} = (\mathbf{F}^{IN})^T \bar{\mathbf{G}} \mathbf{F}^{IN}. \quad (3.56)$$

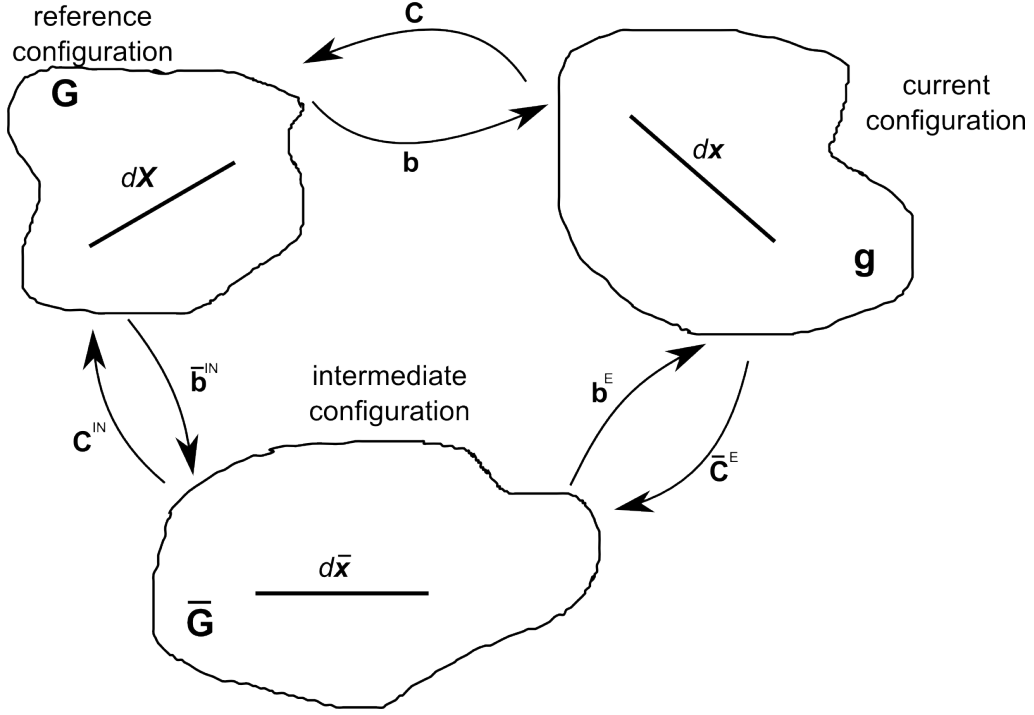


Figure 3.3: Scheme of Cauchy-Green strain tensors in corresponding configurations

In this context, elastic Lagrangian strain \mathbf{E}^E is formally defined as [76]:

$$\mathbf{E}^E = \mathbf{E} - \mathbf{E}^{IN}. \quad (3.57)$$

Relative to intermediate configuration, the local inelastic state is characterized by the Lagrangian strain tensor [76]:

$$\bar{\mathbf{E}}^E = \frac{1}{2} (\bar{\mathbf{C}}^E - \bar{\mathbf{G}}), \quad (3.58)$$

$$\bar{\mathbf{E}}^{IN} = \frac{1}{2} \left(\bar{\mathbf{G}} - (\bar{\mathbf{b}}^{IN})^{-1} \right), \quad (3.59)$$

where, the right Cauchy-Green elastic strain tensor is obtained by pull back transformation of metric tensor in current configuration by elastic deformation gradient \mathbf{F}^E :

$$\bar{\mathbf{C}}^E = (\mathbf{F}^E)^T \mathbf{g} \mathbf{F}^E, \quad (3.60)$$

while the left inelastic Finger strain tensor is obtained by push forward transformation of metric tensor in reference configuration by inelastic deformation gradient:

$$(\bar{\mathbf{b}}^{IN})^{-1} = (\mathbf{F}^{IN})^{-T} \mathbf{G}^{-1} (\mathbf{F}^{IN})^{-1}. \quad (3.61)$$

In the current configuration, Almansi strain tensor is defined as [76]:

$$\mathbf{e} = \frac{1}{2} (\mathbf{g} - (\mathbf{b})^{-1}), \quad (3.62)$$

where the total Finger strain tensor is obtained by pull back transformation of metric tensor in reference configuration by total deformation gradient:

$$(\mathbf{b})^{-1} = (\mathbf{F})^{-T} \mathbf{G}^{-1} (\mathbf{F})^{-1}. \quad (3.63)$$

The elastic Almansi strain tensor is [76]:

$$\mathbf{e}^E = \frac{1}{2} (\mathbf{g} - (\mathbf{b}^E)^{-1}), \quad (3.64)$$

where the elastic left Finger strain tensor is obtained by pull back transformation of metric tensor in reference configuration by elastic deformation gradient:

$$(\mathbf{b}^E)^{-1} = \mathbf{F}^{E-T} \overline{\mathbf{G}}^{-1} \mathbf{F}^{E-1}. \quad (3.65)$$

In this case, the inelastic strain can be defined as [76]:

$$\mathbf{e}^{IN} = \mathbf{e} - \mathbf{e}^E. \quad (3.66)$$

The advantage of such representation of the strain tensors is fact that all strain measures in the neighbourhood point completely defined by difference between current and reference metric tensor relative to any configuration [70].

Elastic and inelastic Hencky strain are defined as [67]:

$$\overline{\mathbf{H}}^E = \frac{1}{2} \ln \overline{\mathbf{C}}^E, \quad \mathbf{h}^E = \frac{1}{2} \ln \mathbf{b}^E \quad (3.67)$$

$$\mathbf{H}^{IN} = \frac{1}{2} \ln \mathbf{C}^{IN} \quad \overline{\mathbf{h}}^{IN} = \frac{1}{2} \ln \overline{\mathbf{b}}^{IN}. \quad (3.68)$$

As it can be noticed in Figure 3.4, total left Hencky strain \mathbf{h} is given with respect to current configuration, as well as elastic left Hencky strain \mathbf{h}^E . Also, inelastic left Hencky strain measure $\overline{\mathbf{h}}^{IN}$ is defined with respect to intermediate configuration.

In that scope, addition of the elastic and inelastic strain tensors is possible in the same configuration [70] (Figure 3.5), so for the correct calculation of the inelastic strain measure in the current configuration, it is possible to subtract the elastic strain from the total strain defined in the same (current) configuration (3.66). So, the transformation strain in current configuration (inelastic strain) can be calculated

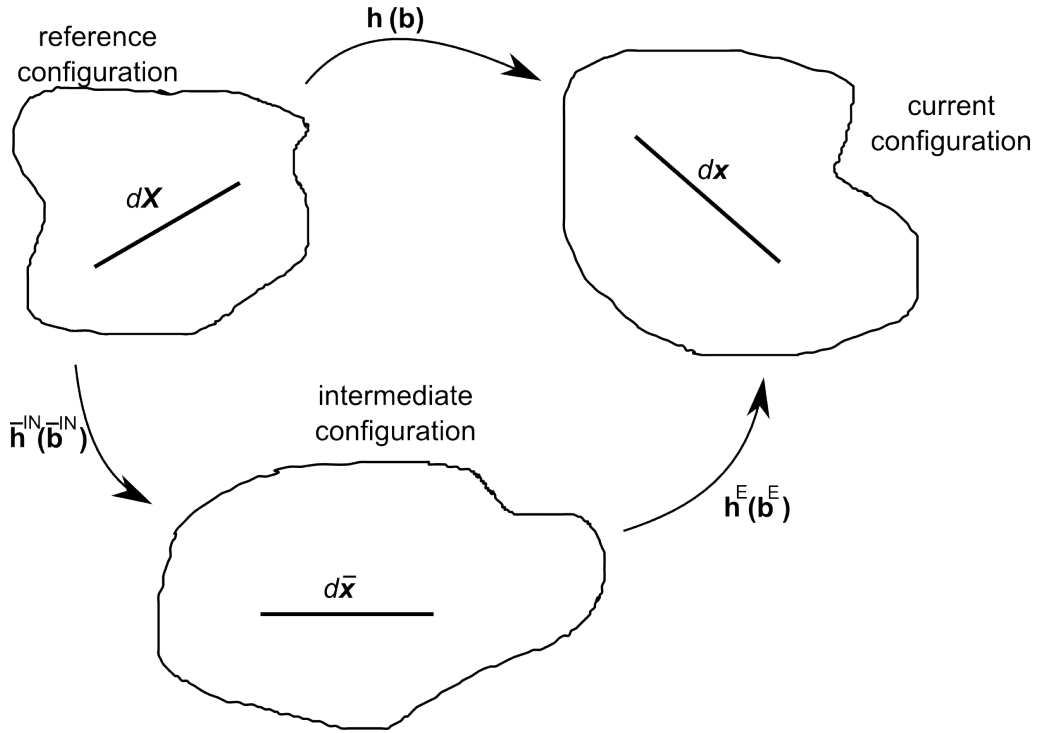


Figure 3.4: Scheme of strain tensors and configurations

from the left Hencky strains as:

$$\mathbf{e}_{tr} = \mathbf{h} - \mathbf{h}^E. \quad (3.69)$$

Relative to constitutive model for metal plasticity, in the SMA case, total transformation strain is needed for the stress integration direction of reverse martensitic transformation what will be discussed in Chapter 4.

3.1.8 Stress tensors

The stress defined in the current configuration is called Cauchy stress tensor $\boldsymbol{\sigma}$ (symmetric tensor) or true stress. Also, the stress can be defined with respect to reference or intermediate configuration. This gives possibility to define alternative stress measures i.e. the stress measure defined in the reference configuration is the first Piola-Kirchhoff (or simply Piola stress) \mathbf{P} which is generally unsymmetric tensor. The relation between the Cauchy and Piola stress is known as Piola transformation [67]:

$$\mathbf{P} = J\boldsymbol{\sigma}\mathbf{F}^{-T}. \quad (3.70)$$

Beside those two stress tensors defined in the known configurations and have physical interpretations, there are other stress tensors used for practical nonlinear analysis.

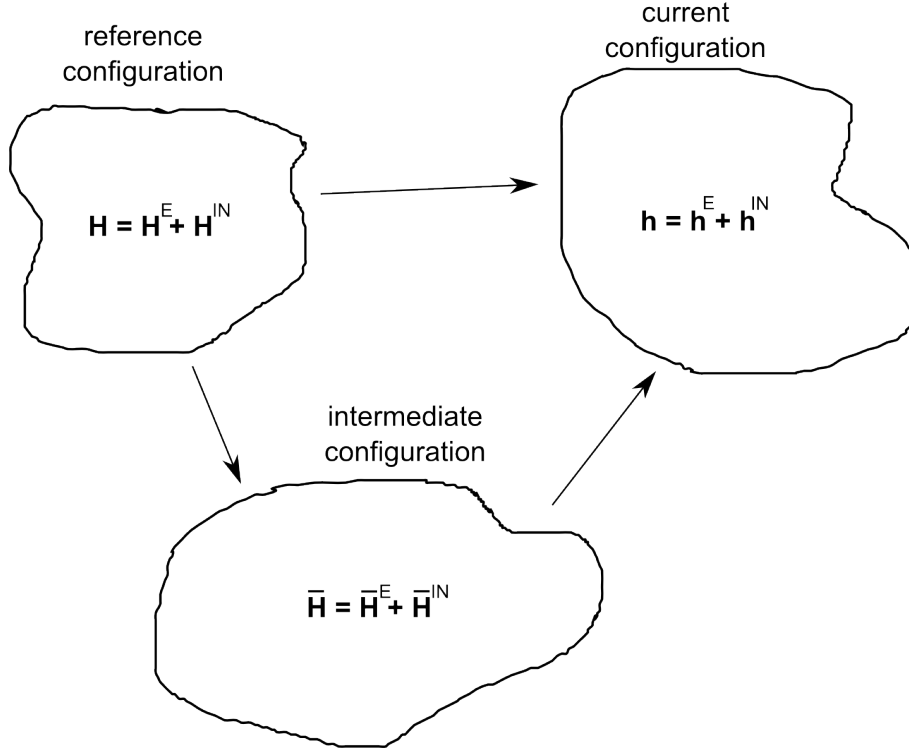


Figure 3.5: Scheme of compatible strain tensors and configurations.

The Kirchhoff stress tensor $\boldsymbol{\tau}$ (symmetric tensor) differs from the Cauchy stress tensor only by the volume ratio J defined by (3.2) [67]:

$$\boldsymbol{\tau} = J\boldsymbol{\sigma}. \quad (3.71)$$

The second Piola-Kirchhoff stress tensor \mathbf{S} is also symmetric and can be obtained by the transformation [67]:

$$\mathbf{S} = \mathbf{F}^{-1}\boldsymbol{\tau}\mathbf{F}^{-T}. \quad (3.72)$$

By the reverse transformation, the Kirchhoff stress can be obtained as [67]:

$$\boldsymbol{\tau} = \mathbf{F}\mathbf{S}\mathbf{F}^{-1}. \quad (3.73)$$

The relationship between the first and the second Piola-Kirchhoff stress tensor can be represented as [67]:

$$\mathbf{P} = \mathbf{F}\mathbf{S}. \quad (3.74)$$

Beside the previous stress measures, one more unsymmetric material stress tensor is defined as:

$$\mathbf{T}_B = \mathbf{R}^T\mathbf{P}. \quad (3.75)$$

The tensor \mathbf{T}_B is known as Biot stress tensor. Other examples of stress tensors [67] are corotated Cauchy stress tensor $\boldsymbol{\sigma}_u$, introduced by Green and Naghdi and the Mandel stress tensor $\boldsymbol{\Sigma}$ which is unsymmetric in general. Those tensors are defined with respect to an intermediate configuration. The relations which describe the corotated Cauchy and the Mandel stress tensors are given as [67]:

$$\boldsymbol{\sigma}_u = J^{-1}\mathbf{U}\mathbf{S}\mathbf{U} = \mathbf{R}^T\boldsymbol{\sigma}\mathbf{R} \quad (3.76)$$

$$\boldsymbol{\Sigma} = \mathbf{C}\mathbf{S}. \quad (3.77)$$

Alternative conjugated (3.78) stress and strain measures [67] gives the equation of the stress power (3.79). The alternative expressions of the energetically conjugated pairs of stress and strain are given in [67] as:

$$w_{int}(t) = J\boldsymbol{\sigma} : \mathbf{d} = \mathbf{P} : \dot{\mathbf{F}} = \mathbf{S} : \dot{\mathbf{E}} = \boldsymbol{\Sigma} : \frac{1}{2}\mathbf{C}^{-1}\dot{\mathbf{C}} = J\boldsymbol{\sigma}_u : \mathbf{D}_R = \text{sym}\mathbf{T}_B : \dot{\mathbf{U}}. \quad (3.78)$$

3.1.9 Balance of mechanical energy

The rate of internal mechanical work (stress power) \mathcal{P}_{int} is possible to be defined with respect to (3.78) as [67]:

$$\mathcal{P}_{int}(t) = \int_{{}^t\Omega} \boldsymbol{\sigma} : \mathbf{d}dv = \int_{{}^0\Omega} J\boldsymbol{\sigma} : \mathbf{d}dV, \quad (3.79)$$

where ${}^0\Omega$ is the reference and ${}^t\Omega$ is the current volume, and \mathbf{d} is the rate of deformation tensor. The rate of internal mechanical work per unit reference volume is w_{int} . It describes the work conjugated stress and strain measures (work conjugated pairs (3.78)). The balance of mechanical energy is given as [67]:

$$\dot{\mathcal{K}}(t) = \mathcal{P}_{ext} - \mathcal{P}_{int}, \quad (3.80)$$

where \mathcal{K} is the kinetic energy, \mathcal{P}_{ext} is the rate of external mechanical work and \mathcal{P}_{int} is the rate of internal mechanical work. This means that the rate of kinetic energy change $\dot{\mathcal{K}}$ is equal to the difference between the rate of external \mathcal{P}_{ext} and internal \mathcal{P}_{int} mechanical work.

3.2 Continuum thermodynamics

Continuum which possesses both mechanical and thermal energy has a name a thermodynamic continuum. The quantities which describe the system are thermodynamic state variables. A thermodynamic state function describes a certain state variables; relations which connect state variables are constitutive equations.

3.2.1 The First law of thermodynamics (Balance of Energy)

The first law of thermodynamics defines balance of work done on the continuum body and internal energy in the deformable body. This is introduced as an equality between the rate of the work and the rate of internal energy \dot{U} . The rate of work done on the system can be done by mechanical forces \mathcal{P}_{int} or can be added to the system as heat \mathcal{Q} , so the balance can be presented as [67]:

$$\mathcal{P}_{int}(t) + \mathcal{Q}(t) = \dot{U}(t). \quad (3.81)$$

According to the balance of mechanical energy (3.80), the balance equation is [67]:

$$\dot{K}(t) + \dot{U}(t) = \mathcal{P}_{ext} + \mathcal{Q}(t). \quad (3.82)$$

As it is given in [3, 67] by Lagoudas: "The law of conservation of energy states that the time rate of change of the total energy (kinetic plus internal energy) of a continuum body is equal to the rate at which external mechanical work is done to that body by surface tractions and body forces plus the rate at which thermal energy is added by heat flux, \mathbf{q} and heat sources, q ". The local form is given as [3, 67]:

$$\rho \dot{u} = \boldsymbol{\sigma} : \mathbf{d} - \text{div}(\mathbf{q}) + \rho q, \quad (3.83)$$

where u is the specific internal energy, ρ is the material density, $\boldsymbol{\sigma}$ is the stress tensor and \mathbf{d} is the deformation rate tensor.

3.2.2 The Second law of thermodynamics (Entropy inequality principle)

The direction of the energy transfer cannot be determined according to the First law of thermodynamics (3.83) because it only governs the energy transfer. The Second law of thermodynamics is responsible for the direction of transfer process.

The entropy \mathcal{S} as concept is needed to be introduced. The entropy is important

property described by Clausius in 19th century. The entropy can be described as "the quantitative measure of microscopic randomness and disorder. The difference between the rate of change of entropy $\dot{\mathcal{S}}$ and the rate of entropy input $\tilde{\mathcal{Q}}$ into a body determines the total production of entropy per unit time, which we denote by Γ " [67].

The second law of thermodynamics states that the total production of entropy is always greater than or equal to zero. The mathematical expression is [67]:

$$\Gamma(t) = \dot{\mathcal{S}}(t) - \tilde{\mathcal{Q}}(t) \geq 0. \quad (3.84)$$

The entropy in continuum body is defined as [67]:

$$\mathcal{S}(t) = \int_{\Omega} s(\mathbf{x}, t) dv, \quad (3.85)$$

while the rate of entropy input consists of the entropy transferred across its boundary surface $\partial\Omega$ by Cauchy entropy flux $\tilde{\mathbf{h}}$ and the entropy generated by sources \tilde{r} inside the body [67]:

$$\tilde{\mathcal{Q}}(t) = - \int_{\partial\Omega} \tilde{\mathbf{h}} \cdot \mathbf{n} ds + \int_{\Omega} \tilde{r} dv. \quad (3.86)$$

Now we have explicit form of the second law of thermodynamics as [67]:

$$\Gamma(t) = \int_{\Omega} \dot{s} dv + \int_{\partial\Omega} \tilde{\mathbf{h}} \cdot \mathbf{n} ds - \int_{\Omega} \tilde{r} dv \geq 0. \quad (3.87)$$

As it is stated in [67], the next relations exist:

$$\tilde{\mathbf{h}} = \frac{\mathbf{q}}{T}, \quad \tilde{r} = \frac{q}{T}, \quad (3.88)$$

so the relation (3.87) is now [67]:

$$\Gamma(t) = \int_{\Omega} \dot{s} dv + \int_{\partial\Omega} \frac{\mathbf{q}}{T} \cdot \mathbf{n} ds - \int_{\Omega} \frac{q}{T} dv \geq 0, \quad (3.89)$$

known as the Clausius-Duhem inequality. Using the Gauss transformation of integral [67]:

$$\int_s \mathbf{u} n ds = \int_v \text{div} \mathbf{u} dv, \quad (3.90)$$

and the property of divergence [67]:

$$\operatorname{div} F \mathbf{u} = F \operatorname{div} \mathbf{u} + \mathbf{u} \nabla F, \quad (3.91)$$

this inequality can be expressed in local form as [3]:

$$\rho \dot{s} + \frac{1}{T} \operatorname{div}(\mathbf{q}) - \frac{1}{T^2} \mathbf{q} \cdot \nabla T - \frac{\rho q}{T} \geq 0. \quad (3.92)$$

Based on the physical observation, the heat only flows spontaneously from a hotter material point to a colder one. Because T is always greater of equal zero, inequality of the heat conduction is [3]:

$$\mathbf{q} \cdot \nabla T \geq 0 \quad (3.93)$$

so the maximum of $\mathbf{q} \cdot \nabla T$ is equal to zero, so the term $-\frac{1}{2} \mathbf{q} \cdot \nabla T$ is always equal to zero, so the new form of Clausius-Duhem inequality is:

$$\rho \dot{s} + \frac{1}{T} \operatorname{div}(\mathbf{q}) - \frac{\rho q}{T} \geq 0. \quad (3.94)$$

Substituting the eq. (3.83) into the previous, the Second Law of Thermodynamics is obtained in the stronger Clausius-Planck inequality form [3]:

$$\mathcal{D}_{int} = \frac{1}{\rho} \boldsymbol{\sigma} : \mathbf{d} - \dot{u} + T \dot{s} \geq 0, \quad (3.95)$$

which represents the internal dissipation or local production of entropy.

3.3 Free energy

The constitutive model for any solid material can be derived from a free energy function. There are several alternate forms of thermodynamic potentials which can be obtained by Legendre transformation. The Legendre transformation is a procedure which provides possibility to replace one variable with the conjugated one. The relationships between the internal energy u , enthalpy h and Helmholtz ψ and Gibbs g free energy are given by Holzapfel [67] and Lagoudas [3] as it is presented in Table 3.1.

The time derivative of the Gibbs free energy has following form [3]:

$$\dot{g}(\boldsymbol{\sigma}, T, \zeta) = \dot{u} - \dot{s}T - s\dot{T} - \frac{1}{\rho} \dot{\boldsymbol{\sigma}} : \boldsymbol{\varepsilon} - \frac{1}{\rho} \boldsymbol{\sigma} : \dot{\boldsymbol{\varepsilon}}. \quad (3.96)$$

The Gibbs free energy depends on the stress $\boldsymbol{\sigma}$, the temperature T and the tem-

Table 3.1: Legendre transformation between the thermodynamic potentials [3, 67]

Thermodynamic potential	Symbol	Trasformation
Internal energy	u	u
Enthalpy	h	$h = u - \frac{1}{\rho} \boldsymbol{\sigma} : \boldsymbol{\varepsilon}$
Helmholtz energy	ψ	$\psi = u - sT$
Gibbs energy	g	$g = u - sT - \frac{1}{\rho} \boldsymbol{\sigma} : \boldsymbol{\varepsilon}$

perature gradient $\mathbf{T} = \nabla T$ and the set of internal state variables $\boldsymbol{\zeta}$ [3]. The total \dot{g} derivative of the Gibbs free energy is in that case as follows [3]:

$$\dot{g} = \frac{\partial g}{\partial \boldsymbol{\sigma}} : \dot{\boldsymbol{\sigma}} + \frac{\partial g}{\partial T} \dot{T} + \frac{\partial g}{\partial \mathbf{T}} \cdot \dot{\mathbf{T}} + \frac{\partial g}{\partial \boldsymbol{\zeta}} \cdot \dot{\boldsymbol{\zeta}}. \quad (3.97)$$

The time derivative of the Legendre transformation (3.96) substituted into the second law of thermodynamics (Clausius-Planck inequality) (3.94), gives the following form [3]:

$$-\rho \dot{g} - \dot{\boldsymbol{\sigma}} : \boldsymbol{\varepsilon} - \rho s \dot{T} \geq 0. \quad (3.98)$$

After substitution of (3.97) into the (3.98) it can be obtained:

$$-\rho \left(\frac{\partial g}{\partial \boldsymbol{\sigma}} : \dot{\boldsymbol{\sigma}} + \frac{\partial g}{\partial T} \dot{T} + \frac{\partial g}{\partial \mathbf{T}} \cdot \dot{\mathbf{T}} + \frac{\partial g}{\partial \boldsymbol{\zeta}} \cdot \dot{\boldsymbol{\zeta}} \right) - \dot{\boldsymbol{\sigma}} : \boldsymbol{\varepsilon} - \rho s \dot{T} \geq 0. \quad (3.99)$$

Because $\dot{\mathbf{T}}$ can be positive or negative, (3.99) can be satisfied if $\frac{\partial g}{\partial \mathbf{T}} \equiv 0$. By fixing constant, all but one variable, the following relations are obtained [3]:

$$s = -\frac{\partial g}{\partial T} \quad (3.100)$$

$$\boldsymbol{\varepsilon} = -\rho \frac{\partial g}{\partial \boldsymbol{\sigma}}. \quad (3.101)$$

Substituting the entropy and strain, the Clausius-Planck inequality results in [3]:

$$-\rho \frac{\partial g}{\partial \boldsymbol{\zeta}} \cdot \dot{\boldsymbol{\zeta}} \geq 0. \quad (3.102)$$

The set of internal variables is identified as \mathbf{e}_{tr} , ξ [3], where \mathbf{e}_{tr} is the transformation strain and ξ is the martensitic volume fraction [3]. The Clausius-Planck inequality, (3.99), assumes the following form:

$$\left(-\rho \frac{\partial g}{\partial \mathbf{e}_{tr}} \right) : \dot{\mathbf{e}}_{tr} + \left(-\rho \frac{\partial g}{\partial \xi} \right) \dot{\xi} \geq 0. \quad (3.103)$$

3.4 SMA constitutive model - Lagoudas

The phase transformation model for SMA formulated by Boyd and Lagoudas [34] and Lagoudas [3] is basic framework for this thesis. Thermodynamic potential given by Gibbs free energy function g is defined for the forward and reverse transformation (see Section 1.2). The free energy can be derived in a quadratic polynomial form as [3]:

$$g(\boldsymbol{\sigma}, T) = -\frac{1}{2\rho}\boldsymbol{\sigma} : \mathcal{M} : \boldsymbol{\sigma} - \frac{1}{\rho}\boldsymbol{\sigma} : \boldsymbol{\alpha}(T - T_0) + c \left[(T - T_0) - T \ln\left(\frac{T}{T_0}\right) \right] - s_0T + u_0, \quad (3.104)$$

where T_0 is the reference temperature. The variable $\boldsymbol{\sigma}$ is the Cauchy total stress, T is the temperature of the SMA specimen, ξ is the martensitic volume fraction and \mathbf{e}_{tr} is the transformation strain. The function $f(\xi)$ is a transformation hardening function. The material parameters c , u_0 , s_0 , \mathcal{M} , $\boldsymbol{\alpha}$ are the effective specific heat, the effective specific internal energy, the effective specific entropy, the effective compliance tensor and the effective thermal expansion tensor, respectively. These effective material parameters can be determined using pure phases parameters and the martensitic volume fraction ξ by the rule of mixture.

Using the (3.100), the entropy s and the strain $\boldsymbol{\varepsilon}$ can be obtained as:

$$s = \frac{1}{\rho}\boldsymbol{\sigma} : \boldsymbol{\alpha} + c \ln\left(\frac{T}{T_0}\right) + s_0, \quad (3.105)$$

$$\boldsymbol{\varepsilon} = \mathcal{M} : \boldsymbol{\sigma} + \boldsymbol{\alpha}(T - T_0). \quad (3.106)$$

The basic form of Gibbs free energy (3.104), which depends on internal state variables, presented by Qidwai and Lagoudas [37] is given as follows:

$$g(\boldsymbol{\sigma}, T, \xi, \mathbf{e}_{tr}) = -\frac{1}{2\rho}\boldsymbol{\sigma} : \mathcal{M} : \boldsymbol{\sigma} - \frac{1}{\rho}\boldsymbol{\sigma} : [\boldsymbol{\alpha}(T - T_0) + \mathbf{e}_{tr}] + c \left[(T - T_0) - T \ln\left(\frac{T}{T_0}\right) \right] - s_0T + u_0 + \frac{1}{\rho}f(\xi). \quad (3.107)$$

Using the Legendre transformation (Table 3.1) between Gibbs free energy g , the internal energy u and the first and second law of thermodynamics substituted into the Clausius-Planck inequality, it is shown that in irreversible processes the internal

dissipation of energy is greater or equal zero [3]:

$$\mathcal{D}_{int} = \boldsymbol{\sigma} : \dot{\mathbf{e}}_{tr} + \left(-\rho \frac{\partial g}{\partial \xi} \right) \dot{\xi} \geq 0. \quad (3.108)$$

The main assumption for the evolution of this constitutive model is that "any change in the current microstructural state of the material is strictly a result of a change in the martensitic volume fraction" [3, 28, 34, 37]:

$$\dot{\mathbf{e}}_{tr} = H \mathbf{n}_{tr} \dot{\xi}. \quad (3.109)$$

The transformation direction will be in the direction of the deviatoric stress \mathbf{S}' during the forward transformation, while, during the reverse one, it will be in the direction of transformation strain tensor \mathbf{e}_{tr} [3]:

$$\mathbf{n}_{tr} = \begin{cases} \frac{3}{2} \frac{\mathbf{S}'}{\bar{S}}; & \dot{\xi} > 0 \\ \frac{\mathbf{e}_{tr}}{\bar{e}_{tr}}; & \dot{\xi} < 0 \end{cases}, \quad (3.110)$$

where H is the maximal effective transformation strain.

The deviatoric stress tensor \mathbf{S}' , the effective (von Mises equivalent) stress \bar{S} and the effective transformation strain \bar{e}_{tr} are defined as:

$$\mathbf{S}' = \boldsymbol{\sigma} - \sigma_m \mathbf{I}, \quad (3.111)$$

$$\bar{S} = \sqrt{\frac{3}{2} \mathbf{S}' : \mathbf{S}'}, \quad (3.112)$$

$$\bar{e}_{tr} = \sqrt{\frac{2}{3} \mathbf{e}_{tr} : \mathbf{e}_{tr}}, \quad (3.113)$$

where σ_m is mean stress.

Substituting the (3.109) into the Clausius-Planck inequality (3.108), it can be obtained:

$$\left(\boldsymbol{\sigma} : \mathbf{n}_{tr} H - \rho \frac{\partial g}{\partial \xi} \right) \dot{\xi} = \Pi \dot{\xi} \geq 0 \quad (3.114)$$

where Π is the general thermodynamic force. For the given Gibbs free energy (3.107), the explicit evaluation of Π is [3]:

$$\begin{aligned} \Pi(\boldsymbol{\sigma}, T, \xi) = & \boldsymbol{\sigma} : \mathbf{n}_{tr} H + \frac{1}{2} \boldsymbol{\sigma} : \Delta \mathcal{M} : \boldsymbol{\sigma} + \boldsymbol{\sigma} : \Delta \boldsymbol{\alpha} (T - T_0) - \\ & \rho \Delta c \left[(T - T_0) - T \ln \left(\frac{T}{T_0} \right) \right] + \rho \Delta s_0 T - \rho \Delta u_0 - \frac{\partial f(\xi)}{\partial \xi}, \end{aligned} \quad (3.115)$$

where $\Delta\mathcal{M} = \mathcal{M}^M - \mathcal{M}^A$, $\Delta\boldsymbol{\alpha} = \boldsymbol{\alpha}^M - \boldsymbol{\alpha}^A$, $\Delta c = c^M - c^A$, $\Delta s_0 = s_0^M - s_0^A$, $\Delta u_0 = u_0^M - u_0^A$, where A and M detones austenitic and martensitic phases, respectively. Effective properties of the material can be determined as function of the pure phases and the martensitic volume fraction ξ by the rule of mixture [3]:

$$\begin{aligned}\mathcal{M}(\xi) &= \mathcal{M}^A + \xi (\mathcal{M}^M - \mathcal{M}^A) = \mathcal{M}^A + \xi \Delta\mathcal{M}, \\ \boldsymbol{\alpha}(\xi) &= \boldsymbol{\alpha}^A + \xi (\boldsymbol{\alpha}^M - \boldsymbol{\alpha}^A) = \boldsymbol{\alpha}^A + \xi \Delta\boldsymbol{\alpha}, \\ c(\xi) &= c^A + \xi (c^M - c^A) = c^A + \xi \Delta c, \\ s_0(\xi) &= s_0^A + \xi (s_0^M - s_0^A) = s_0^A + \xi \Delta s_0, \\ u_0(\xi) &= u_0^A + \xi (u_0^M - u_0^A) = u_0^A + \xi \Delta u_0.\end{aligned}\tag{3.116}$$

The transformation function Φ is introduced by Lagoudas as [3, 37]:

$$\Phi = \begin{cases} \Pi - Y; & \dot{\xi} > 0 \\ -\Pi - Y & \dot{\xi} < 0 \end{cases}\tag{3.117}$$

where Y is threshold value which depends on transformation hardening function [3, 78]. The transformation function Φ needs to satisfy the condition $\Phi = 0$ during transformation. It represents transformation surfaces for $0 < \xi < 1$ and the two boundary surfaces for $\xi = 0$ and $\xi = 1$ of each transformation surface family [3].

It is important to stress that suggested directions of transformation can be differently implemented depending on applied approach. Using the (3.111), (3.112), (3.113), it is possible to transform the thermodynamic force (3.115) into a scalar form, what allows solving of one nonlinear equation in integration point. Evolution of suggested improvement is given in the next section.

3.5 Evolution of the transformation function

In this terms the decomposition on the deviatoric and mean stress (3.111) can be used in the equation (3.115) with the approximation that the proposed direction of the transformation (3.109) is constant and equal to the value from the beginning of the time step ($\mathbf{S}' = \mathbf{S}'_*$ and $\mathbf{e}_{tr} = {}^t\mathbf{e}_{tr}$).

The first term in the eq. (3.115) can be derived for the forward transformation

($\dot{\xi} > 0$) as:

$$\begin{aligned} \boldsymbol{\sigma} : \mathbf{n}_{tr} H &= (\mathbf{S}' + \sigma_m \mathbf{I}) : \frac{3}{2} H \frac{\mathbf{S}'_*}{\bar{S}_*} = \frac{3H}{2\bar{S}_*} (\mathbf{S}' : \mathbf{S}'_* + \sigma_m \mathbf{I} : \mathbf{S}'_*) = \\ &= \frac{3H}{2\bar{S}_*} \frac{\bar{S}_*}{\bar{S}_*} \mathbf{S}'_* = \frac{\bar{S}_* H \bar{S}_*^2}{\bar{S}_*^2} = H \bar{S}_*. \end{aligned} \quad (3.118)$$

The second term in the eq. (3.115) is the same for both, the forward and reverse transformation, but with different sign. The derivation is given as follows:

$$\begin{aligned} \frac{1}{2} \boldsymbol{\sigma} : \Delta \mathcal{M} : \boldsymbol{\sigma} &= \frac{1}{2} \boldsymbol{\sigma} : (\mathcal{M}^M : \boldsymbol{\sigma} - \mathcal{M}^A : \boldsymbol{\sigma}) = \frac{1}{2} \boldsymbol{\sigma} : (\mathbf{e}^M - \mathbf{e}^A) = \\ &= \frac{1}{2} (\mathbf{S}' + \sigma_m \mathbf{I}) : \left(\frac{\mathbf{S}'}{2G^M} + \frac{\sigma_m \mathbf{I}}{c_m^M} - \frac{\mathbf{S}'}{2G^A} - \frac{\sigma_m \mathbf{I}}{c_m^A} \right) = \\ &= \frac{1}{2} \left(\frac{1}{2} \mathbf{S}' : \mathbf{S}' \left(\frac{1}{G^M} - \frac{1}{G^A} \right) + 3\sigma_m^2 \left(\frac{1}{c_m^M} - \frac{1}{c_m^A} \right) \right) = \\ &= \frac{1}{2} \left(\frac{1}{3} \bar{S}^2 \left(\frac{1}{G^M} - \frac{1}{G^A} \right) + 3\sigma_m^2 \left(\frac{1}{c_m^M} - \frac{1}{c_m^A} \right) \right). \end{aligned} \quad (3.119)$$

The third term in the eq. (3.115) is also the same for both directions of transformation but with different sign and it can be derived as:

$$\begin{aligned} \Delta \boldsymbol{\alpha} : \boldsymbol{\sigma} (T - T_0) &= (\boldsymbol{\alpha}^M - \boldsymbol{\alpha}^A) : (\mathbf{S}' + \sigma_m \mathbf{I}) \Delta T = \\ &= (\mathbf{S}' + \sigma_m \mathbf{I}) : \boldsymbol{\alpha}^M \mathbf{I} \Delta T - (\mathbf{S}' + \sigma_m \mathbf{I}) : \boldsymbol{\alpha}^A \mathbf{I} \Delta T = \\ &= 3\sigma_m (\boldsymbol{\alpha}^M - \boldsymbol{\alpha}^A) \Delta T. \end{aligned} \quad (3.120)$$

In (3.118) and (3.119), we have the effective deviatoric stress \bar{S}_* and the transformation strain \bar{e}_{tr} , the mean stress σ_m and the shear modulus as:

$$G^A = \frac{E^A}{2(1+\nu)} \quad G^M = \frac{E^M}{2(1+\nu)}, \quad (3.121)$$

for austenite and martensite and c_m^A and c_m^M which are 1/3 of bulk modulus K^A and K^M for austenite and martensite phases, respectively:

$$c_m^A = \frac{E^A}{1-2\nu} \quad c_m^M = \frac{E^M}{1-2\nu}. \quad (3.122)$$

The final form of the transformation function is obtained by substituting of

previous equations into (3.117) as:

$$\Phi = \begin{cases} H\bar{S} + \frac{1}{2} \left(\frac{1}{3}\bar{S}^2 \left(\frac{1}{G^M} - \frac{1}{G^A} \right) + 3\sigma_m^2 \left(\frac{1}{c_m^M} - \frac{1}{c_m^A} \right) \right) + 3\sigma_m (\alpha^M - \alpha^A) \Delta T + \\ \quad \rho\Delta s_0 (T - M_s) - \frac{\partial f(\xi)}{\partial \xi}; & \dot{\xi} > 0 \\ -\mathbf{S}'_* : {}^t\mathbf{e}_{tr} \frac{H}{t_{\bar{e}_{tr}}} + 3G\Delta\xi H^2 - \frac{1}{2} \left(\frac{1}{3}\bar{S}^2 \left(\frac{1}{G^M} - \frac{1}{G^A} \right) + 3\sigma_m^2 \left(\frac{1}{c_m^M} - \frac{1}{c_m^A} \right) \right) - \\ \quad 3\sigma_m (\alpha^M - \alpha^A) \Delta T - \rho\Delta s_0 (T - A_f) + \frac{\partial f(\xi)}{\partial \xi}; & \dot{\xi} < 0 \end{cases} \quad (3.123)$$

The integration procedure given in [3] considers the change of integration direction in the time step and calculation of total stress without the decomposition on deviatoric and volumetric part what has negative influence on the implementation efficiency. This integration procedure solves vector equation on the integration point level. The implementation given in [3] is rate formulation, it is necessary to calculate increment of transformation strain and total stress in the time step, using the total strain increment as input variable.

On the other hand, such evolution of transformation function in effective form, it is possible to solve only one scalar nonlinear equation on integration point level. This allows better efficiency of the stress integration and possibility of easy extension of stress integration to large strain problems. Functionality of proposed approach is verified by literature examples results and the comparison to experimental results.

3.6 Hardening functions

Various hardening functions can be used to simulate the behavior of the material more realistically. By choice of the hardening function. it is possible to obtain different shape of the stress-strain dependence. The hardening functions $f(\xi)$ are take into account the interaction between the phases and martensite variants [3]. Various hardening functions influence the different simulation results for the same constitutive model. So, a few hardening functions can be found in the literature:

- the exponential model proposed by Tanaka [3, 79]

$$f(\xi) = \begin{cases} \frac{\rho\Delta s_0}{a^M} [(1 - \xi) \ln(1 - \xi) + \xi] + (\mu_1 + \mu_2) \xi; & \dot{\xi} > 0 \\ -\frac{\rho\Delta s_0}{a^A} \xi [\ln \xi - 1] + (\mu_1 - \mu_2) \xi; & \dot{\xi} < 0 \end{cases} \quad (3.124)$$

- the cosine model proposed by Liang and Rogers [3, 80]

$$f(\xi) = \begin{cases} \int_0^{\xi} -\frac{\rho\Delta s_0}{a^M} [\pi - \arccos(2\xi - 1)] d\xi + (\mu_1 + \mu_2)\xi; & \dot{\xi} > 0 \\ \int_0^{\xi} -\frac{\rho\Delta s_0}{a^A} [\pi - \arccos(2\xi - 1)] d\xi + (\mu_1 - \mu_2)\xi; & \dot{\xi} < 0 \end{cases} \quad (3.125)$$

- the polynomial model proposed by Boyd and Lagoudas [3]

$$f(\xi) = \begin{cases} \frac{1}{2}\rho b^M \xi^2 + (\mu_1 + \mu_2)\xi; & \dot{\xi} > 0 \\ \frac{1}{2}\rho b^A \xi^2 + (\mu_1 - \mu_2)\xi; & \dot{\xi} < 0 \end{cases} \quad (3.126)$$

- the smooth hardening function proposed by Machado and Lagoudas [3, 81]

$$f(\xi) = \begin{cases} \frac{1}{2}\rho b^M \left(\xi + \frac{\xi^{n_1+1}}{n_1+1} + \frac{(1-\xi)^{n_2+1}}{(n_2+1)} \right); & \dot{\xi} > 0 \\ \frac{1}{2}\rho b^A \left(\xi + \frac{\xi^{n_3+1}}{n_3+1} + \frac{(1-\xi)^{n_4+1}}{(n_4+1)} \right); & \dot{\xi} < 0 \end{cases} \quad (3.127)$$

In above equations a^M , a^A , μ_1 , μ_2 , ρb^M , ρb^A , n_1 , n_2 , n_3 , n_4 denote transformation hardening parameters available in [3, 81].

For the transformation function, the first derivative of $f(\xi)$ with respect to ξ is necessary. The first derivative of $f(\xi)$ with respect to ξ can be described as follows:

- the exponential model proposed by Tanaka [3, 79]

$$\frac{df(\xi)}{d\xi} = \begin{cases} \frac{\rho\Delta s_0}{a^M} [-\ln(1-\xi)] + (\mu_1 + \mu_2); & \dot{\xi} > 0 \\ \frac{\rho\Delta s_0}{a^A} [\ln \xi - 1] + \frac{\xi}{\xi-1} + (\mu_1 - \mu_2); & \dot{\xi} < 0 \end{cases} \quad (3.128)$$

- the cosine model proposed by Liang and Rogers [3, 80]

$$\frac{df(\xi)}{d\xi} = \begin{cases} -\frac{\rho\Delta s_0}{a^M} [\pi - \arccos(2\xi - 1)] + (\mu_1^c + \mu_2^c); & \dot{\xi} > 0 \\ -\frac{\rho\Delta s_0}{a^A} [\pi - \arccos(2\xi - 1)] + (\mu_1^c - \mu_2^c); & \dot{\xi} < 0 \end{cases} \quad (3.129)$$

- the polynomial model proposed by Boyd and Lagoudas [3]

$$\frac{df(\xi)}{d\xi} = \begin{cases} \rho b^M \xi + (\mu_1 + \mu_2); & \dot{\xi} > 0 \\ \rho b^A \xi + (\mu_1 - \mu_2); & \dot{\xi} < 0 \end{cases} \quad (3.130)$$

- the smooth hardening function proposed by Machado and Lagoudas [3, 81]

$$\frac{df(\xi)}{d\xi} = \begin{cases} \frac{1}{2}\rho b^M (1 + \xi^{n_1} - (1 - \xi)^{n_2}); & \dot{\xi} > 0 \\ \frac{1}{2}\rho b^M (1 + \xi^{n_3} - (1 - \xi)^{n_4}); & \dot{\xi} < 0 \end{cases} \quad (3.131)$$

Chapter 4

Numerical implementation of SMA stress integration procedure

4.1 Basic assumptions

This approach of implementation is motivated by Kojić and Bathe [64], Simo and Hughes [82], Qidwai and Lagoudas [28, 37], Weber and Anand [83], Henann and Anand [84] and Caminero et al. [85]. The most common strategy for implicit stress integration procedure for the rate independent models is the return mapping algorithm [64, 82]. It consists of two steps: (1) prediction of the trial elastic state (elastic predictor) and (2) stress correction due to the phase transformation (inelastic corrector). In [3], the convex cutting plane algorithm is used, what means that the direction of the inelastic corrector is changing during the iterations, while the method presented in [64, 84], that directions keep constant in time step. According to the rate formulation for transformation strain given by equation (3.109), similarly to the rate independent plasticity, the increment of transformation strain in time step is [3]:

$$\Delta \mathbf{e}_{tr} = H \Delta \xi \mathbf{n}_{tr}. \quad (4.1)$$

The trial deviatoric stress \mathbf{S}'_* can be calculated as [64]:

$$\mathbf{S}'_* = 2G \mathbf{e}'_* \quad (4.2)$$

where G is the shear modulus and \mathbf{e}'_* is the trial elastic deviatoric strain. With known increment of the transformation strain $\Delta \mathbf{e}_{tr}$, the final deviatoric stress can be obtained as [64]:

$$\mathbf{S}' = \mathbf{S}'_* - 2G \Delta \mathbf{e}_{tr}. \quad (4.3)$$

Introducing the eq. (4.1), we obtain deviatoric stress for the forward transformation:

$$\mathbf{S}' = \mathbf{S}'_* - 2GH\Delta\xi\mathbf{n}_{tr}. \quad (4.4)$$

According to the relation (3.109), for the forward transformation, we have:

$$\mathbf{S}' = \mathbf{S}'_* - 2GH\Delta\xi\frac{3\mathbf{S}'}{2\bar{S}}, \quad (4.5)$$

$$\mathbf{S}'_* = \mathbf{S}' \left(1 + \frac{3GH\Delta\xi}{\bar{S}} \right), \quad (4.6)$$

$$\mathbf{S}' = \frac{\bar{S}\mathbf{S}'_*}{\bar{S} + 3GH\Delta\xi}. \quad (4.7)$$

Introducing this into the term for effective deviatoric stress, we can derive:

$$\bar{S} = \sqrt{\frac{3}{2}\mathbf{S}' : \mathbf{S}'} = \sqrt{\frac{3}{2}\frac{\bar{S}\mathbf{S}'_*}{\bar{S} + 3GH\Delta\xi} : \frac{\bar{S}\mathbf{S}'_*}{\bar{S} + 3GH\Delta\xi}}, \quad (4.8)$$

$$\bar{S} = \frac{\bar{S}\bar{S}'_*}{\bar{S} + 3GH\Delta\xi}, \quad (4.9)$$

$$\bar{S} = \bar{S}'_* - 3GH\Delta\xi. \quad (4.10)$$

Finally, we obtain that deviatoric stress is derived as:

$$\mathbf{S}' = \frac{\bar{S}\mathbf{S}'_*}{\bar{S}'_*}. \quad (4.11)$$

Using the same procedure, the deviatoric stress and effective stress can be obtained for the reverse transformation as:

$$\mathbf{S}' = \mathbf{S}'_* - 3GH\Delta\xi\frac{\mathbf{e}_{tr}}{\bar{e}_{tr}}, \quad (4.12)$$

$$\bar{S} = \sqrt{\frac{3}{2}\mathbf{S}' : \mathbf{S}'} = \sqrt{\bar{S}'_*^2 - 6GH\Delta\xi\frac{\mathbf{S}'_* : \mathbf{e}_{tr}}{\bar{e}_{tr}} + 9G^2H^2\Delta\xi^2}. \quad (4.13)$$

4.2 Local Newton-Raphson algorithm

The transformation function (3.123) is calculated with the trial deviatoric stress (4.2), the temperature change $\Delta T = T - T_0$ and the assumption that ${}^{t+\Delta t}\xi^{(0)} = {}^t\xi$. The condition ${}^{t+\Delta t}\Phi^{(0)} \leq 0$ is checked for violation [28]. If there is no violation, the elastic solution is accepted as final. If condition ${}^{t+\Delta t}\Phi^{(0)} \leq 0$ is violated, correction

of the solution should satisfy $\Phi = 0$. This condition leads to solution of nonlinear equation by parameter $\Delta\xi$ with appropriate limitations ($0 \leq \xi \leq 1$). The iterative scheme given in Table 4.2 continues until ${}^{t+\Delta t}\Phi^{(k+1)}$ is smaller than some tolerance or ${}^{t+\Delta t}\xi$ reaches a boundary values of 0 or 1.

Table 4.1: Proposed algorithm for decision about transformation direction

-
1. Transformation direction assumed to be the same as in the previous time step
 2. Calculate transformation function ${}^{t+\Delta t}\Phi^{(k)}$ according to formula (3.123)
 3. If ${}^{t+\Delta t}\Phi^{(k)} > tolerance$ then
 - Continue transformation in same direction
 - Else
 - Transformation direction assumed to be in opposite direction
 - Calculate transformation function ${}^{t+\Delta t}\Phi^{(k)}$ according to formula (3.123)
 - If ${}^{t+\Delta t}\Phi^{(k)} > tolerance$ then
 - Continue transformation in new direction
 - Else
 - Solution is elastic - go to the next time step
-

The decision about the direction of the martensitic transformation is important for the correct integration of the transformation function. Firstly, it is assumed that the transformation direction (forward or reverse) is the same as in the previous time step. Then, the transformation function value is calculated with the trial values of stress and strain and value from the previous step of the martensitic volume fraction using the eq. (3.123). If the condition ${}^{t+\Delta t}\Phi \leq 0$ is violated, then the transformation directions is unchanged and the integration procedure is employed. If the condition is not violated, then the transformation function is calculated with the opposite value of ${}^{t+\Delta t}\xi_*$. If the condition ${}^{t+\Delta t}\Phi \leq 0$ is violated now, then the transformation direction is changed. If the condition is not violated again, the solution is elastic and we can proceed to the next time step. The algorithm is given in Table 4.1.

4.3 Stress integration for small strains

In the case of the small strains, the trial elastic deviatoric strain ${}^{t+\Delta t}\mathbf{e}'_*$, the mean strain ${}^{t+\Delta t}e_m$ and the thermal strain ${}^{t+\Delta t}e_{th}$ can be presented as follows:

$${}^{t+\Delta t}\mathbf{e}'_* = {}^{t+\Delta t}\mathbf{e} - {}^{t+\Delta t}e_m \mathbf{I} - {}^t e_{tr} - \Delta {}^{t+\Delta t}e_{tr}, \quad (4.14)$$

$${}^{t+\Delta t}e_m = \frac{1}{3} \sum_{k=1}^3 {}^{t+\Delta t}e_{kk}, \quad (4.15)$$

Table 4.2: Newton-Raphson algorithm for SMA constitutive model

-
1. Let $k = 0$, ${}^{t+\Delta t}\xi^{(0)} = {}^t\xi$, ${}^{t+\Delta t}G^{(0)} = {}^tG$, ${}^{t+\Delta t}\alpha^{(0)} = {}^t\alpha$, ${}^{t+\Delta t}c_m^{(0)} = {}^tc_m$
 2. Calculate transformation function (3.123)

$${}^{t+\Delta t}\Phi^{(k)} = \Phi \left[{}^{t+\Delta t}\mathbf{S}'_*, {}^{t+\Delta t}\xi^{(k)}, {}^{t+\Delta t}T, {}^{t+\Delta t}\sigma_m \right]$$

If ${}^{t+\Delta t}\Phi^{(k)} \leq \textit{tolerance}$ then
 Solution is elastic - go to the next time step
 Else
 Continue to transformation

3. Compute increment of martensitic volume fraction in iteration

$${}^{t+\Delta t}\Phi^{(k)} + d{}^{t+\Delta t}\Phi^{(k)} = {}^{t+\Delta t}\Phi^{(k+1)} = {}^{t+\Delta t}\Phi^{(k)} + \frac{\partial {}^{t+\Delta t}\Phi^{(k)}}{\partial \xi} d{}^{t+\Delta t}\xi^{(k)} \simeq 0$$

$$d{}^{t+\Delta t}\xi^{(k)} = -\frac{{}^{t+\Delta t}\Phi^{(k)}}{\frac{\partial {}^{t+\Delta t}\Phi^{(k)}}{\partial \xi}}$$

4. The step increment of martensitic volume fraction and the current martensitic volume fraction are updated as follows:

$$\Delta {}^{t+\Delta t}\xi^{(k+1)} = \Delta {}^{t+\Delta t}\xi^{(k)} + d{}^{t+\Delta t}\xi^{(k)}$$

$${}^{t+\Delta t}\xi = {}^t\xi + \Delta {}^{t+\Delta t}\xi^{(k+1)}$$

5. Update of the effective deviatoric stress:

$${}^{t+\Delta t}\bar{\mathbf{S}} = \begin{cases} {}^{t+\Delta t}\bar{\mathbf{S}}_* - 3{}^{t+\Delta t}GH\Delta {}^{t+\Delta t}\xi; & \dot{\xi} > 0 \\ \sqrt{{}^{t+\Delta t}\bar{\mathbf{S}}_*^2 - 6{}^{t+\Delta t}GH\Delta {}^{t+\Delta t}\xi \frac{{}^{t+\Delta t}\mathbf{S}'_* \cdot {}^t\mathbf{e}_{tr}}{t\bar{e}_{tr}} + 9{}^{t+\Delta t}G^2H^2\Delta {}^{t+\Delta t}\xi^2}; & \dot{\xi} < 0 \end{cases}$$

Let $k = k + 1$ and go to the step 2.

$${}^{t+\Delta t}e_{th} = {}^{t+\Delta t}\alpha\Delta T, \quad (4.16)$$

where ${}^{t+\Delta t}\alpha$ is the thermal expansion coefficient which depends on ξ . The total strain at the end of time step and the transformation strain from the end of the previous time step are ${}^{t+\Delta t}\mathbf{e}$ and ${}^t\mathbf{e}_{tr}$, respectively. Firstly, by a thermoelastic prediction it is assumed that the transformation strain increment $\Delta {}^{t+\Delta t}\mathbf{e}_{tr}$ is equal to zero (4.14). The trial elastic deviatoric stress ${}^{t+\Delta t}\mathbf{S}'_*^E$ and the mean stress ${}^{t+\Delta t}\sigma_m$ are calculated

with the assumption that there is no phase transformation in the time step:

$${}^{t+\Delta t}\mathbf{S}'_E = 2{}^{t+\Delta t}G{}^{t+\Delta t}\mathbf{e}'_E, \quad (4.17)$$

$${}^{t+\Delta t}\sigma_m = {}^{t+\Delta t}c_m ({}^{t+\Delta t}e_m - {}^{t+\Delta t}e_{th}), \quad (4.18)$$

where ${}^{t+\Delta t}G$ is shear modulus, ${}^{t+\Delta t}c_m$ is bulk modulus which depends on ξ . Now, we proceed to the algorithm given in Table 4.2.

Finally, with known value of martensitic volume fraction ${}^{t+\Delta t}\xi$ and the variables updated during the integration, the deviatoric stress at the end of time step can be calculated as:

$${}^{t+\Delta t}\mathbf{S}'_E = \begin{cases} \frac{{}^{t+\Delta t}\bar{S}^E}{{}^{t+\Delta t}\bar{S}'_E} {}^{t+\Delta t}\mathbf{S}'_E; & \dot{\xi} > 0 \\ {}^{t+\Delta t}\mathbf{S}'_E - 2{}^{t+\Delta t}GH\Delta {}^{t+\Delta t}\xi \frac{{}^t\mathbf{e}_{tr}}{{}^t\bar{e}_{tr}}; & \dot{\xi} < 0 \end{cases}.$$

The total stress and the transformation strain (using the equation (4.1)), at the end of time step are given as:

$${}^{t+\Delta t}\boldsymbol{\sigma} = {}^{t+\Delta t}\mathbf{S}' + {}^{t+\Delta t}\sigma_m \mathbf{I} \quad (4.19)$$

$${}^{t+\Delta t}\mathbf{e}_{tr} = {}^t\mathbf{e}_{tr} + \begin{cases} \frac{3H\Delta {}^{t+\Delta t}\xi}{{}^{t+\Delta t}\bar{S}} {}^{t+\Delta t}\mathbf{S}'; & \dot{\xi} > 0 \\ \frac{H\Delta {}^{t+\Delta t}\xi}{{}^t\bar{e}_{tr}} {}^t\mathbf{e}_{tr}; & \dot{\xi} < 0 \end{cases}. \quad (4.20)$$

This algorithm uses stress decomposed on deviatoric and mean part and with the approximation (4.1) the solution is based on one nonlinear equation. The algorithm is simplified, comparing with the radial return algorithm used in [3] where total stress is used. For such numerical implementation of the stress integration algorithm, in the case of proportional loading, we have exact solution [64, 84]. In the case of arbitrary loading, an error is dependent on time step size. This will be shown and analyzed in the section with numerical examples. Also, this iterative procedure can be used also for large strain problems and it will be described in the next section.

4.4 Stress integration for large strains

By the proposed improvements of stress integration, it is possible to use the small strain procedure to solve large strain problems taking care of geometric relations important for finite strains. Various strain measures correspond to various energetically conjugated stress measures given in (3.78). Choosing a proper strain measure

as input variable, it is necessary to adjust algorithm to correspond to a proper conjugated measure of stress measure. In this section, the stress integration for Eulerian logarithmic strain (Hencky strain) obtained from left Cauchy-Green strain tensor is presented.

Also, it should be stressed that the elastic response will be considered as in case of metal plasticity. The idea is to decompose the deformation gradient into deviatoric and volumetric part using the multiplicative decomposition. In that case, we introduce according to [70, 86], the next relation for modified relative and total deformation gradient ${}^{t+\Delta t}\bar{\mathbf{F}}$ u ${}^{t+\Delta t}\bar{\mathbf{F}}$:

$${}^{t+\Delta t}\bar{\mathbf{F}} = (\det {}^{t+\Delta t}\mathbf{F})^{-\frac{1}{3}} {}^{t+\Delta t}\mathbf{F} \quad {}^{t+\Delta t}\bar{\mathbf{0}}\mathbf{F} = (\det {}^{t+\Delta t}\mathbf{0}\mathbf{F})^{-\frac{1}{3}} {}^{t+\Delta t}\mathbf{0}\mathbf{F}, \quad (4.21)$$

where $\det \bar{\mathbf{F}} = \mathbf{1}$.

The total left Cauchy-Green deformation tensor ${}^{t+\Delta t}\bar{\mathbf{b}}$ can be calculated using the known modified deformation gradient $\bar{\mathbf{F}}$ as [64, 70]:

$${}^{t+\Delta t}\bar{\mathbf{b}} = {}^{t+\Delta t}\bar{\mathbf{F}} {}^{t+\Delta t}\bar{\mathbf{F}}^T. \quad (4.22)$$

Also, the trial elastic left Cauchy-Green deformation tensor ${}^{t+\Delta t}\bar{\mathbf{b}}_*^E$ can be calculated using known data for ${}^{t+\Delta t}\bar{\mathbf{b}}^E$ from previous step [64, 70] as:

$${}^{t+\Delta t}\bar{\mathbf{b}}_*^E = {}^{t+\Delta t}\bar{\mathbf{F}} {}^{t+\Delta t}\bar{\mathbf{b}}^E {}^{t+\Delta t}\bar{\mathbf{F}}^T. \quad (4.23)$$

In the case of logarithmic strains, the total Hencky strain ${}^{t+\Delta t}\mathbf{h}$ and the trial elastic Hencky strain ${}^{t+\Delta t}\mathbf{e}_*^E$ are:

$${}^{t+\Delta t}\mathbf{h} = \frac{1}{2} \ln {}^{t+\Delta t}\bar{\mathbf{b}} = \sum_{k=1}^3 \ln \left({}^{t+\Delta t}\bar{\lambda}_k \right) {}^{t+\Delta t}\mathbf{q}_k {}^{t+\Delta t}\mathbf{q}_k, \quad (4.24)$$

$${}^{t+\Delta t}\mathbf{e}_*^E = {}^{t+\Delta t}\mathbf{h}_*^E = \frac{1}{2} \ln {}^{t+\Delta t}\bar{\mathbf{b}}_*^E = \sum_{k=1}^3 \ln \left({}^{t+\Delta t}\bar{\lambda}_{k*}^E \right) {}^{t+\Delta t}\mathbf{q}_k {}^{t+\Delta t}\mathbf{q}_k, \quad (4.25)$$

where ${}^{t+\Delta t}\bar{\lambda}_k$ and ${}^{t+\Delta t}\bar{\lambda}_{k*}^E$ are the total principal stretches and the trial elastic principal stretches, respectively. ${}^{t+\Delta t}\mathbf{q}_k$ are the corresponding principal directions of the tensors ${}^{t+\Delta t}\bar{\mathbf{b}}$ and ${}^{t+\Delta t}\bar{\mathbf{b}}_*^E$.

For calculation of logarithmic strains, it is necessary to find spectral decomposition of ${}^{t+\Delta t}\bar{\mathbf{b}}$ and ${}^{t+\Delta t}\bar{\mathbf{b}}_*^E$ to find principal stretches ${}^{t+\Delta t}\bar{\lambda}_k$ and ${}^{t+\Delta t}\bar{\lambda}_{k*}^E$ and directions \mathbf{q}_k . The logarithmic strain tensor has many interesting properties. It is known as natural strain measure and is used for direct extension of stress inte-

gration procedure developed for small strain to large strain problems. Also, using the logarithmic strain, it is possible to express volume change using the principal strains. This is important for plasticity and SMA materials because the inelastic deformations are deviatoric.

In this case, according to (3.69), the trial transformation strain, which will be final for the elastic case without phase transformation. The trial transformation strain can be calculated as:

$${}^{t+\Delta t}\mathbf{e}_{tr*} = {}^{t+\Delta t}\mathbf{h} - {}^{t+\Delta t}\mathbf{h}^E_*. \quad (4.26)$$

This transformations strain is used as the direction of stress integration for the reverse martensitic transformation. This assumption defines correct direction of stress integration for the large strain problems.

For known trial elastic state the same integration procedure described for small strain case in Table 4.2 is applied for large strain problems.

Update of the left Cauchy-Green tensor ${}^{t+\Delta t}\mathbf{b}^E$ is defined by exponential mapping of inelastic deformation gradient in citeHenannAnand,Caminero2011:

$${}^{t+\Delta t}\mathbf{F}^{IN} = \exp(\Delta\mathbf{e}_{tr}) {}^t\mathbf{F}^{IN}. \quad (4.27)$$

Inverse relation is given as:

$${}^{t+\Delta t}\mathbf{F}^{IN-1} = {}^t\mathbf{F}^{IN-1} \exp(-\Delta\mathbf{e}_{tr}). \quad (4.28)$$

Using the multiplicative decomposition (3.51), $\mathbf{F}^E = \mathbf{F}\mathbf{F}^{IN-1}$ добија да је:

$${}^{t+\Delta t}\mathbf{F}^E = {}^t\mathbf{F}^E_* \exp(-\Delta\mathbf{e}_{tr}), \quad (4.29)$$

since:

$$\mathbf{F}^E_* = {}^{t+\Delta t}\mathbf{F} {}^t\mathbf{F}^{IN-1}. \quad (4.30)$$

Using the approximations proposed in [84]:

$$\exp(-\Delta\mathbf{e}_{tr}) = (\mathbf{1} - \Delta\mathbf{e}_{tr}), \quad (4.31)$$

it can be shown that:

$${}^{t+\Delta t}\mathbf{b}^E = {}^{t+\Delta t}\mathbf{b}^E_* (\mathbf{1} - 2\Delta\mathbf{e}_{tr}). \quad (4.32)$$

For the case of the logarithmic strain, the update of transformation strain at the

end of time step can be calculated as:

$${}^{t+\Delta t}\mathbf{e}_{tr} = {}^{t+\Delta t}\mathbf{h} - {}^{t+\Delta t}\mathbf{h}^E, \quad (4.33)$$

where

$${}^{t+\Delta t}\mathbf{h}^E = \frac{1}{2} \ln {}^{t+\Delta t}\mathbf{b}^E. \quad (4.34)$$

As it can be noticed, stress integration procedure is the same for small and large strains. The difference is based on geometric relations using the appropriate stress and strain measures. In order to achieve that, the finite strain measures are used, which need to be updated in a proper way. So, using the multiplicative decomposition, polar decomposition and total strain measures in proposed algorithm, it is possible to solve large strain problems easily [64, 84].

Chapter 5

Thermo-mechanical coupling of structural and heat transfer analysis in SMA

It is well known from both experimental investigation and modeling that a thermo-mechanical coupling is very strong in SMA materials, especially at high strain rates, since the process is close to adiabatic conditions [8, 13]. Latent heat production or absorption influence the material temperature increase or decrease responsible for changes of the SMA material characteristics. It was shown in [3] that the latent heat production is strongly correlated with the amount of martensitic phase (the martensitic volume fraction).

5.1 Coupled energy balance equation

Starting with the first and the second law of thermodynamics it was shown that the internal dissipation can be presented by eq. (3.95). By introduction of Gibbs free energy and Legendre transformation, we have obtained the final form of the Clausius-Planck inequality (3.114). From this point of view, it can be proposed that [3]:

$$\Pi\dot{\xi} = \boldsymbol{\sigma} : \mathbf{d} - \rho\dot{u} + \rho T\dot{s}. \quad (5.1)$$

Returning into the first law of thermodynamics, eq. (3.83), we can obtain that [3]:

$$\rho\dot{s}T - \Pi\dot{\xi} = -\text{div}(\mathbf{q}) + \rho q. \quad (5.2)$$

According to eq. (3.100), (3.97) and (3.114), we can define derivative of the entropy \dot{s} as [3]:

$$\dot{s} = -\frac{\partial \dot{g}}{\partial T} = \frac{\partial^2 g}{\partial T \partial \boldsymbol{\sigma}} : \dot{\boldsymbol{\sigma}} + \frac{\partial^2 g}{\partial T^2} \dot{T} + \frac{1}{\rho} \frac{\partial \Pi}{\partial T} \dot{\xi}. \quad (5.3)$$

The Gibbs free energy g and the thermodynamics force Π are given by equations (3.107) and (3.115), respectively. By its derivation in entropy rate relation (5.3), we obtain [3]:

$$\frac{\partial^2 g}{\partial T \partial \boldsymbol{\sigma}} = -\frac{\boldsymbol{\alpha}}{\rho} \quad (5.4)$$

$$\frac{\partial^2 g}{\partial T^2} = -\frac{c}{T} \quad (5.5)$$

$$\frac{1}{\rho} \frac{\partial \Pi}{\partial T} = \frac{1}{\rho} \Delta \boldsymbol{\alpha} : \boldsymbol{\sigma} - \Delta c \ln \left(\frac{T}{T_0} \right) + \Delta s_0. \quad (5.6)$$

The explicit form of the entropy rate can be obtained by substitution in (5.3) [3]:

$$\dot{s} = -\frac{\boldsymbol{\alpha}}{\rho} : \dot{\boldsymbol{\sigma}} - \frac{c}{T} \dot{T} + \left(\frac{1}{\rho} \Delta \boldsymbol{\alpha} : \boldsymbol{\sigma} - \Delta c \ln \left(\frac{T}{T_0} \right) + \Delta s_0 \right) \dot{\xi}. \quad (5.7)$$

Now the eq. (5.2) has the following form [3]:

$$-T \boldsymbol{\alpha} : \dot{\boldsymbol{\sigma}} - \rho c \dot{T} + \left(-\Pi + T \Delta \boldsymbol{\alpha} : \boldsymbol{\sigma} - \rho \Delta c T \ln \left(\frac{T}{T_0} \right) + \rho \Delta s_0 T \right) \dot{\xi} = -\text{div}(\mathbf{q}) + \rho q \quad (5.8)$$

This is thermomechanical coupled energy balance equation for SMA. The first term is related to the influence of stress state on the temperature changes. The second term is related to the specific heat, while the third term show the temperature change with respect to a variation of the martensitic volume fraction. By assuming $\Delta \boldsymbol{\alpha} = 0$ and $\Delta c = 0$ the heat transfer equation has the form:

$$-T \boldsymbol{\alpha} : \dot{\boldsymbol{\sigma}} - \rho c \dot{T} + (-\Pi + \rho \Delta s_0 T) \dot{\xi} = -\text{div}(\mathbf{q}) + \rho q. \quad (5.9)$$

5.2 Thermomechanical coupling and methods

For consideration of thermomechanical coupling a partitioned approach is used [61]. The structural and heat transfer FEM programs are connected using a component based software engineering - CTL [63]. CTL is used to provide communication interface. The CTL has already been used for the partitioned coupling algorithm (fluid-structure interaction) [62]. Using the CTL, the coupling components are independent of location and can be connected through a communication channel such as

Transmission Control Protocol and Internet Protocol (TCP/IP), Message Passing Interface (MPI), Secure Shell (SSH), etc.

The realization thermo-mechanical coupling requires at least two program codes which simulate the heat transfer and the mechanical behaviour of materials, independently. Each of these programs can solve only one kind of a physical phenomena. In order to simulate multiple physical models or multiple simultaneous physical phenomena, the efficient algorithm for communication between the codes has been developed.

For this purpose, the partitioned approach established on the fundamentals of nonlinear Block-Gauss-Seidel numerical procedure for strong coupling [61] is used. The algorithm is based on the exchange of information between the two programs. The solid mechanics program computes the dissipative energy released during the phase transformation (or plastic deformation for plasticity). The energy produces the internal heat which further is used in the heat transfer program for computation of a temperature change. The temperature change influences change of transformation function and thermodynamic force (or material characteristics and additional change of the inelastic strains). The solid mechanics program also computes the thermal strains induced by the temperature change. The interaction effects are accounted for by synchronization of coupled state variables: the martensitic volume fraction (or effective plastic strain) and the temperatures.

5.2.1 Heat transfer program - PAK-T

The heat transfer program of Program za Analizu Konstrukcija, in serbian (PAK) software (PAK-T) [60] provides possibility to solve problems of heat transfer through the solids using FEM with the boundary conditions: convection on the part of the surface, prescribed surface flux, prescribed temperature, radiation, etc. Following the fundamental principle of energy conservation, the following procedure is used to solve the energy balance equation [66, 87]:

$$\frac{dQ}{dt} = \frac{dU}{dt}, \quad (5.10)$$

where Q is the heat added to the system and U is the internal energy. The internal energy change is identified with [87]:

$$\frac{dU}{dt} = \int_V \rho c \frac{dT}{dt} dV, \quad (5.11)$$

where ρ is the material density, c is the specific heat and dV is the elementary volume. The heat energy change can be described as [87]:

$$-\frac{d\mathcal{U}}{dt} = \int_V \operatorname{div} \mathbf{q} dV, \quad (5.12)$$

where \mathbf{q} is heat flux over elementary volume dV .

From the Fourier's Law of heat conduction [87]:

$$\mathbf{q} = -\mathbf{k}\nabla T, \quad (5.13)$$

the energy balance equation is derived as [3]:

$$-\rho c \frac{\partial T}{\partial t} + \nabla^T (\mathbf{k}\nabla T) + q + (q_{dis} - T_0 \alpha c_m \dot{e}_m) = 0, \quad (5.14)$$

where q is the local heat source, \mathbf{k} is the material's conductivity, $\mathbf{T} = \nabla T$ is the temperature gradient and q_{dis} is the elementary dissipative energy. The term $-T_0 \alpha c_m \dot{e}_m$ describes the Gough-Joule effect (piezocalorimetric or thermoelastic effect also known as Lord Kelvin formula) [88] which gives a temperature decrease when the material is under elastic tension and increase under compressive loading [89].

The term in brackets represents dissipative energy defined by eq. (5.15) and thermoelastic effect [88]. The elementary dissipative energy q_{dis} of the phase transformation converted into the heat is given as [3]:

$$q_{dis} = \eta (\Pi - \rho \Delta s_0 T) \dot{\xi}, \quad (5.15)$$

where η is the dissipative factor, Π is the thermodynamic force of the martensitic transformation, $\dot{\xi}$ denotes the martensite volume fraction rate, the product $\rho \Delta s_0$ is the stress influence coefficient and Δs_0 is the difference of effective entropy at zero stress for martensitic and austenitic phase [3]. One can notice that the amount of dissipative energy is proportional to the rate of martensitic volume fraction. The eq. (5.15) describes also the temperature change due to a variation of the martensitic volume fraction, associated with the latent heat of the phase transformation [3]. The energy induced by phase transformation is calculated on an integration point level in the structural analysis program PAK-S. The energy is then transferred via CTL to the program for heat transfer (PAK-T) [60] as an internal heat source. The PAK-T calculates the temperature change and sends it back to the PAK-S for further stress integration. The thermomechanical coupling scheme using the CTL interface

is presented in Figure 5.1.

Multiplying eq.(5.14) by weight function h_I (Galerkin method) [66, 87], it is obtained:

$$\begin{aligned}
 - \int_V \rho c h_I \frac{dT}{dt} dV + \int_V h_I (\nabla^T \mathbf{k} \nabla T) dV + \int_V h_I q dV + \\
 \int_V h_I (q_{dis} - T_0 \alpha c_m \dot{\epsilon}_m) dV = 0 \quad \forall h_I.
 \end{aligned} \tag{5.16}$$

Applying the Green formula on the second integral of equation (5.16) and using the same interpolation functions for the temperature, it can be obtained [87]:

$$\sum_J \left[\int_V h_I (\nabla^T \mathbf{k} \nabla h_J) dV \right] T^J = - \sum_J \left[\int_V (\nabla h_I \mathbf{k} \nabla h_J) dV \right] h_J + \int_S h_I q_n dS, \tag{5.17}$$

where T^J are the nodal temperatures, h_J are the interpolation functions, which means that the temperature at any point of volume is:

$$T(x, y, z) = \sum_J T^J h_J(x, y, z). \tag{5.18}$$

Also, $q_n = \mathbf{n}^T \mathbf{q}$ is the total heat flux on the surface boundary which consists of prescribed heat flux input on part of the surface (q_S), convective flux:

$$q_c = h_c (T_0 - T), \tag{5.19}$$

and radiative flux:

$$q_r = h_r (T_r - T). \tag{5.20}$$

This gives [87]:

$$\int_S h_I q_n ds = Q_I^S + \left(Q_I^c - \sum_J K^c_{IJ} T^J \right) + \left(Q_I^r - \sum_J K^r_{IJ} T^J \right). \tag{5.21}$$

From previous equations, the energy balance is obtained as [87]:

$$\mathbf{C}\dot{\mathbf{T}} + \mathbf{K}\mathbf{T} = \mathbf{Q}, \tag{5.22}$$

where:

$$C_{IJ} = \int_V \rho c h_I h_J dV, \tag{5.23}$$

$$K_{IJ} = K^k_{IJ} + K^c_{IJ} + K^r_{IJ}, \quad (5.24)$$

$$K^k_{IJ} = \int_V \nabla h_I \mathbf{k} \nabla h_J dV, \quad (5.25)$$

$$Q_I = Q_I^q + Q_I^{qs} + Q_I^c + Q_I^r + Q_I^{dis}. \quad (5.26)$$

Discretizing in time by implicit Euler, the nonlinear energy balance equation can be solved in an iterative procedure [87]:

$$\frac{1}{\Delta t} \mathbf{C}^{(i-1)} ({}^{t+\Delta t} \mathbf{T}^{(i-1)} - {}^t \mathbf{T} + \Delta \mathbf{T}^{(i)}) + \mathbf{K}^{(i-1)} ({}^{t+\Delta t} \mathbf{T}^{(i-1)} + \Delta \mathbf{T}^{(i)}) = {}^{t+\Delta t} \mathbf{Q}^{(i-1)}, \quad (5.27)$$

$$\Delta \mathbf{T}^{(i)} = \left(\hat{\mathbf{K}}^{(i-1)} \right)^{-1} {}^{t+\Delta t} \hat{\mathbf{Q}}^{(i-1)}, \quad (5.28)$$

where:

$$\hat{\mathbf{K}}^{(i-1)} = \mathbf{K}^{(i-1)} + \frac{1}{\Delta t} \mathbf{C}^{(i-1)}, \quad (5.29)$$

$${}^{t+\Delta t} \hat{\mathbf{Q}}^{(i-1)} = {}^{t+\Delta t} \mathbf{Q}^{(i-1)} - \mathbf{K}^{(i-1)} {}^{t+\Delta t} \mathbf{T}^{(i-1)} - \frac{1}{\Delta t} \mathbf{C}^{(i-1)} ({}^{t+\Delta t} \mathbf{T}^{(i-1)} - {}^t \mathbf{T}). \quad (5.30)$$

This iterative procedure continues until the temperature increment is greater than some tolerance. Also, upper left indexes t and $t + \Delta t$ denote the previous and current time step, respectively. Note that the coordinates of the element nodes are updated in the current time step according to the mesh deformation obtained from the PAK-S. This means that the temperature gradient and the integration procedure are performed with respect to current configuration.

5.2.2 Structure analysis program - PAK-S

The structure analysis program of PAK software (PAK-S) has possibility to solve linear and nonlinear structural problems. Firstly, we introduce the relations necessary to describe FEM formulation for 3D element. Relation for the interpolation of geometry and displacements are given as [87]:

$$\mathbf{x}_p = \mathbf{H}_{int} \mathbf{x}_n, \quad (5.31)$$

$$\mathbf{u}_p = \mathbf{H}_{int} \mathbf{u}_n, \quad (5.32)$$

where \mathbf{x}_p and \mathbf{u}_p are the position vector and the displacement of the material point, \mathbf{x}_n and \mathbf{u}_n are the position vector and the displacement of the element nodes and \mathbf{H}_{int} is the interpolation matrix. The total strain vector \mathbf{e} is determined in the

material point by the relation [87]:

$$\mathbf{e} = \mathbf{B}\mathbf{u}_n, \quad (5.33)$$

where \mathbf{B} is the matrix of the coordinate derivative of the interpolation function. For the elastic and thermoelastic material, the stress is determined by the constitutive relation:

$$\boldsymbol{\sigma} = \mathbf{C}_{el}(\mathbf{e} - e_{th}\mathbf{I}), \quad (5.34)$$

where \mathbf{C}_{el} is the elastic constitutive matrix and e_{th} is the thermic strain. The equilibrium equations can be derived in the following form [61, 62, 90]:

$$-\mathbf{div}(\boldsymbol{\tau}) = \mathbf{r}_s, \quad (5.35)$$

$$\boldsymbol{\tau} = 2G\mathbf{h} + c_m(\text{tr}\mathbf{h})\mathbf{I}, \quad \mathbf{h} = \ln \mathbf{v}, \quad \mathbf{b} = \mathbf{F}\mathbf{F}^T = \mathbf{v}^2 \quad (5.36)$$

in which "tr" indicates the trace function, $\boldsymbol{\tau}$ is the Kirchhoff stress, \mathbf{h} is the Hencky (logarithmic) strain, \mathbf{F} is the deformation gradient, \mathbf{v} is the left stretch tensor, \mathbf{b} is the left Cauchy-Green deformation tensor and \mathbf{r}_s is the body load.

From this point of view we can define the stiffness matrix of the element as [87]:

$$\mathbf{K} = \int_V \mathbf{B}^T \mathbf{C}_{el} \mathbf{B} dV. \quad (5.37)$$

The forces in the element nodes can be determined from the virtual power equilibrium [87]:

$$\delta \mathcal{P}_{int} = \int_V \delta \mathbf{e}^T \boldsymbol{\sigma} dV = \delta \mathbf{u}_n^T \int_V \mathbf{B}^T \boldsymbol{\sigma} dV = \delta \mathbf{u}_n^T \mathbf{F}_{int}, \quad (5.38)$$

so we have:

$$\mathbf{F}_{int} = \int_V \mathbf{B}^T \boldsymbol{\sigma} dV. \quad (5.39)$$

From here, we obtain that [87]:

$$\mathbf{F}_{int} = \mathbf{K}\mathbf{u}_n. \quad (5.40)$$

So, the displacement \mathbf{u}_n is a linear function of the internal forces vector \mathbf{F}_{int} what means that the eq. (5.40) corresponds to a linear analysis. If that is not a case, we speak about geometric and material nonlinear behavior of the material. Classification of nonlinear behavior can be considered depending on the type of analysis. The formulations are given in Table 5.1.

Table 5.1: Classification of nonlinear analysis [66]

Type of analysis	Formulation	Stress and strain measure
Material-nonlinear-only	Material-nonlinear-only (MNO)	Engineering stress and strain
Large displacement, large rotations, but small strains	Total Lagrangian (TL)	Second Piola-Kirchhoff stress, Green-Lagrange strain
	Updated Lagrangian (UL)	Cauchy stress, Almansi strain
Large displacement, large rotations, and large strains	Total Lagrangian (TL)	Second Piola-Kirchhoff stress, Green-Lagrange strain
	Updated Lagrangian (UL)	Cauchy stress, logarithmic strain

Using the equilibrium (5.35) and the kinematic and constitutive equations (5.36), a nonlinear system of equations is formulated using the standard procedure described in [66]. That system can be solved using the classical iterative Newton-Raphson technique [66, 87] as follows:

$${}^{t+\Delta t}\mathbf{K}^{(i-1)}\Delta\mathbf{u}_n^{(i)} = {}^{t+\Delta t}\mathbf{r}_s - {}^{t+\Delta t}\mathbf{F}_{int}^{(i-1)}, \quad (5.41)$$

$${}^{t+\Delta t}\mathbf{u}_n^{(i)} = {}^{t+\Delta t}\mathbf{u}_n^{(i-1)} + \Delta\mathbf{u}_n^{(i)}, \quad (5.42)$$

with the initial conditions:

$${}^{t+\Delta t}\mathbf{u}_n^{(0)} = {}^t\mathbf{u}_n \quad {}^{t+\Delta t}\mathbf{K}^{(0)} = {}^t\mathbf{K} \quad {}^{t+\Delta t}\mathbf{F}_{int}^{(0)} = {}^t\mathbf{F}_{int}, \quad (5.43)$$

where ${}^{t+\Delta t}\mathbf{K}^{(i-1)}$ is the tangential stiffness matrix of the structure [66], $\Delta\mathbf{u}_n^{(i)}$ is the vector of nodal displacement increment, ${}^{t+\Delta t}\mathbf{r}_s$ is the external force and ${}^{t+\Delta t}\mathbf{F}_{int}^{(i-1)}$ is the internal force.

Depending on the used formulation, two possible approaches can be distinguished: Total Lagrangian (TL) and Updated Lagrangian (UL). In the Total Lagrangian solution scheme, all static and kinematic variables are referred to the initial configuration, while the Updated Lagrangian is based on the same procedure but all variables are referred to the last i.e.. current configuration. More details and comparison of both formulations are given in [66].

Depending on choice of the formulation, the balance equation of the finite element can be [66]:

- Material-nonlinear-only analysis:

$${}^t\mathbf{K}\Delta\mathbf{u}_n = {}^{t+\Delta t}\mathbf{r}_s - {}^t\mathbf{F}_{int}, \quad (5.44)$$

- Total Lagrangian:

$$({}_0^t\mathbf{K}_L + {}_0^t\mathbf{K}_{NL})\Delta\mathbf{u}_n = {}^{t+\Delta t}\mathbf{r}_s - {}_0^t\mathbf{F}_{int}, \quad (5.45)$$

- Updated Lagrangian:

$$({}_t^t\mathbf{K}_L + {}_t^t\mathbf{K}_{NL})\Delta\mathbf{u}_n = {}^{t+\Delta t}\mathbf{r}_s - {}_t^t\mathbf{F}_{int}, \quad (5.46)$$

where:

${}^t\mathbf{K}$, ${}_0^t\mathbf{K}_L$, ${}_t^t\mathbf{K}_L$ - linear stiffness matrices,

${}_0^t\mathbf{K}_{NL}$, ${}_t^t\mathbf{K}_{NL}$ - nonlinear stiffness matrices (geometric).

It should be noted that the linear stiffness matrices can be obtained as:

$$\mathbf{K}_L = \int_V \mathbf{B}^T \mathbf{C} \mathbf{B} dV, \quad (5.47)$$

$$\mathbf{K}_{NL} = \int_V \mathbf{B}_{NL}^T \boldsymbol{\sigma} \mathbf{B}_{NL} dV, \quad (5.48)$$

where:

$$\mathbf{C} = \frac{\partial \boldsymbol{\sigma}}{\partial \mathbf{e}}, \quad (5.49)$$

is the tangent stress-strain matrix. The convergence of the Newton-Raphson scheme is influenced by the correctness of the derivation of tangent stress-strain matrix [64, 66].

5.3 Implementation of partitioned coupling algorithm

5.3.1 Mathematical description

The thermo-mechanical problem needed to be solved by using the partitioned procedure can be generally described as a nonlinear system of equations [90]:

$$f(\mathbf{u}_n, T) = 0, \quad (5.50)$$

$$g(\mathbf{u}_n, T) = 0, \quad (5.51)$$

where f and g are thermal and structural subproblems, respectively. The numerical simulation of the first equation is provided by a PAK-T program, while the numerical simulation of the second equation is done by using the PAK-S program. The exchange of data between these two components happens such that the solution of the thermal subproblem f is temperature T for given displacements \mathbf{u}_n , while solution of the structural subproblem g are displacements \mathbf{u}_n for the temperature T as given parameter. Due to nonlinearity of system given in eq. (5.50), (5.51) the block-Gauss Seidel procedure for coupling is used [61, 90]. The algorithm solves the system in a fixed point iteration form as:

$$T^{k+1} = F(\mathbf{u}_n^k, T^k), \quad (5.52)$$

$$\mathbf{u}_n^{k+1} = G(\mathbf{u}_n^k, T^{k+1}), \quad (5.53)$$

where k is the iteration counter of a global iteration procedure.

In order to compute the influence of the mechanics on the temperature field, the PAK-T requires the knowledge on the dissipative energy which causes the temperature change as an internal source. Therefore, the dissipative energy of martensitic transformation caused by the displacements is calculated in each integration point of the structure and is delivered to the PAK-T as coupled state variable. The energy can be computed as:

$$q_{dis_i}^k = \eta (\Pi_i^k - \rho \Delta s_0 T_i^k) \dot{\xi}_i^k, \quad (5.54)$$

where i is the current number of the integration point, η is the dissipative factor, Π_i^k , T_i^k and $\dot{\xi}_i^k$ are the thermodynamic forces, the temperature and the martensitic volume fraction rate in corresponding iteration and integration point. For the delivered energy, PAK-T computes new temperature distribution in the structure and sends them back to the PAK-S for the correction of the displacements via integration procedure given in Chapter 4. This process repeats until the global convergence criterion:

$$\frac{q_{dis}^k - q_{dis}^{k-1}}{q_{dis}^{k-1}} < tol_W, \quad (5.55)$$

is satisfied. Here, q_{dis}^k is the dissipative energy of whole construction and tol_W is the tolerance which define convergence of global iterations. Finally, the dissipative energy of the whole construction can be evaluated as:

$$q_{dis}^k = \sum_{i=1}^P q_{dis_i}^k \quad (5.56)$$

where P is the total number of integration points.

5.3.2 Implementation

For communication between the heat transfer and structural software components, CTL is used as the most fitting middleware. The component is a unit of distributed program structure that encases its implementation behind an interface which consists of services provided by the component to other components in the system. Although it is based on C++ generic template programming, CTL provides C, FORTRAN or C++ interfaces. The components are independent of location and can be accessed through a communication channel such as TCP/IP, Message Passing Interface (MPI), SSH (Secure Shell), etc.

The realization of coupling is performed by creating the components out of two individual programs by use of CTL. The client application had to be made in C++, which calls the components. For the heat transfer (PAK-T) component, the FORTRAN CTL interface was used even though its functionality is limited, since a FORTRAN code is not object oriented programming language. The CTL C++ interface is employed for the structural component PAK-S, because it needs to receive pointer to an instance of PAK-T object. Also, it was necessary to write a C++ wrapper around PAK-S code, because the PAK-S program is written in FORTRAN. All this had to be done in this manner such that PAK-S component could directly interface the PAK-T component.

The partitioned coupling scheme is given in Figure 5.1. The client application is used for initialization of the components. Firstly, the PAK-T component is initialized and passed to the PAK-S component as an initialization argument. After initialization of the components, the *paksCI_solve_step* function performs one time step in the loop over time steps. The initial temperatures for the current time step are evaluated by calling *paktCI_solve* and further delivered from the PAK-T component via *paktCI_gettemperatures* to PAK-S. At this point, all variables needed for a stress and strain calculation have been acquired. The next block represents the iteration loop within the time step of PAK-S component. At the beginning of each iteration, the stresses and strains are being calculated. At the same time, the dissipative energy is computed for all integration points. Afterwards, the dissipative energy is sent to the PAK-T component, where it is being used as a volumetric heat source. At the end of each iteration, the convergence criterion is evaluated. If the convergence is achieved, the PAK-S component exits the iteration loop and returns to the client loop over time steps. However, in the case that the convergence criterion is not met, the whole procedure is repeated all over again. In order to reduce

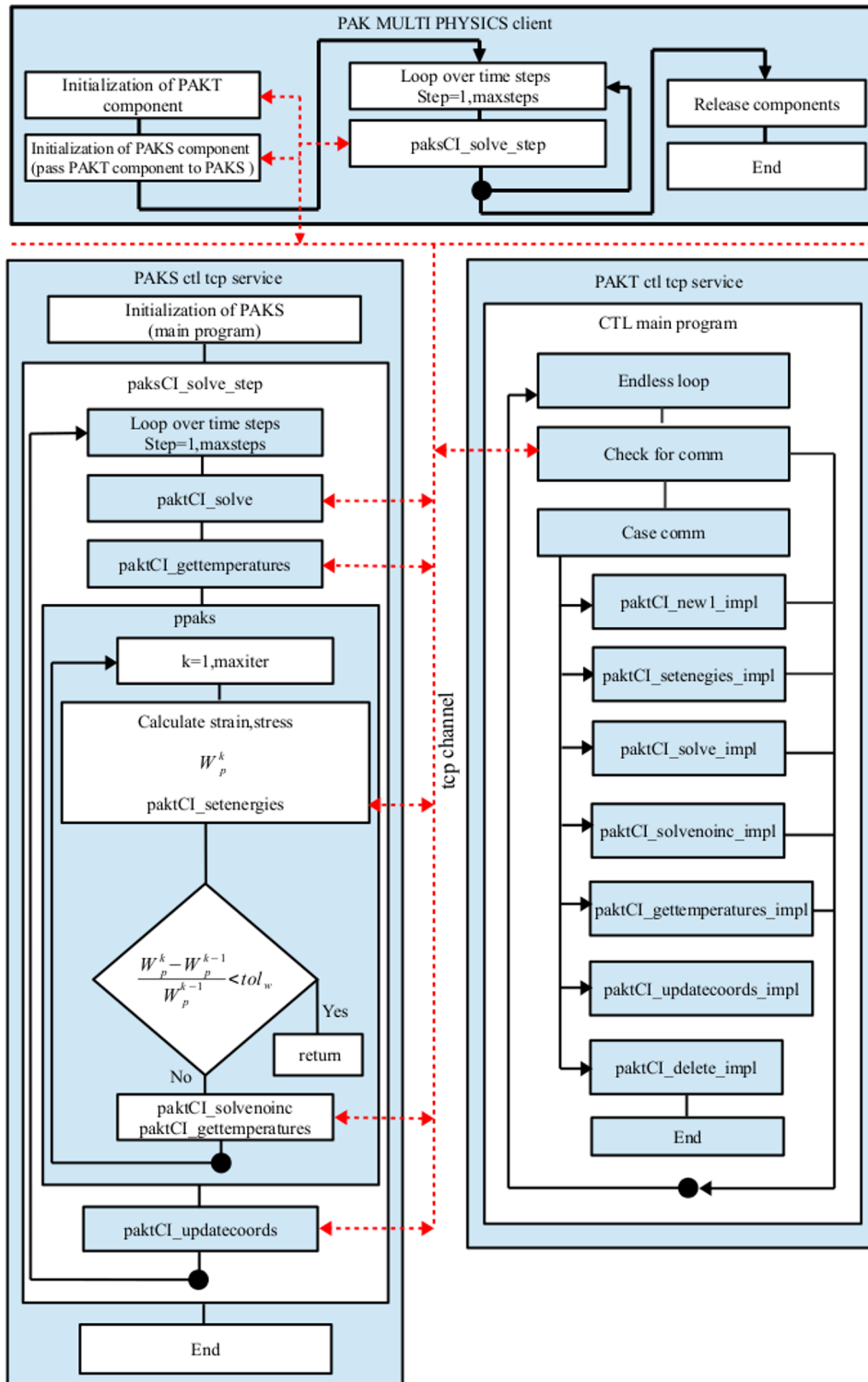


Figure 5.1: Thermo-mechanical coupling scheme using CTL interface (thanks to Nenad Busarac)

the number of iterations, the internal iteration loop of PAK-S component is also used for the global iterations.

Chapter 6

Verification of coupled thermo-mechanical model by comparison to experimental results

6.1 Experimental details of SMA tension tests

The experiments have been conducted on TiNi SMA, produced by Furukawa Electric Co., in IFTR, PAS¹ (Poland) and AIT² (Japan). The TiNi alloy microstructure is obtained from high-resolution Transmission Electron Microscopy (TEM) (Jem 310, JOEL Co.) (Figure 6.1 [8]). As it is noticed by Pieczyska et al. in [8]: "the microstructure was characterized by uniformly distributed, regular grains with a diameter of approximately 80 nm." [16]

The SMA specimens are mechanically loaded and unloaded on electro-mechanical Instron 5867 testing machine at room temperature (approximately 25⁰C) above the A_f temperature, manifesting pseudoelastic behaviour. The machine can be controlled by a force or displacement. In the case of the tests loaded by the stress rates 12.5 MPa/s, 25 MPa/s and 50 MPa/s the machine was controlled by a force. Whereas, for the strain rates 10^{-3} s^{-1} , 10^{-2} s^{-1} and 10^{-1} s^{-1} the machine was controlled by displacement. Several series of loading-unloading cycles have been performed for each experimental test. Furthermore, fast and sensitive FLIR Co infrared camera was used in order to estimate effects of thermomechanical coupling accompanying the Stress Induced Martensitic Transformation (SIMT) [8]. A scheme of the experimental set-up is shown in Figure 6.2, while its photograph in Figure 6.3(a)

¹Institute of Fundamental Technological Research, Polish Academy of Sciences, IPPT PAN

²Aichi Institute of Technology (AIT), Toyota-City

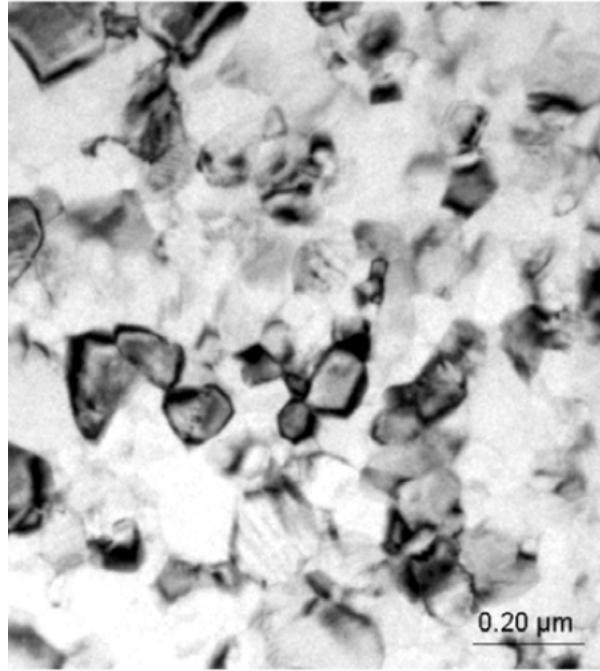


Figure 6.1: TEM image of the TiNi SMA reference state (courtesy of Danuta Stroz, University of Silesia, Poland) [8]

and Figure 6.3(b) presents the TiNi SMA in grips of testing machine [8, 16].

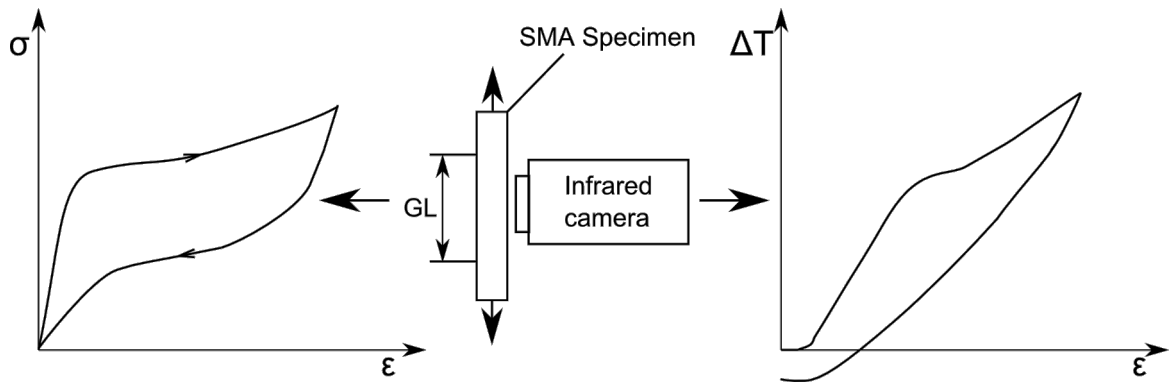


Figure 6.2: Scheme of experimental set-up designed for thermomechanical investigation of SMA (GL denotes gauge length of the testing machine extensometer) [16]

The experimental data received during the SMA tension for various stress- and strain-rates are analyzed by thermo-mechanically coupled FEM modeling, modifying the phenomenological Lagoudas constitutive model [3] implemented into the PAK software for structure [59] and the heat transfer [60] analysis. The results obtained from the experiment and FEM modeling are compared to each other and discussed in this chapter.

Belt type specimens ($160 \text{ mm} \times 10 \text{ mm} \times 0.38 \text{ mm}$), cut from a TiNi SMA (50.5at% Ni) strip have been placed in a specially designed holder in order to pro-

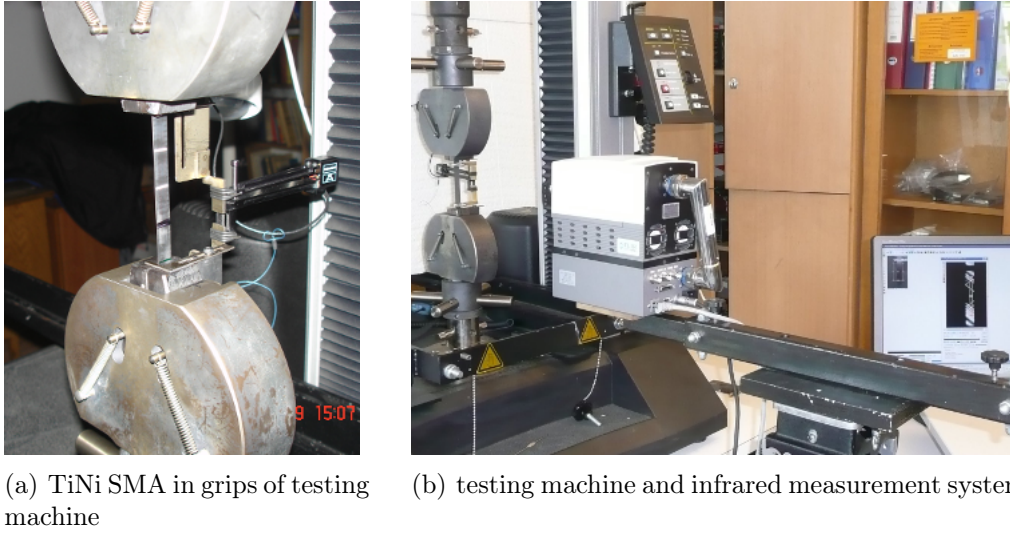


Figure 6.3: Photographs of experimental set-up designed for thermomechanical investigation of SMA [14]

vide a correct functioning of the system composed of TiNi specimen, mechanical extensometer and grips of the testing machine (Figure 6.3) [14, 16]. Mechanical extensometer with parameter 25mm+50% was used. The proper functioning of the measuring system was verified during the initial validation procedure, involving tension tests carried out by using also a laser extensometer, which allows measuring of the strain independently of the testing machine influence [8]. Not until a good agreement between the strain values recorded by the laser and mechanical extensometers were found, the experimental procedure was carried out. Only the mechanical extensometer can be used during the experimental evaluation of the effects of thermomechanical coupling, since the laser beam can influence the infrared measurements. The obtained values of the stress and the strain, presented in the diagrams (Figures 6.5 to 6.16), were related to the current cross-section of the specimen. True stress and true strain values of stress and strain are [16]:

$$\sigma_{true} = \frac{l + \Delta l_0}{l_0 S_0} F, \quad \varepsilon_{true} = \ln \frac{l + \Delta l}{l_0}, \quad (6.1)$$

where l_0 is the length of the specimen prior the loading, Δl is its elongation, S_0 is the area of the specimen cross section and F is the applied force. The infrared camera enables obtaining the temperature changes from the sample surface in various manners: as average value from the chosen area, line, points, etc. The temperature results presented in the diagrams ((Figures 6.5 to 6.16),) were calculated as average from the specimen surface [18]. The temperature changes presented as a function of strain or time indicates current progress of the martensitic forward and reverse

transformation process [16].

6.2 Description of FEM model

The experimentally tested specimens behavior is modelled by the FEM 3D elements [16]. The FEM mesh consists of 400 elements ($80 \times 5 \times 1$) with 972 nodes (Figure 6.4). The dimensions of the model are the same as the dimensions of the experimentally tested specimen given in Section 6.1. Three kinds of possible boundary conditions for such a modeling case are discussed by Yang and Dui in [58]. As one of the appropriate solutions for large metallic grips of the testing machine with respect to the thickness of specimens, the first kind presented in [58] is applied as constant temperature of the specimen ends in the FEM model and the grips of the testing machine are modeled as perfect heat sinks [16]. The working length of the specimen is limited by the testing machine grips to 100 mm, so the 15 rows of elements on the left-hand side of the specimen are fixed and the 15 rows of elements on the right-hand side are loaded. Free convection is prescribed on the elements between the grips, with the convection coefficient adopted according to the literature [58]. The same boundary conditions have been used for all considered tests discussed in this thesis. The same FEM mesh is used for the mechanical and the heat transfer analysis with the boundary conditions shown in Figure 6.4 [16].

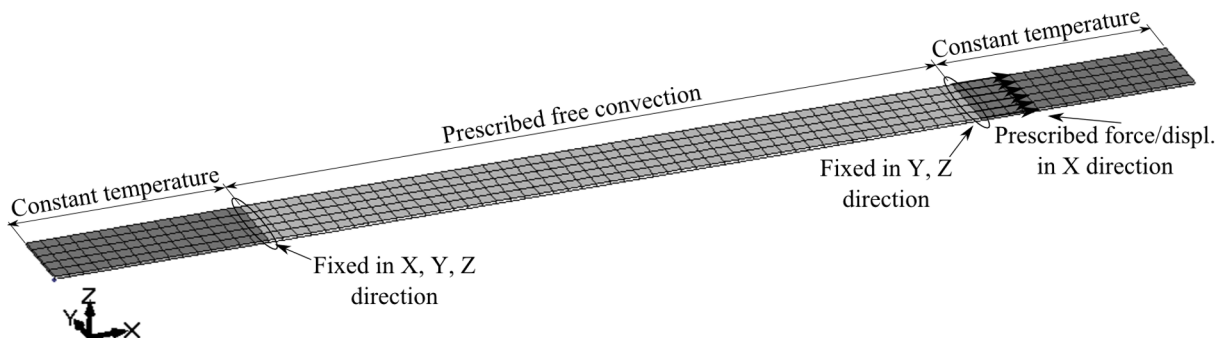


Figure 6.4: Example of the FEM mesh with boundary and loading conditions for tension tests

The TiNi SMA material parameters used for all numerical tests are given in Table 6.1. Identification of the material and thermodynamic parameters for the applied TiNi alloy, necessary for the SMA modeling, was presented by Pieczyska in [13,14]. To this end, a wide program of especially prepared initial experiments was performed, e.g., DSC and additional tension test carried out in a thermal chamber at three various temperatures with low strain rate. From the obtained results, it was

Table 6.1: Material parameters of SMA in stress- and strain- controlled tension tests in Section 6 [16]

E_A	E_M	α_A	α_M
59.2 GPa	45 GPa	$11.0 \cdot 10^{-6} \text{K}^{-1}$	$11.0 \cdot 10^{-6} \text{K}^{-1}$
M_{0s}	M_{0f}	A_{0s}	A_{0f}
213K	209K	270K	276K
H	ν	$\rho \Delta s_A$	$\rho \Delta s_M$
0.06	0.41	$-0.378 \text{ MPa K}^{-1}$	$-0.378 \text{ MPa K}^{-1}$
h	c_p	λ_c	ρ
$6.5 \text{ W m}^{-2} \text{K}^{-1}$	$460 \text{ J kg}^{-1} \text{K}^{-1}$	$18 \text{ W m}^{-2} \text{K}^{-1}$	6.29 g cm^{-3}
n_1	n_2	n_3	n_4
0.2	0.2	0.25	-0.35

possible to define a slope of the SMA phase diagram $c^{M,A}$ which can be presented as $c^{M,A} = \frac{\rho \Delta s_0}{H}$ [78]: where H denotes the maximal effective transformation strain. Martensite start (M_s) and finish (M_f) as well as austenite start (A_s) and finish (A_f) temperatures have been estimated from the results obtained for the TiNi SMA tension test and were compared to the DSC results in [13]. The estimated values of the SMA parameters differ slightly depending on the technique applied, also because that in the DSC process the transformation develops in all directions while during the tension one direction is privileged. For the TiNi SMA used in this research it was found that the A_f equals to approximately 276 K, so it is obvious that the SMA manifests PE behaviour during deformation at room temperature. The smooth hardening function have used exponents n_1, n_2, n_3, n_4 for the desired level of curve smoothness at the start and finish stage of the phase transformation [3]. The given parameters are chosen with respect to the shape of the stress-strain curves obtained during the tension loadings.

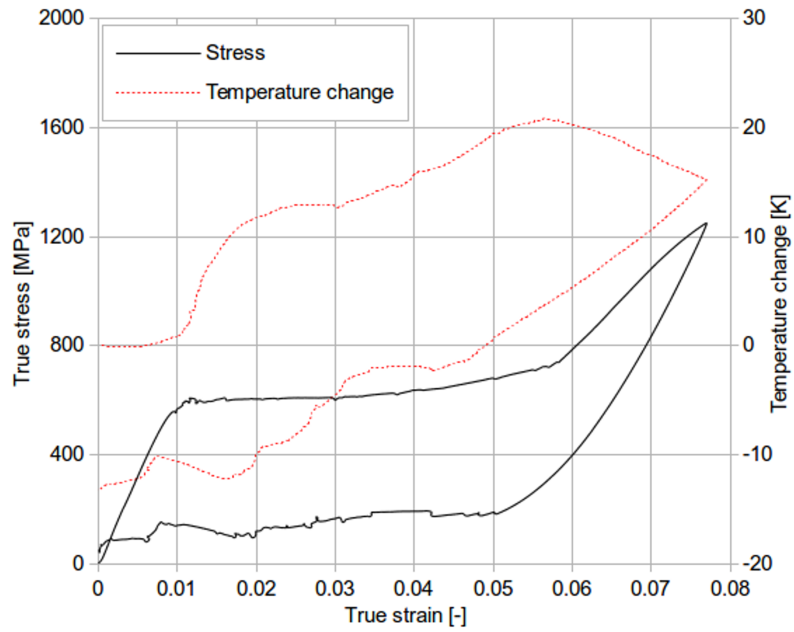
6.3 Experimental and numerical results

The experimental and numerical results of true stress and average temperature changes vs. true strain, obtained during the TiNi SMA tension for various strain and stress rates, are presented in Figures 6.5 to 6.7 and in Figures 6.8 to 6.10, respectively. The obtained diagrams confirm an exothermic character of the forward SIMT and the endothermic character of the reverse one, since the SMA specimen temperature increases during the loading and decreases during the unloading process. At the higher strain rates higher temperature changes are observed, which significantly influences the stress level of the forward and reverse transformation [8].

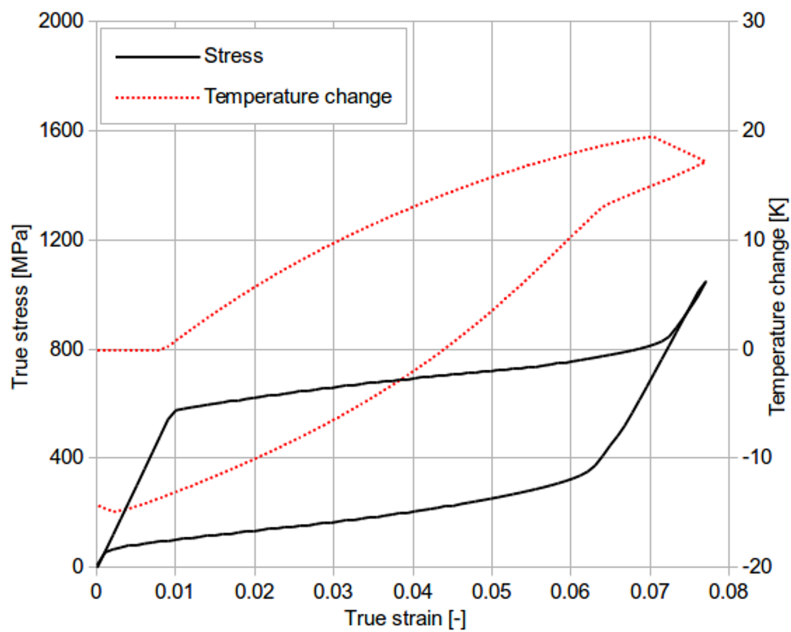
6.3.1 Strain-controlled tension loading: experimental and numerical results

The experimental stress and the average temperature change vs. strain curves of the TiNi SMA, subjected to the loading-unloading tension tests at strain rates of 10^{-3} s^{-1} , 10^{-2} s^{-1} and 10^{-1} s^{-1} are presented in Figures 6.5(a), 6.6(a) and 6.7(a), while their related numerical results in Figures 6.5(b), 6.6(b) and 6.7(b), respectively. Looking at Figure 6.5, one can notice that during the loading the specimen average temperature increases for approximately 20 K. However, at the true strain value of about 0.055 the temperature starts to decrease. That means that the martensitic forward transformation has almost been completed at this stage of the SMA loading: the heat conduction to grips of the testing machine and the heat convection is higher in comparison to the heat production related to the exothermic martensitic forward transformation. In Figure 6.5, it can be noticed that the average temperature of the specimen is lower than the initial temperature after the end of the reverse transformation. At the higher strain rate, e.g. 10^{-2} s^{-1} , the stress-strain loop is much narrower, which was caused by the significant influence of the effects of thermomechanical coupling, e.g. the SMA sample temperature increase for 39 K (Figure 6.6(a)). At the strain rate of 10^{-1} s^{-1} , the stress-strain hysteresis loop is the narrowest (Figure 6.7(a)). A huge temperature increase for 56 K is observed and the temperature change vs. strain curves for the forward and the reverse transformation almost overlap. This indicates that the test was carried out in almost adiabatic conditions.

The maximal total strain applied for the numerical analysis was 8%. All the numerical tests considered for various strain rates were performed in 160 equal time steps with the proper size which depends on the loading rate. The numerical results show the similar qualitative and quantitative behaviour of the stress vs. strain and the average temperature change vs. strain curves for all the tests; Figures 6.5(b), 6.6(b) and 6.7(b) compared to those obtained during the experiment; Figures 6.5(a), 6.6(a) and 6.7(a). It should also be noted that similar values of saturation effect of the martensitic forward transformation were found at the strain rate of 10^{-3} s^{-1} (Figure 6.5). Furthermore, the effects of the transformation saturation were also confirmed by the modeling for the strain rates 10^{-2} s^{-1} and 10^{-1} s^{-1} (Figures 6.6 and 6.7).



(a) experimental results

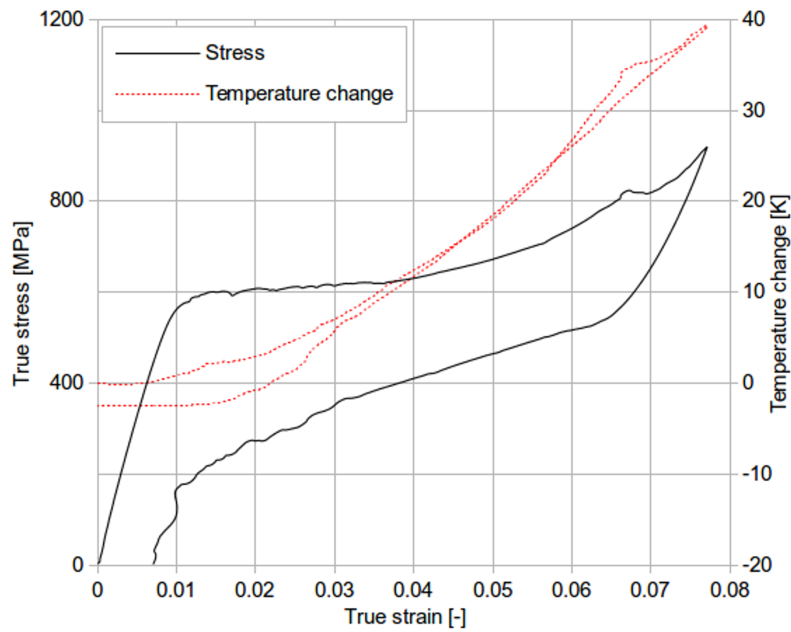


(b) numerical results

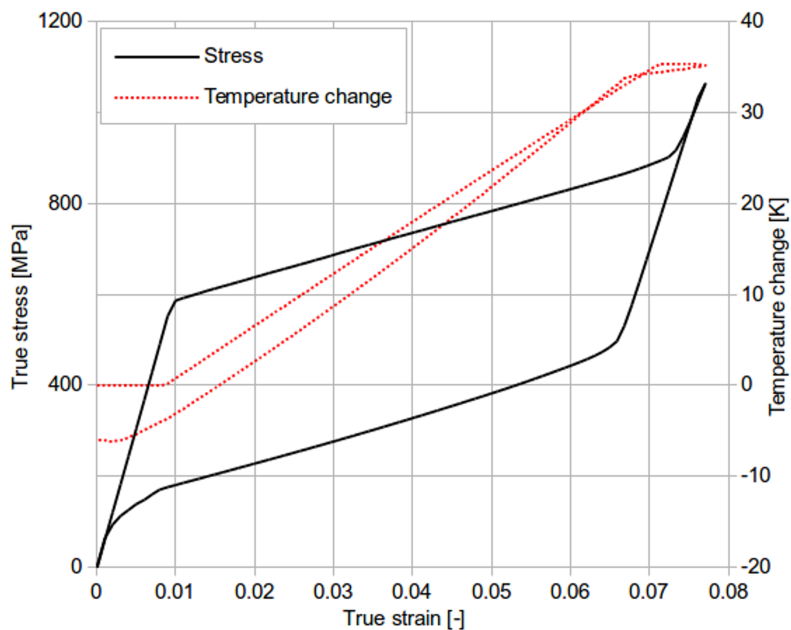
Figure 6.5: Comparison of true stress vs. true strain and temperature change vs. strain curves for TiNi SMA during tension at strain rate 10^{-3}s^{-1} [14, 16]

6.3.2 Force-controlled tension loading: experimental and numerical results

Experimental curves of the stress and the average temperature change vs. strain, obtained for the TiNi SMA subjected to loading-unloading tension cycles at stress



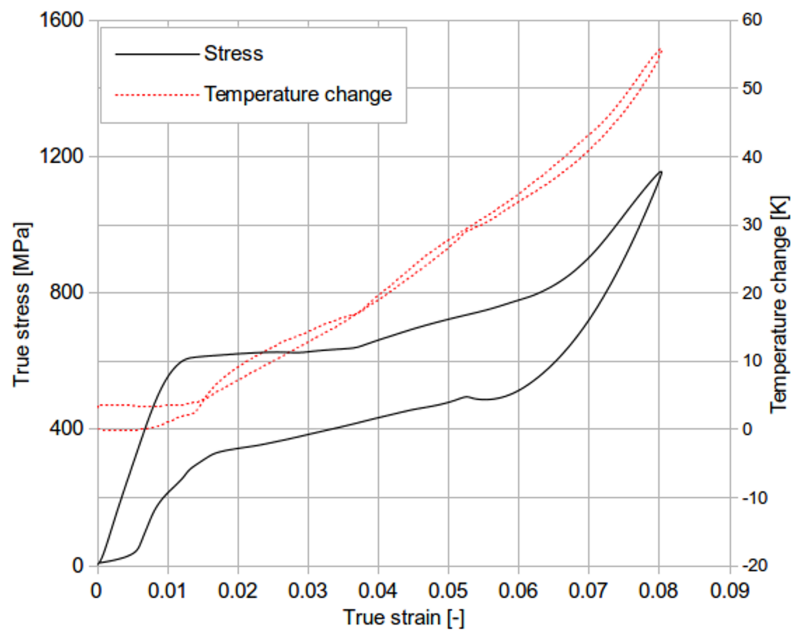
(a) experimental results



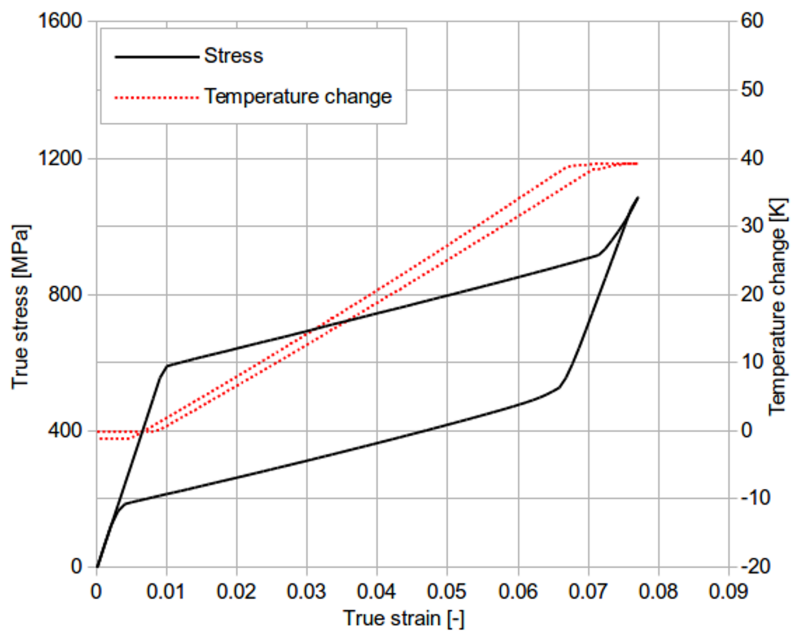
(b) numerical results

Figure 6.6: Comparison of true stress vs. true strain and temperature change vs. strain curves for TiNi SMA during tension at strain rate 10^{-2}s^{-1} [14, 16]

rates 12.5 MPa/s, 25 MPa/s and 50 MPa/s, are presented in Figures 6.8(a), 6.9(a) and 6.10(a), while their related numerical results are shown in Figures 6.8(b), 6.9(b) and 6.10(b), respectively. Similarly to the above presented results, in the initial tension stage the temperature does not change, however it starts to increase slightly even before the stress-strain knee [8, 12–14, 18]. Soon, due to the heat production



(a) experimental results

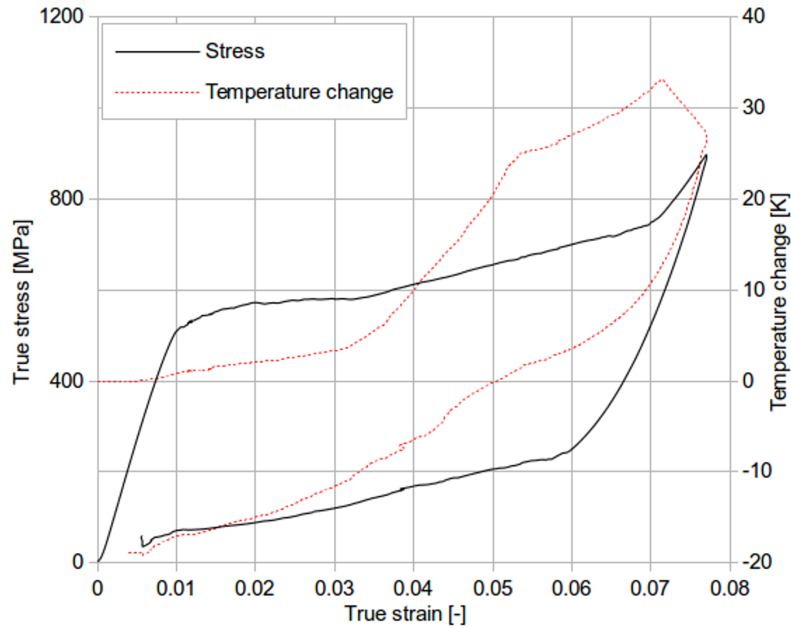


(b) numerical results

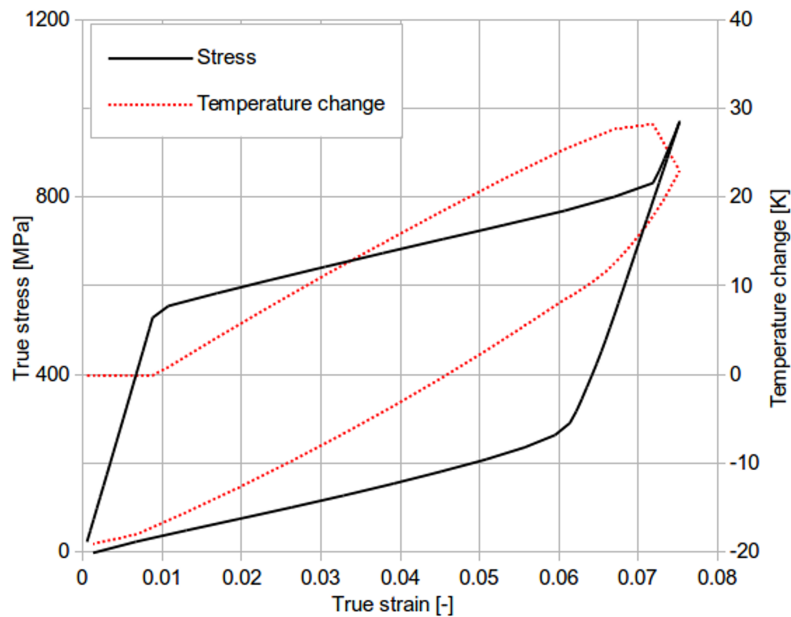
Figure 6.7: Comparison of true stress vs. true strain and temperature change vs. strain curves for TiNi SMA during tension at strain rate 10^{-1}s^{-1} [14, 16]

caused by the exothermic martensitic forward transformation, the average specimen temperature increases very rapidly for 33 K with the stress rate of 12.5 MPa/s (Figure 6.8) and over 40 K for the stress rate 50 MPa/s (Figure 6.10). Moreover, at the advanced state of the transformation, a decrease in the specimen temperature was observed, signalling the saturation stage of the martensitic forward transformation,

similarly to those observed in Figures 6.5 to 6.7 for the strain-controlled tension test.



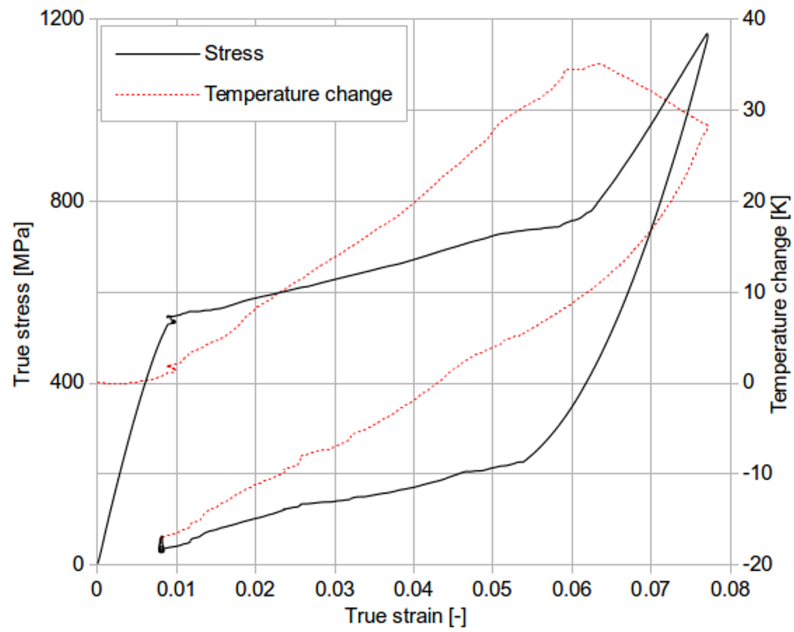
(a) experimental results



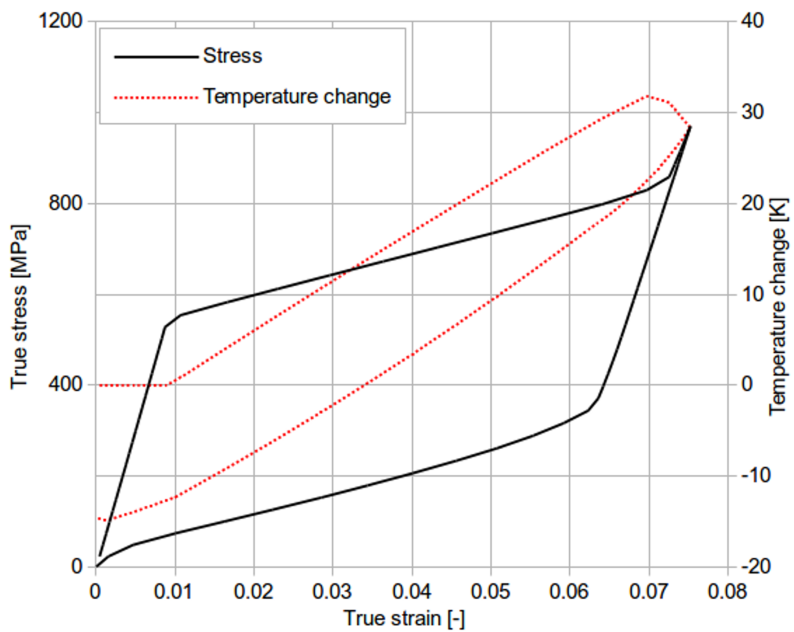
(b) numerical results

Figure 6.8: Comparison of true stress vs. true strain and temperature change vs. strain curves for TiNi SMA during tension at stress rate 12.5 MPa/s [14, 16]

All numerical stress-controlled tests have been performed in 72 equal time steps with the proper size depending on the loading rate; the maximal applied stress was 900 MPa. The numerical analysis gave similar qualitative and quantitative results for stress vs. strain and temperature change vs. strain curves (Figures 6.8(b),



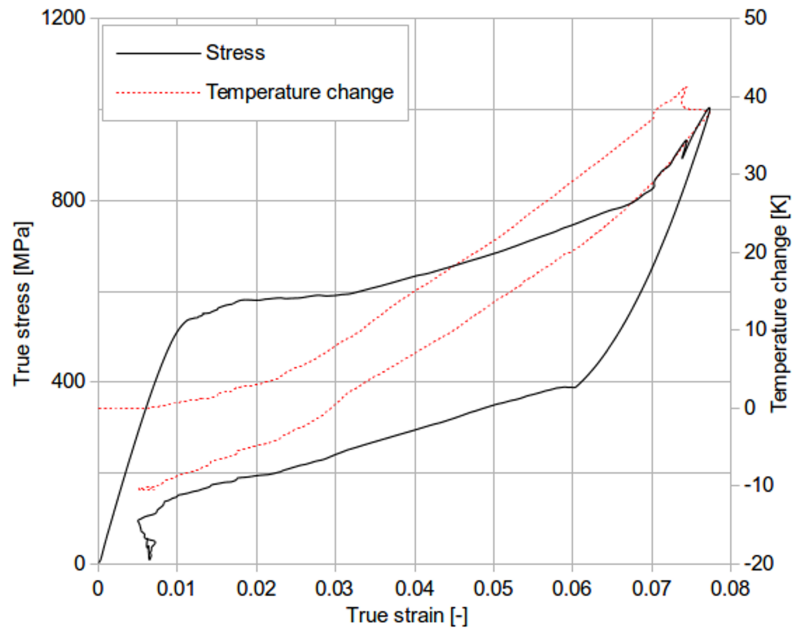
(a) experimental results



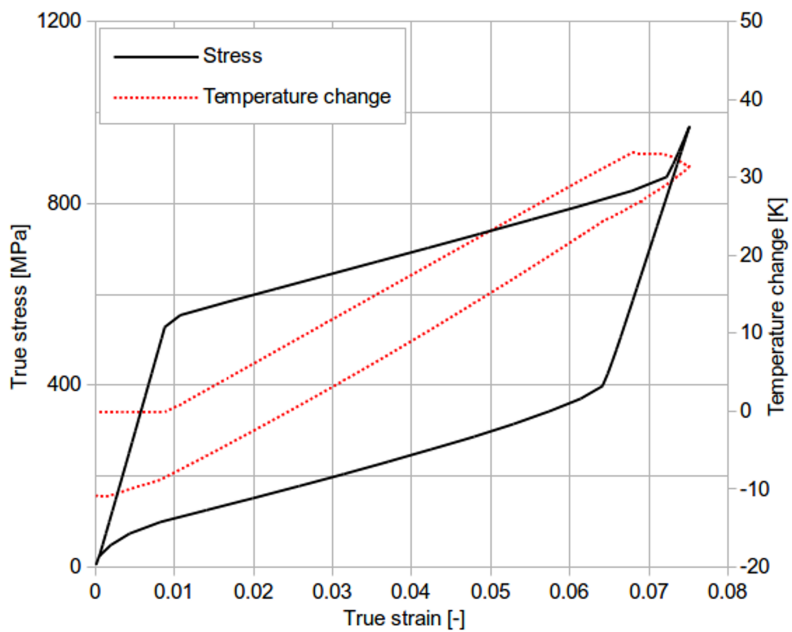
(b) numerical results

Figure 6.9: Comparison of true stress vs. true strain and temperature change vs. strain curves for TiNi SMA during tension at stress rate 25 MPa/s [14, 16]

6.9(b) and 6.10(b)) compared to those found during the experiment (Figures 6.8(a), 6.9(a) and 6.10(a)). Moreover, similar saturation effects of the martensitic forward transformation for both experimental and numerical results have been obtained for all the stress rates applied [8, 16].



(a) experimental results



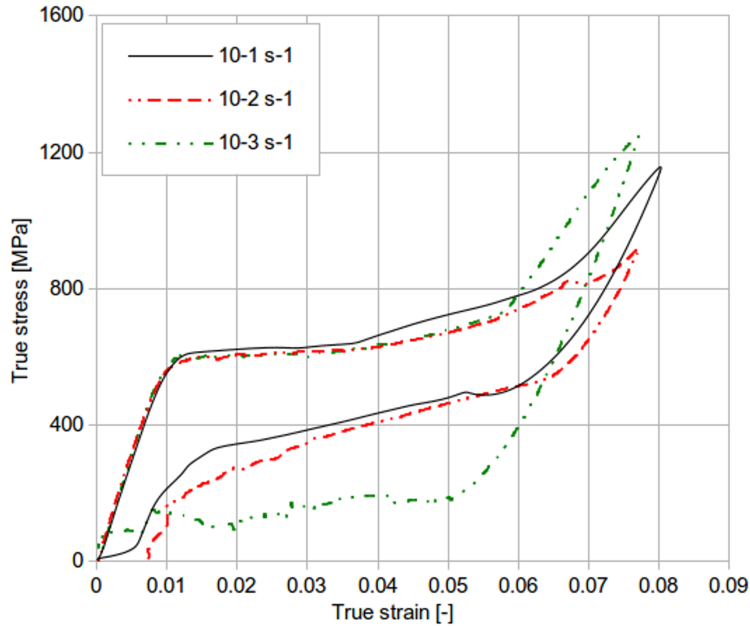
(b) numerical results

Figure 6.10: Comparison of true stress vs. true strain and temperature change vs. strain curves for TiNi SMA during tension at stress rate 50 MPa/s [14, 16]

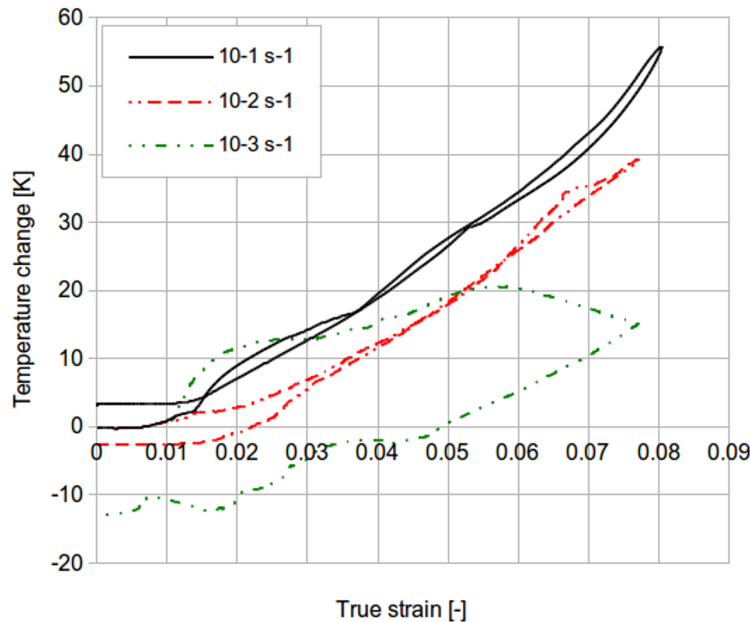
6.4 Discussion of verification results

Comparison of the experimental and numerical results obtained for TiNi SMA during tension, for the various loading, is presented in Figures 6.11 to 6.14. Experimental results of the stress vs. strain comparison is presented in Figures 6.11(a) and 6.13(a),

while their related temperature changes comparison is presented in Figures 6.11(b) and 6.13(b), respectively. Numerical results of the stress vs. strain comparison is presented in Figures 6.12(a) and 6.14(a), while the corresponding comparison of temperature changes vs. strain are shown in Figures 6.12(b) and 6.14(b), respectively [15].

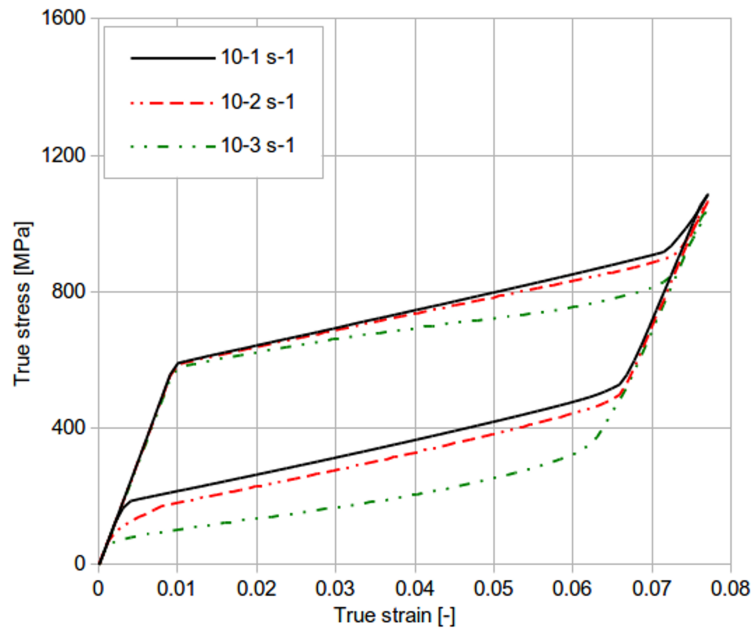


(a) stress vs. strain

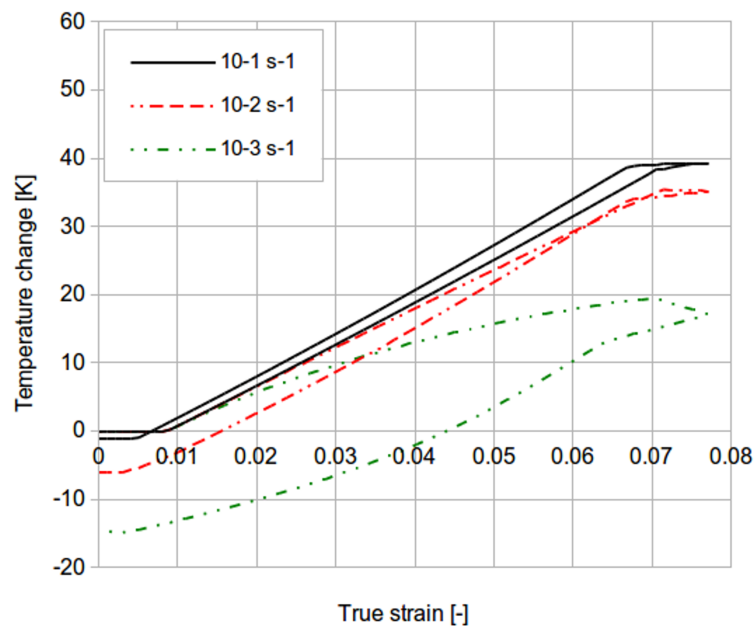


(b) temperature change vs. strain

Figure 6.11: Comparison of experimental curves obtained during TiNi SMA tension at strain rates 10^{-1}s^{-1} , 10^{-2}s^{-1} and 10^{-3}s^{-1} [14, 16]



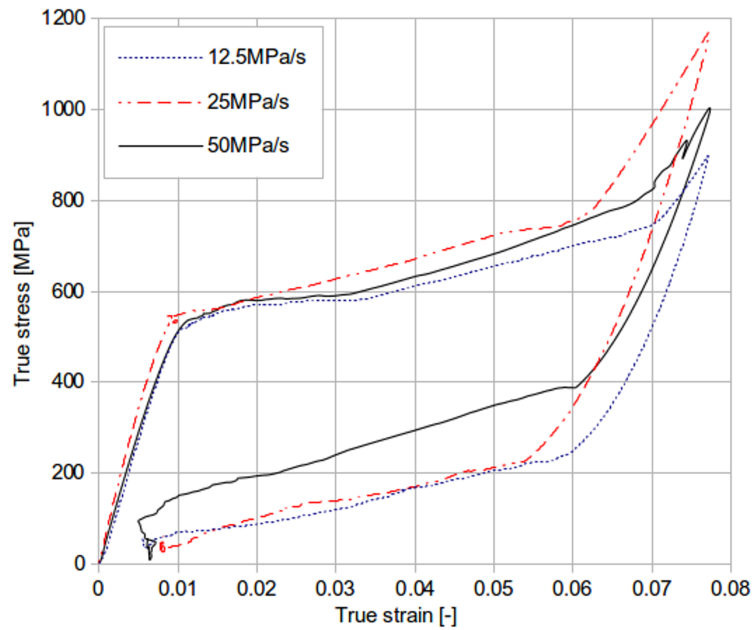
(a) stress vs. strain



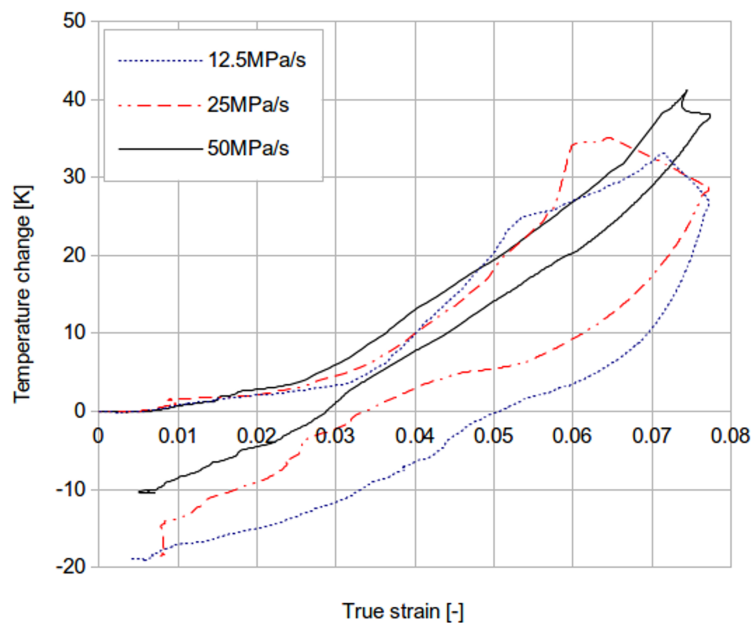
(b) temperature change vs. strain

Figure 6.12: Comparison of numerical curves obtained during TiNi SMA tension at strain rates 10^{-1} s^{-1} , 10^{-2} s^{-1} and 10^{-3} s^{-1} [14, 16]

At the higher loading rates higher values of the stress and temperature change were obtained for all the tests irrespectively of the loading manner (Figures 6.11 to 6.14). The SMA temperature becomes higher since the martensitic forward transformation is accompanied by a huge heat production; in the case of the higher loading rates there is less time for the released heat to be transferred out. As a result, the



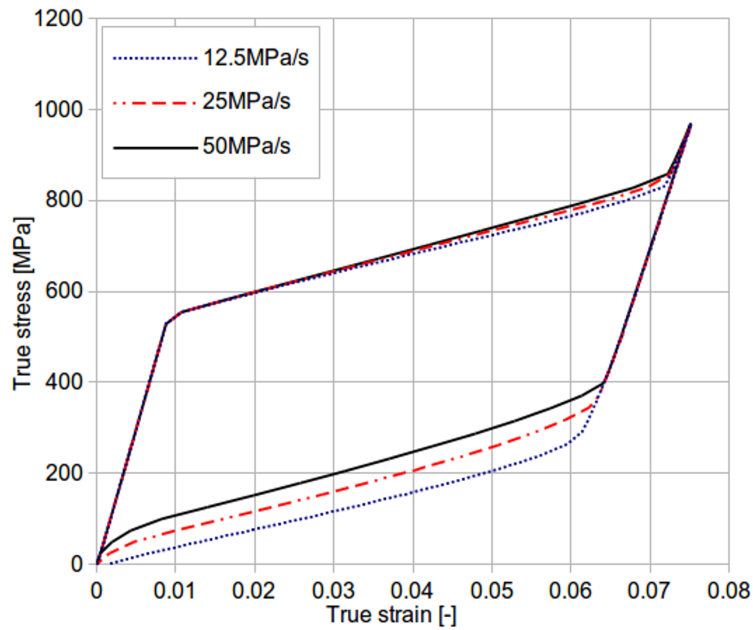
(a) stress vs. strain



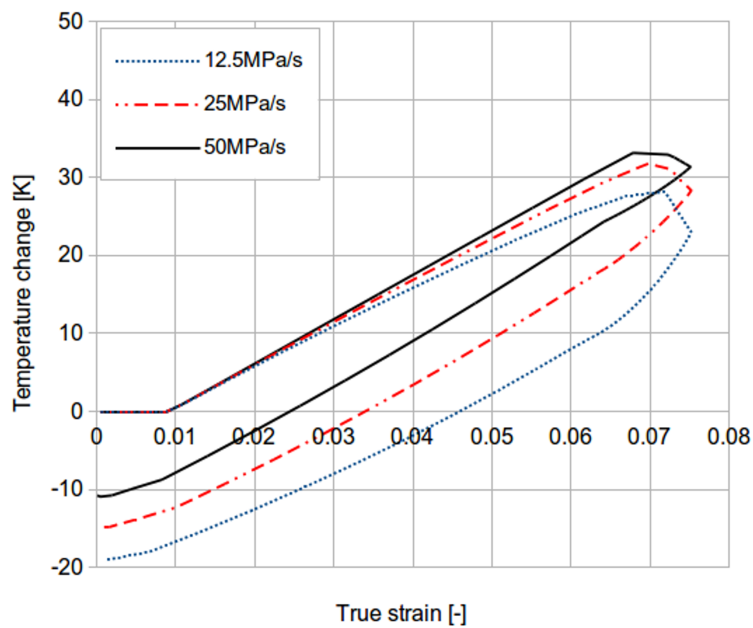
(b) temperature change vs. strain

Figure 6.13: Comparison of experimental curves obtained during TiNi SMA tension at stress rates 12.5 MPa/s, 25 MPa/s and 50 MPa/s [14, 16]

specimen temperature increases, causing a higher level of the stress observed during the SMA loading and a higher slope of the stress-strain curves. The significant temperature increase, accompanying the SMA loading at the higher strain rate, causes the higher level of temperature during the unloading process, which results in a higher stress level of the reverse endothermic transformation and narrower hysteresis



(a) stress vs. strain



(b) temperature change vs. strain

Figure 6.14: Comparison of numerical curves obtained during TiNi SMA tension at stress rates 12.5 MPa/s, 25 MPa/s and 50 MPa/s [14, 16]

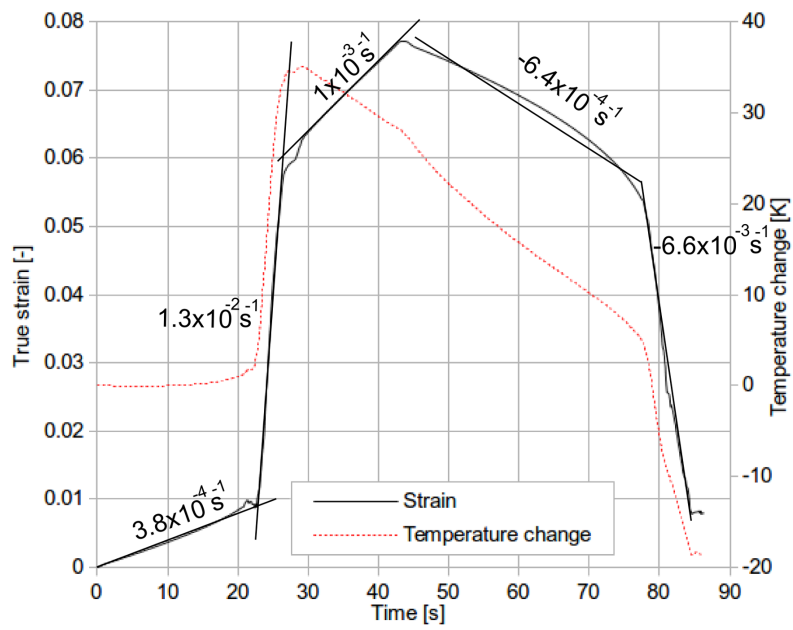
loop. Since the obtained differences of the temperature changes between the forward and the reverse transformation are becoming smaller, the temperature changes vs. strain curves are also narrower (Figures 6.11(b), 6.12(b), 6.13(b) and 6.14(b)). The observed effects point to strong thermomechanical coupling, causing complex mechanical and thermal state during the stress-induced martensitic transformation,

especially when the test conditions become close to adiabatic, i.e. at the higher loading rates [91].

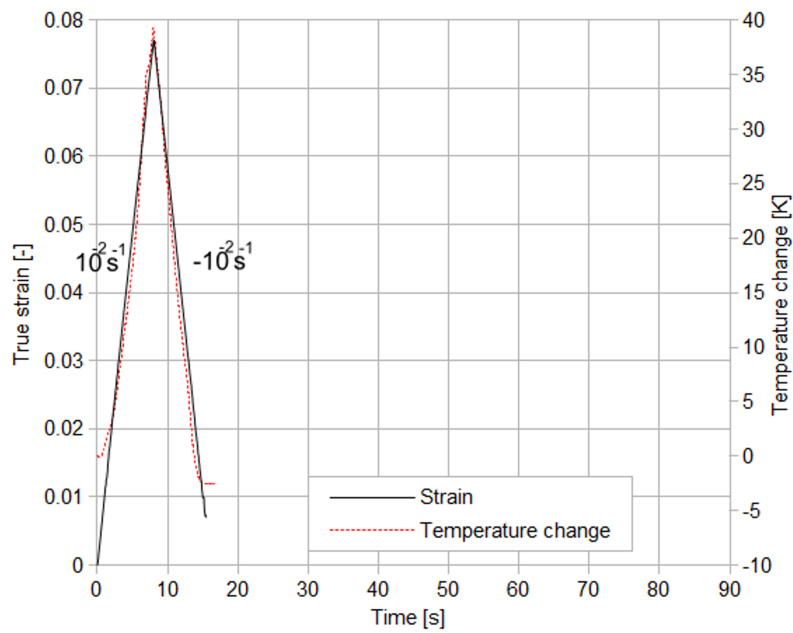
It was also found due to the fast and sensitive infrared camera, that after the SMA unloading the specimen temperature decreases below its initial temperature, quite largely at the lower strain rates (Figures 6.11(b) and 6.13(b)). This thermal effect [8, 18] important for other kind of the SMA application as cooling elements, is also confirmed by the proposed model (Figures 6.12(b) and 6.14(b)). Such results verifies high accuracy of the used equipment and experimental approach, as well as correctness of the applied model.

In order to explain a difference of the SIMT conditions between the two applied experimental approaches (strain and stress-controlled tests) in more details, the strain and temperature changes vs. time for the stress rate 25 MPa/s and strain rate $10^{-2}s^{-1}$ are presented for experimental and numerical case in Figures 6.15 and 6.16, respectively [12]. The graphs prove why such stress and strain rates have been taken into consideration. Namely, the rate of deformation, which seems to be mainly responsible for the transformation conditions, is similar for just these two chosen tests during the main (middle) stage of the SMA loading with strain rate $10^{-2}s^{-1}$, since its estimated value equals to approximately $6.6 \times 10^{-3}s^{-1}$ (Figure 6.16(a)).

One can notice in Figures 6.15 and 6.16 that in the case of the stress rate keeping constant the SMA is deformed with various strain rates. As it was stressed in [8], the stress-controlled tests should assure a constant stress rate, while the strain rate changes according to the transformation progress. The three different stages can be distinguished during the loading with the stress rate 25 MPa/s, according to the strain rate and the transformation progress: the first stage where the strain rate is low, the second with intense growth of the strain rate reflecting intense run of the SIMT and the third stage related to the lower strain rate close to the transformation saturation stage (Figures 6.15(a) and 6.16(a)). For the strain-controlled tests, the strain rate is constant during the loading and unloading process for the forward and reverse transformation and equal to established value of $10^{-2}s^{-1}$ (Figures 6.15(b) and 6.16(b)) [16].

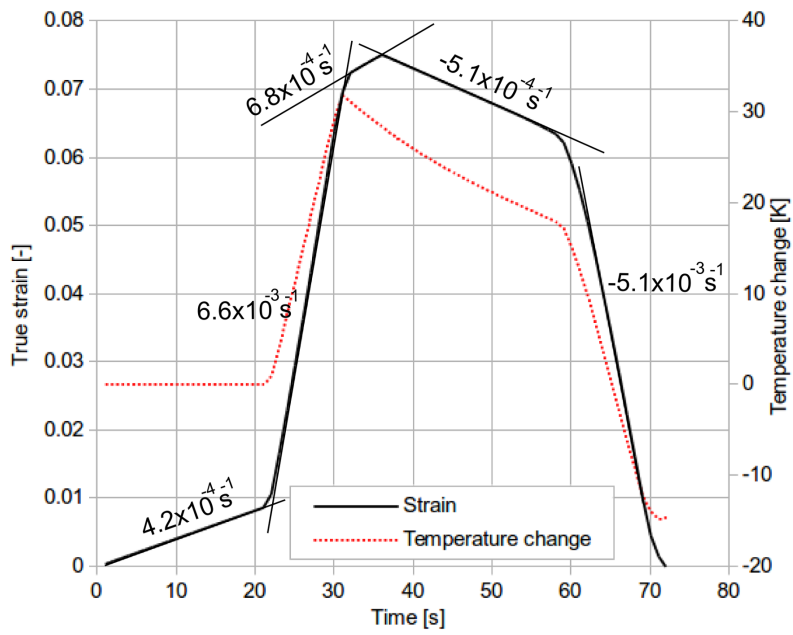


(a)

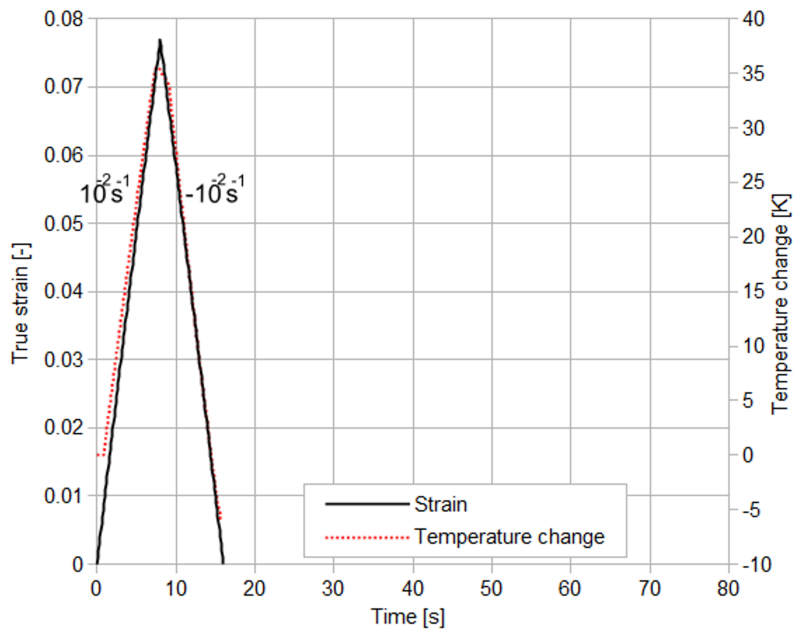


(b)

Figure 6.15: Experimental results. Comparison of strain and temperature change versus time curves for TiNi SMA during tension at (a) stress rate 25 MPa/s and (b) strain rate 10^{-2} s^{-1} [14, 16]



(a)



(b)

Figure 6.16: Numerical results. Comparison of strain and temperature change versus time curves obtained for TiNi SMA during tension at (a) stress rate 25 MPa/s and (b) strain rate 10^{-2} s^{-1} [14, 16]

Chapter 7

Numerical analysis of problems and modeling of real SMA structures

7.1 Numerical analysis of benchmark examples

To verify functionality of the constitutive model and its implementation, the proposed SMA phenomenological effects (pseudoelasticity and SME) need to be successfully simulated. The benchmark examples are intended to verify the correctness of the implemented integration procedure. As introductory tests, the uniaxial tension loading examples are prepared and the obtained results are compared to the literature. The investigation will be extended on multiaxial loading tests from literature to additionally show correctness of the model.

7.1.1 Uniaxial tension loading

The uniaxial tension loading examples are designed according to literature [78]. The unit cube made of SMA has been prepared as 3D FEM model. The model consists of two equal 3D 8-node finite elements. The boundary and loading conditions and the material parameters have been applied according to the literature (Figure 7.1) [3, 78]. The material parameters required for computation are the Young's modulus for austenite and martensite phases E_A and E_M , the thermal expansion coefficients α_A and α_M , the martensite start and finish M_s , M_f as well as austenite start and finish temperatures at zero stress, A_s and A_f , the maximum transformation strain H , the austenite and martensite stress influence coefficients $\rho\Delta s_A$ and $\rho\Delta s_M$. The material parameters from [78], used in those examples, are given in Table 7.1. In addition, for the investigation of the smooth hardening function, the

smooth hardening parameters n_1, n_2, n_3, n_4 are necessary to be chosen. Comments about choosing of smoothness parameters (n_1, n_2, n_3, n_4) also are given.

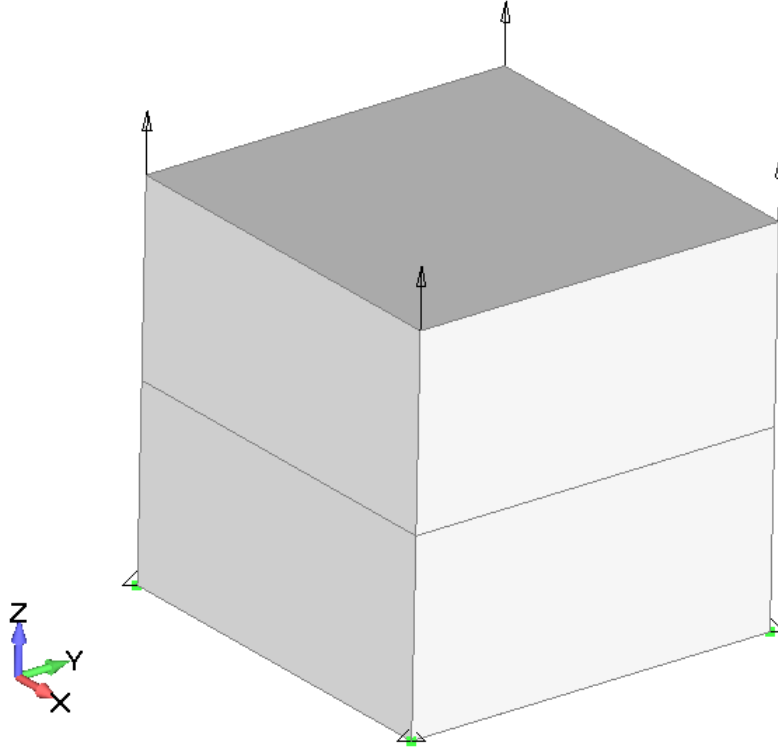


Figure 7.1: The FEM mesh with boundary and loading conditions for uniaxial tension loading examples

Table 7.1: Material parameters of SMA used in uniaxial loading examples [78]

E_A	E_M	α_A	α_M
70.000 MPa	30.000 MPa	$22.0 \cdot 10^{-6} \text{K}^{-1}$	$22.0 \cdot 10^{-6} \text{K}^{-1}$
M_s	M_f	A_s	A_f
291K	271K	295K	315K
H	ν	$\rho \Delta s_A$	$\rho \Delta s_M$
0.05	0.33	-0.35 MPa K^{-1}	-0.35 MPa K^{-1}

Pseudoelasticity effect example

The pseudoelastic behavior of the SMA is expected phenomenological effect in this example. The process is carried out on constant temperature 325 K under isothermal conditions. The temperature is higher than the austenitic finish temperature $A_f = 315 \text{ K}$. The cube is loaded quasi-statically by uniaxial tension stress of $\sigma = 600 \text{ MPa}$ in 100 equal time steps until full martensitic phase is achieved. The material is

then unloaded in 100 equal steps to stress free configuration. As it can be seen in Figure 7.2(a), all transformation strains were fully recovered. The simulation has been done for exponential, cosine and polynomial hardening functions in order to compare the obtained results (Figure 7.2(a)) to the literature results (Figure 7.2(b)). The exactly same results can be noticed looking at the Figure 7.2(a) and Figure 7.2(b).

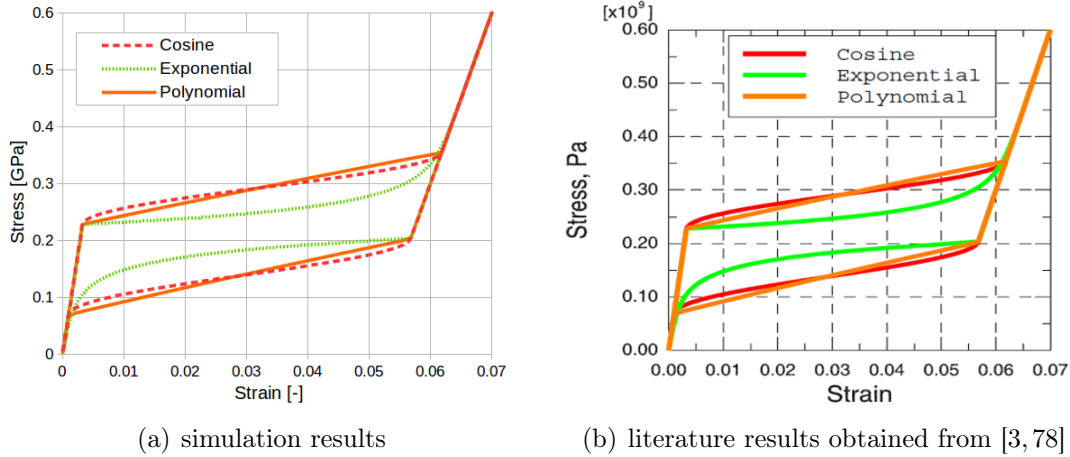


Figure 7.2: Comparison of stress-strain diagrams presenting the SMA pseudoelasticity effect

Furthermore, the polynomial and cosine hardening functions are compared to the smooth hardening function. Using the smooth function, by correction of the smoothness parameters, it is possible to tune the results with respect to experimental measurements. By smooth coefficients variation n_1, n_2, n_3, n_4 the dependence curve behaves in smooth fashion. For the case $n_1 = n_2 = n_3 = n_4 = 1.0$, the obtained results are the same as for polynomial hardening function. For the smoothness effect, M_s and A_f are needed to decrease, while A_s and M_f should be increased in order to achieve better matching the applied experimental results [3, 52, 81].

Shape memory effect example

This example demonstrates a capability of the modified model to catch the shape memory effect. A starting temperature of the SMA specimen is fixed on 295 K which is between the austenitic A_s and martensitic M_s start temperature. The uniaxial tension stress of $\sigma = 600$ MPa is applied quasi-statically in 100 equal time steps until the maximal transformation strain is achieved. Then the cube is relaxed in another 100 steps to zero stress. In this case, it was assumed that the loading and unloading process are without influence of the thermo-mechanical coupling effect. After the relaxation, there are residual strains and the material is in the martensitic phase. Then, the temperature of the cube is increased in all nodes above the austenitic finish

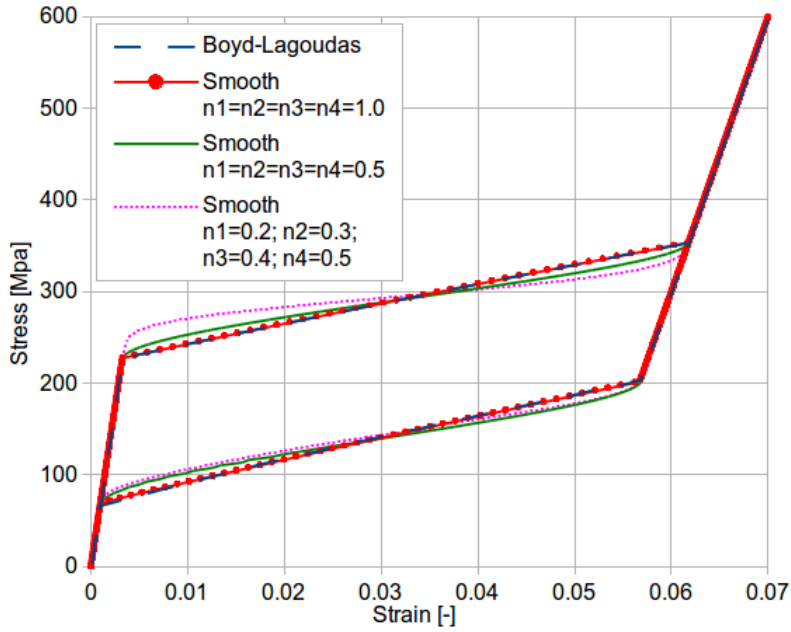


Figure 7.3: Comparison of smooth hardening function to the polynomial and cosine for SMA pseudoelasticity effect

temperature A_f to 350 K in 100 steps and the transformation strains are completely recovered as it is given in Figure 7.4. The obtained results (Figure 7.4(a)) have been compared to the literature data (Figure 7.4(b)). The excellent agreement has been achieved.

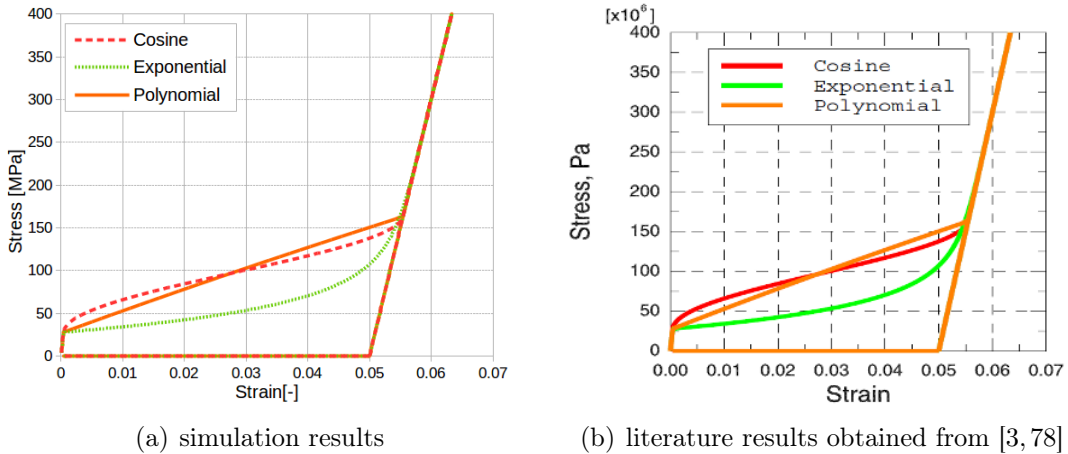


Figure 7.4: Stress-strain diagrams presenting SMA shape memory effect

Finally, the smooth hardening function (with hardening coefficients $n_1 = 0.2, n_2 = 0.3, n_3 = 0.4$ and $n_4 = 0.5$) have been compared to the polynomial and cosine [3] hardening law. The simulation results is presented in Figure 7.5.

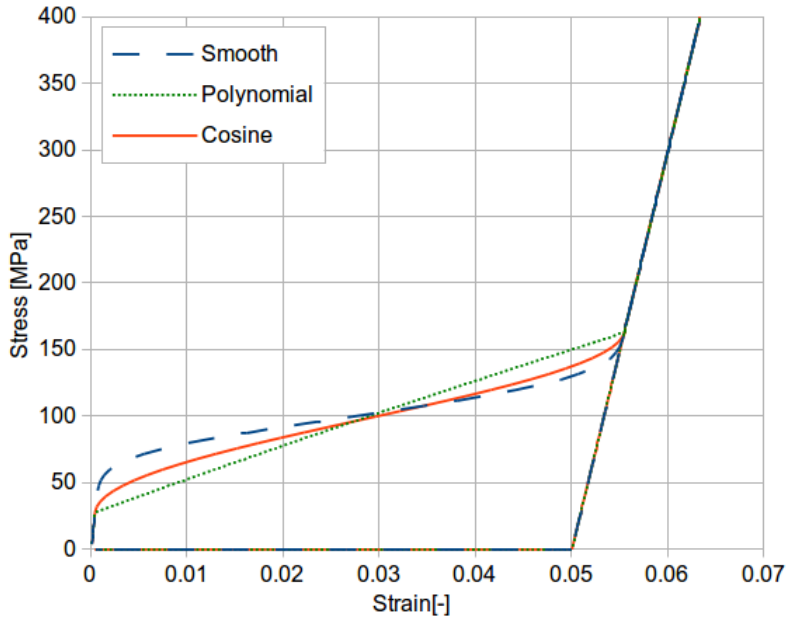


Figure 7.5: Comparison of smooth hardening function to the polynomial and cosine for SME

Phase transformation induced by temperature change

The SMA model with proposed modifications also need to have capability to simulate a temperature-induced phase transformation. To present that, this example has been prepared according to the literature [3, 78]. The initial temperature of the alloy is 350 K (above A_f). Small uniaxial stress 40 MPa (not sufficient to initiate phase transformation) is applied on one side of the cube while the opposite is fixed. The material temperature decreases below martensitic finish temperature M_f to 250 K and the phase transformation occurs. After heating to initial temperature, during the reverse phase transformation, all transformation strains are recovered. The strain-temperature dependence is presented in Figure 7.6. The simulation results (Figure 7.6(a)) have been also compared to the literature data (Figure 7.6(b)). The same strain-temperature dependences were noticed.

The smoothness hardening parameters have been also examined in this case and compared to the polynomial and cosine [3] hardening. The obtained results are presented in Figure 7.7.

7.1.2 Multiaxial loading

Two multiaxial loading examples are prepared to extend verification of the proposed modifications. The FEM model is the cube of dimension $2 \times 2 \times 2$. The loading conditions are proposed as axial and shear stress in proportional and non-proportional

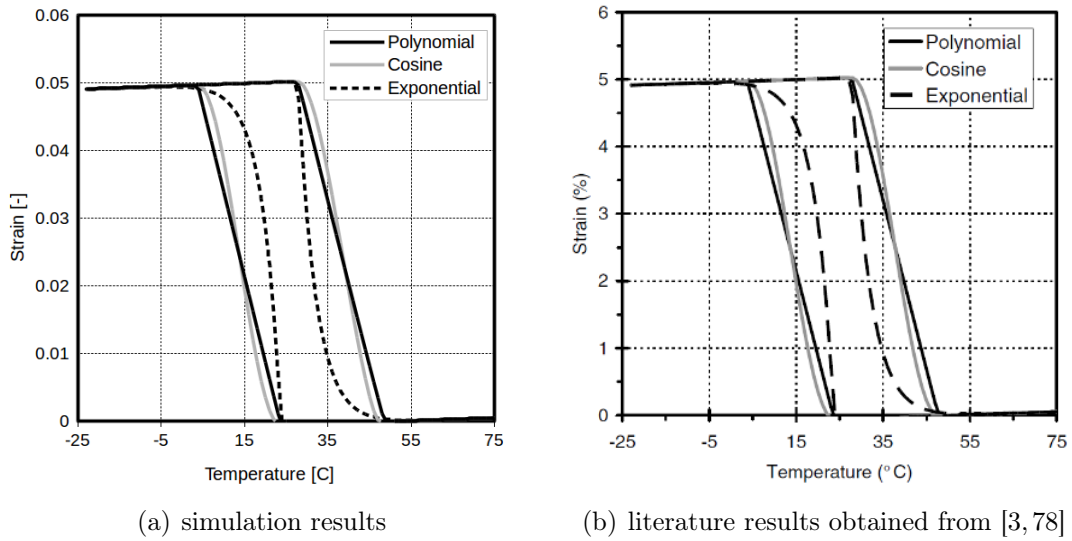


Figure 7.6: Temperature-induced martensite transformation in SMA

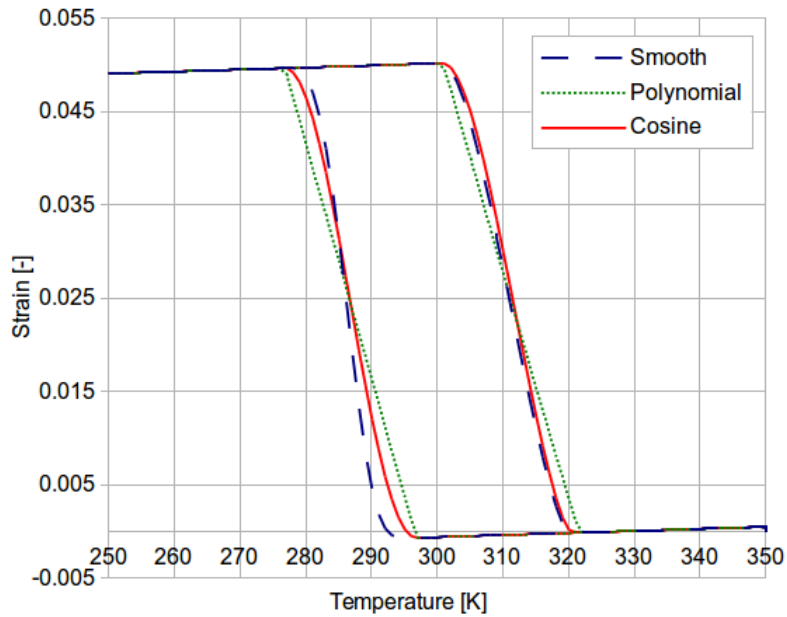


Figure 7.7: Comparison of smooth hardening function to the polynomial and cosine for the temperature-induced martensite transformation

manner. The material parameters used for those simulations are in accordance with literature [28] and are given in Table 7.2. As an interesting selection for hardening function, the smooth hardening law [3, 78, 81] has been used. The smoothness parameters has been set as $n_1 = n_2 = n_3 = n_4 = 0.3$.

Table 7.2: Material parameters of CuAlZnMn alloy used in multiaxial loading examples [28, 92]

E_A	E_M	α_A	α_M
30.000 MPa	10.000 MPa	$10.0 \cdot 10^{-6} K^{-1}$	$10.0 \cdot 10^{-6} K^{-1}$
M_{0s}	M_{0f}	A_{0s}	A_{0f}
269K	183K	188K	283K
H	ν	$\rho\Delta s_A$	$\rho\Delta s_M$
0.035	0.30	$-0.28 \text{ MPa } K^{-1}$	$-0.28 \text{ MPa } K^{-1}$

Proportional tension - shear loading example

The modified model is further examined by prediction of behavior under multiaxial loading in pseudoelasticity range. The SMA temperature has been set to be constant and equal to 308K during the analysis. As it was proposed in [92] the temperature is 25K higher than $A_f = 283\text{K}$. The loading path, given in Figure 7.8, is chosen according to [50] where tension is governing loading and shear is applied with a proportionality factor. The tension amplitude is 370 MPa, while the maximum shear stress is 80 MPa. Unloading is also conducted proportionally. The obtained stress - strain results are given in Figure 7.9.

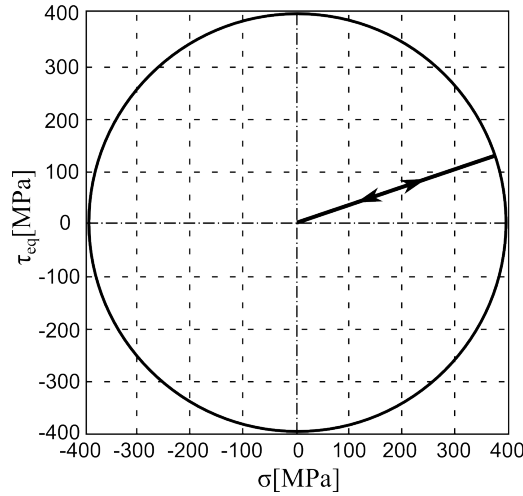


Figure 7.8: Stress path in proportional loading

As it can be noticed the both the tension and shear have pseudoelastic response (Figure 7.9). Both, loading and unloading are performed simultaneously (Figure 7.10), what presents the capability of the model to simulate behavior of the SMA under the proportional loading conditions.

Also, the influence of the time step increment on the accuracy for proportional loading example is analyzed. The analysis has been performed in 200 time steps and the results have been compared with the the results of simulation in 10 times bigger

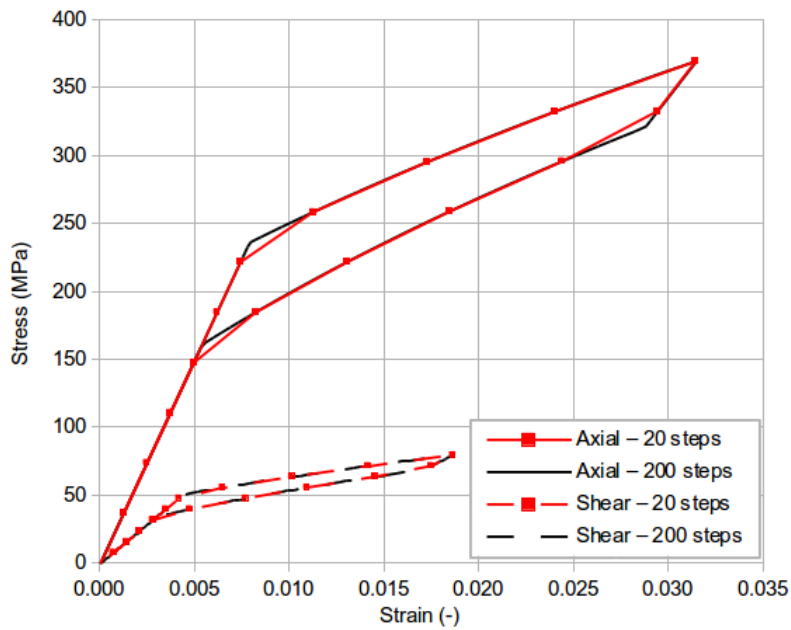


Figure 7.9: Tension and shear stress-strain diagrams for proportional loading

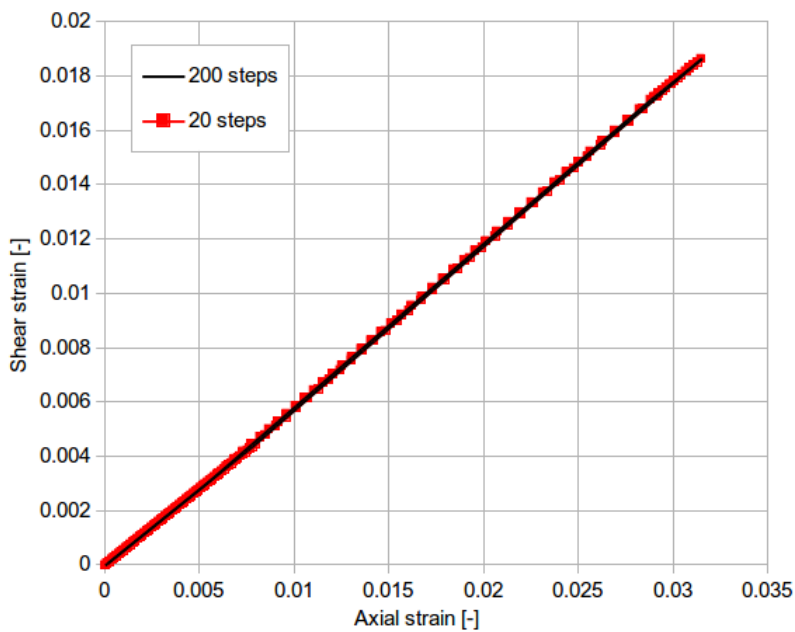


Figure 7.10: Axial-shear strain diagrams for proportional loading

step (20 time steps analysis). As it can be noticed in Figure 7.9, the stress-strain dependence is the same in the coincident steps, but the path can be different because it depends on the loading phase (phase transformation or elastic conditions).

Non-proportional tension-shear loading example

This example has been inspired by experimental results [92] and numerical simulations [28,50] from literature. The modified implementation of the constitutive model has been examined for capability to perform the simulation for non-proportional loading for pseudoelasticity effect. In this scope, the temperature of the SMA specimen is set to 308 K (25 K more than austenitic finish temperature $A_f = 283$ K). The experimental results of similar example were obtained from tension-torsion experiment of thin wall specimen [92] made of CuAlZnMn alloy and the obtained data are available in literature [28, 29, 92].

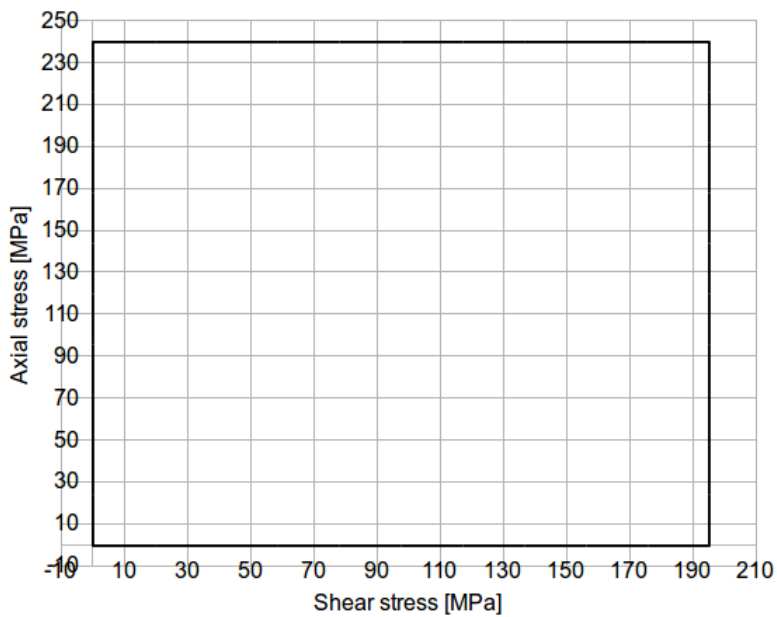


Figure 7.11: Axial stress vs. shear stress diagram presenting non-proportional loading

In simulation of the experiment, the axial stress of 240 MPa and then the shear stress of 200 MPa were applied combined at the same side of the cube ($2 \times 2 \times 2$) which consists of one 3D element, while the opposite side is constrained (Figure 7.11). Firstly axial stress was unloaded and than shear strains were recovered. The material parameters in this analysis are set in accordance to the literature [28]. For the axial and shear stress applied, the axial strain-shear strain dependence is presented in Figure 7.12. Furthermore, the relations between axial stress and strain and shear stress and strain are presented in Figures 7.13 and 7.14, respectively.

As it can be noticed, for the non-proportional loading, accuracy depends on step size because of constant direction of stress integration during the time step. In proportional loading, that difference does not exist because the direction is

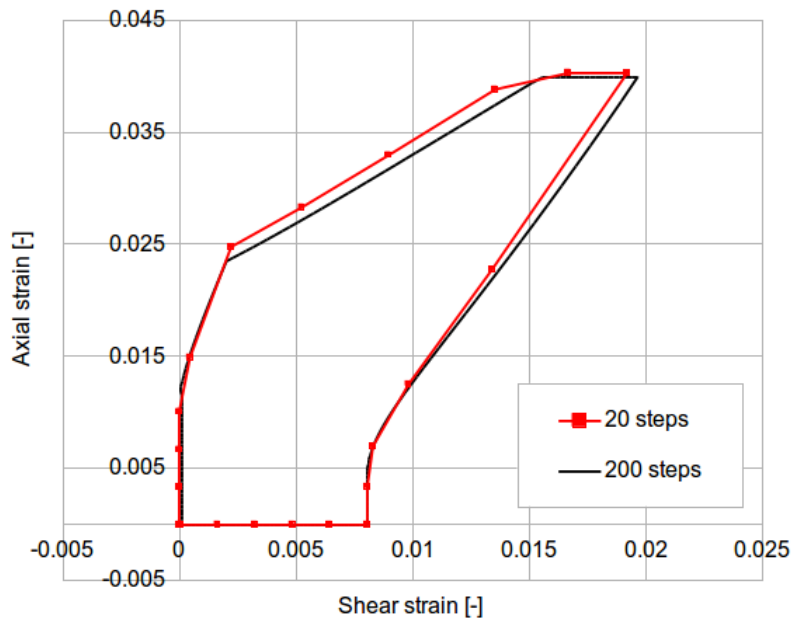


Figure 7.12: Axial strain vs. shear strain diagram presenting non-proportional loading

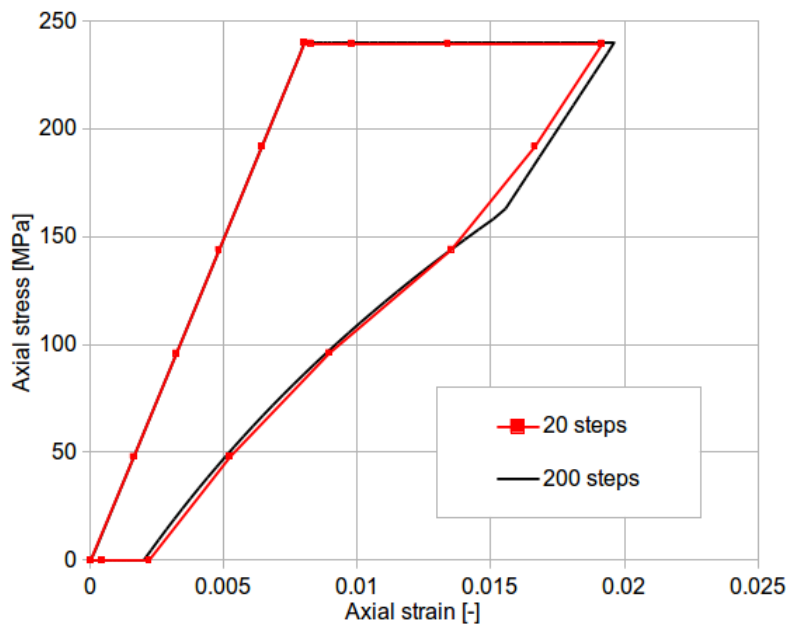


Figure 7.13: Axial stress vs. strain diagram presenting non-proportional loading

constant. Good agreement between the results for different time steps justifies the proposed assumptions about the stress integration in time step.

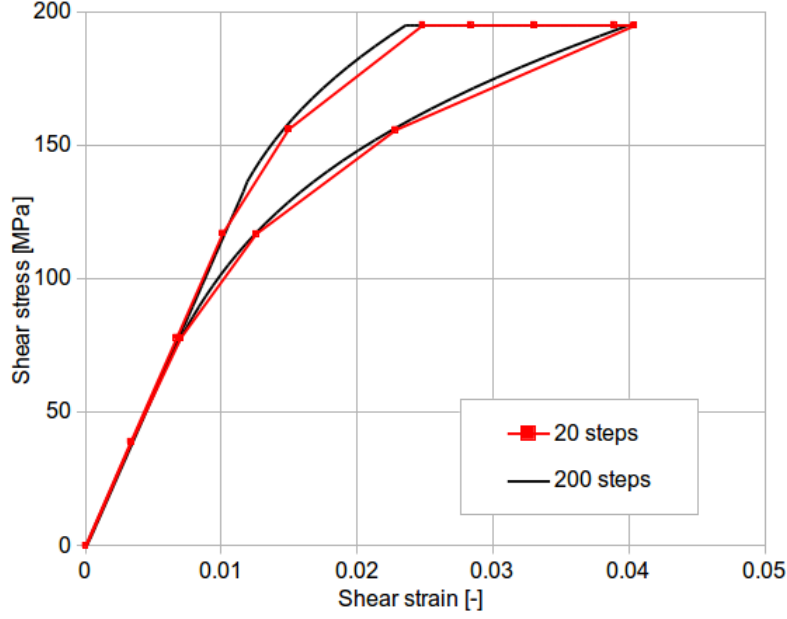


Figure 7.14: Shear stress vs. strain diagram for non-proportional loading

7.2 Large strain examples

7.2.1 Simple shear with superposed rigid rotation

In order to demonstrate the objectivity of constitutive equations and the frame-indifference of the stress integration, simple shear SMA loading example has been carried out with the superposed rigid rotation [84, 93].

The simple shear is defined by displacement described as function of rotation about \mathbf{e}_1 -axis as following:

$$\mathbf{x} = \mathbf{R} [\mathbf{X} + (\dot{x}t) X_3 \mathbf{e}_2], \quad (7.1)$$

where the rotation tensor \mathbf{R} is defined as:

$$\mathbf{R} = (\mathbf{e}_2 \otimes \mathbf{e}_2 + \mathbf{e}_3 \otimes \mathbf{e}_3) \cos(\omega t) + (\mathbf{e}_2 \otimes \mathbf{e}_3 - \mathbf{e}_3 \otimes \mathbf{e}_2) \sin(\omega t) + \mathbf{e}_1 \otimes \mathbf{e}_1. \quad (7.2)$$

The material parameters used for the numerical calculation are the same as given in Table 7.1. The angular velocity of the rotation is $\omega = 0.02\pi$ radians per second for $t \in [0, 100]$, so that $\theta = \omega t \in [0, 2\pi]$. The velocity of the deformation is positive in the first half of rotation $\dot{x} = 0.0025$ per second for $t \in [0, 50]$ so that $\dot{x}t \in [0, 0.125]$. While, the velocity of the deformation in the second half of the rotation process is negative $\dot{x} = -0.0025$ per second for $t \in [50, 100]$ so that $\dot{x}t \in [0.125, 0]$. The time

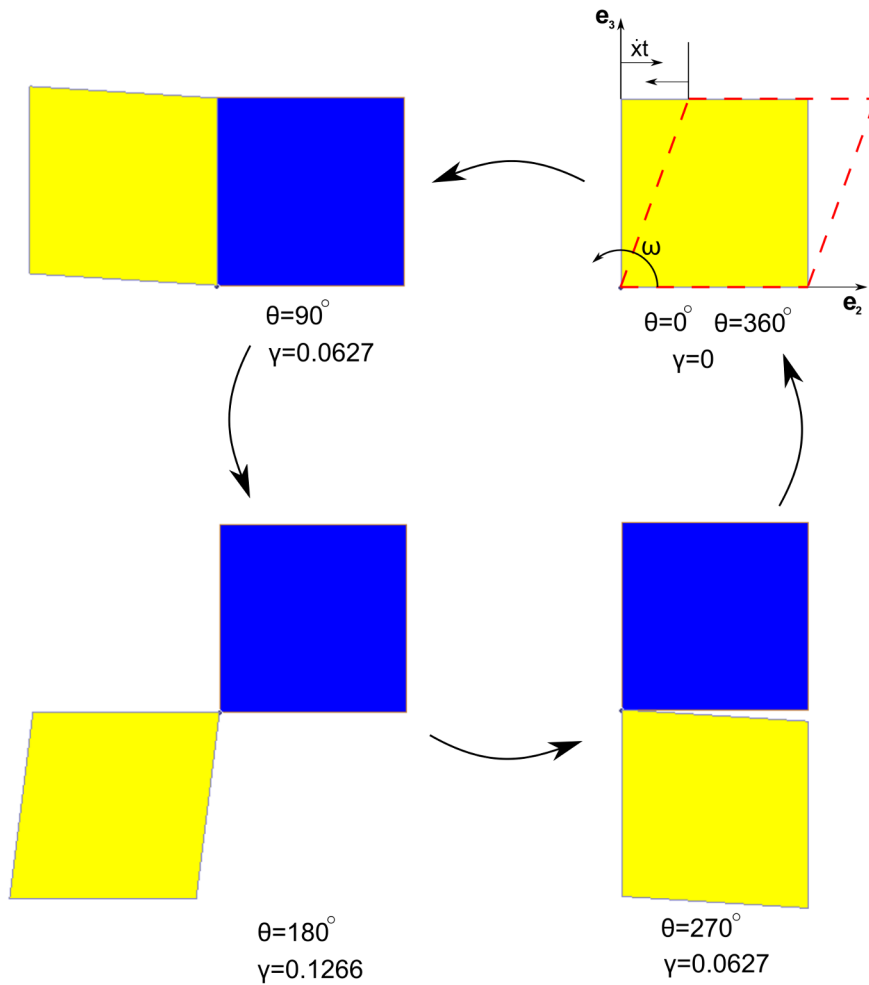


Figure 7.15: Representative positions of simple shear loading example with superposed rigid rotation

step of $\Delta t = 1s$ is fixed and corresponds to a shear strain increment of $\Delta\gamma = 0.0025$ and a rotation increment is $\Delta\theta = 3.6^\circ$. The results of the shear component of the "unrotated" Kirchhoff stress versus amount of shear γ obtained from the numerical calculation is shown in Figure 7.16.

The two obtained curves overlap each other what demonstrates good agreement between the two calculation approaches. The view on the initial and deformed geometry at a several representative positions of the simple shear plus superposed rotation are shown in Figure 7.15.

7.2.2 Cantilever beam with moment at free end

The large deflection of beams can be find in many industrial applications such as aerospace engineering, structural designs, suspension bridges, and various kinds of

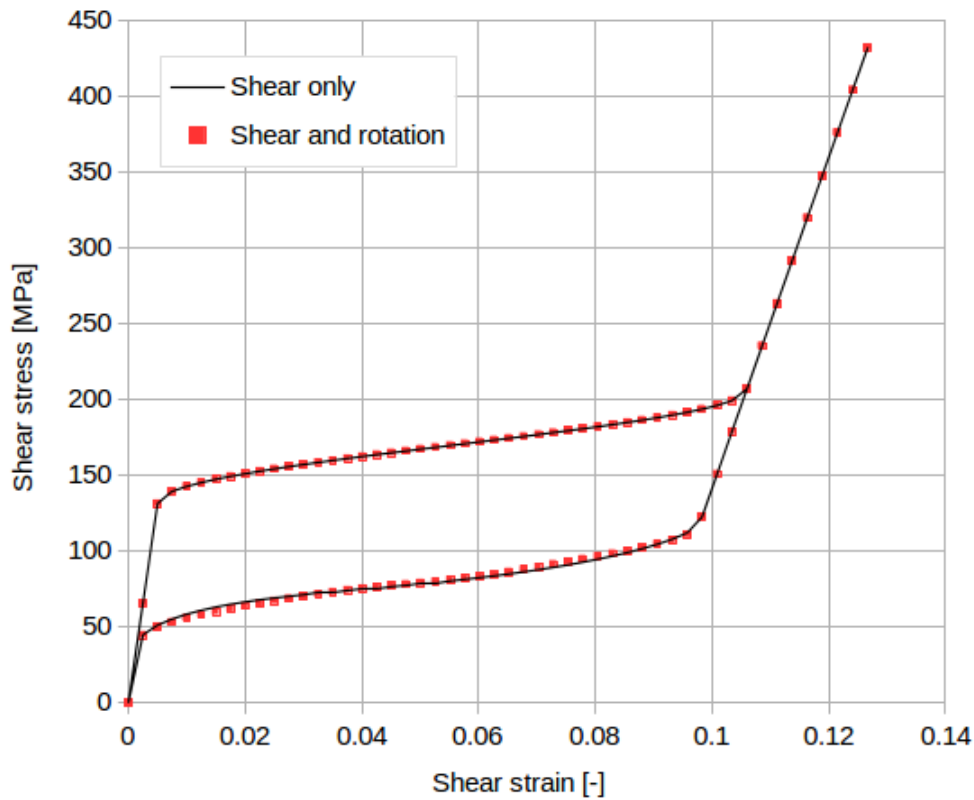


Figure 7.16: Comparison of results obtained for SMA shear with superposed rotation against shear with no superposed rotation

manufacturing processes. So as popular problem, a rectangular cross-section cantilever beam loaded with a moment at free end is considered in this work (Figure 7.17).

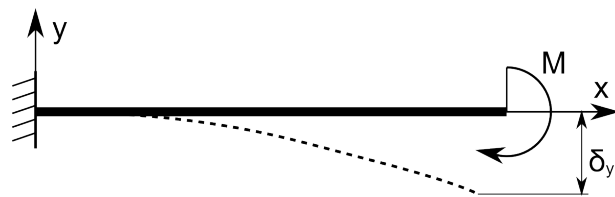


Figure 7.17: Scheme of cantilever beam subjected to end moment

The beam is made of SMA with the same material parameters as given in Table 7.1. The dimensions of the model are $100 \text{ mm} \times 40 \text{ mm} \times 10 \text{ mm}$. The FEM mesh is divided into 320 ($20 \times 16 \times 1$) 3D elements. The model is loaded at the free end by the moment given as pressure in the direction of the cantilever length. The pressure is positive at upper half of the cross section and negative on the lower part distributed as uniformly varying load (linear function) over the vertical coordinate.

In Figures 7.19(a), 7.19(c) and 7.19(e) it can be noticed that during the loading the axial stress in direction of the cantilever length is changing in expected fashion

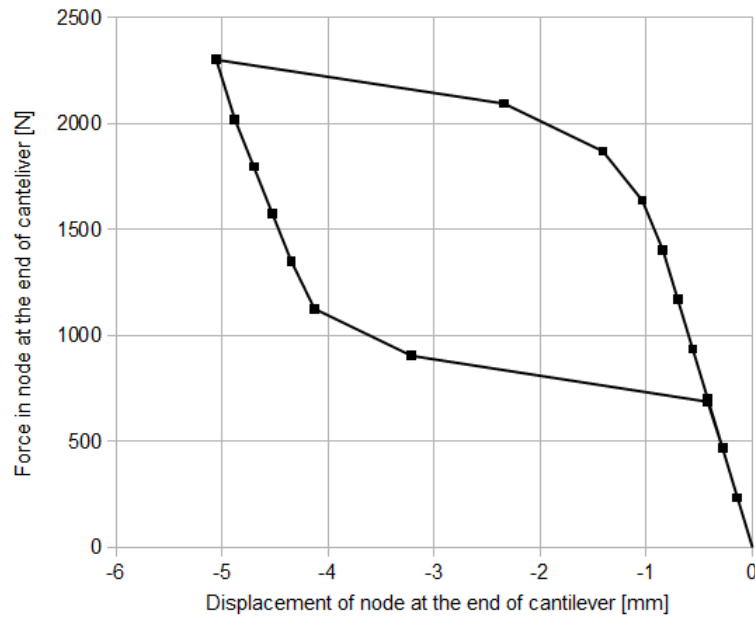


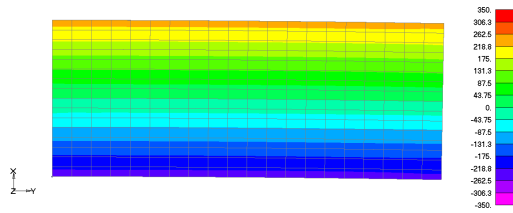
Figure 7.18: Force – displacement dependence at the loaded SMA cantilever end

(symmetric with respect to the neutral line). The stress has highest value in the outermost points looking from the neutral (middle) line where the axial stress is zero. When the martensitic phase transformation begins in 8th step (Figure 7.19(d)) a cumulation of the martensitic volume fraction can be noticed at the free end of the cantilever. The reason for this is a deflection of the cantilever what influences asymmetry of the problem. The concentration of the martensite is the highest in 10th step (Figure 7.19(f)), while it becomes lower when the unloading begins (Figures 7.20(b), 7.20(d) and 7.20(f)) and it disappears when we come back to the elastic zone.

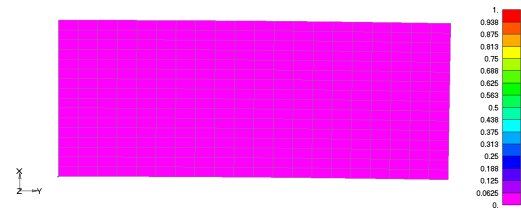
7.2.3 Stent unit cell

For the numerical analysis of complex SMA structures exhibited large strains, finite deformation constitutive model is necessary for correct simulation. To show capability of the implemented constitutive model, a behavior of stent unit cell is modeled with initial geometry given in Figure 7.21 [49, 94]. Due to the symmetry, the FEM model of one-quarter of the stent unit cell is given in Figure 7.22. Material parameters used in this analysis are given in Table 7.3.

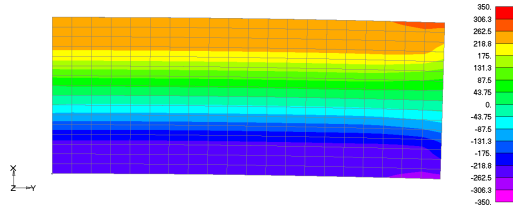
The prescribed boundary conditions for the stent unit cell are: the nodes on the bottom face are describing a Y-symmetry, on the left face are describing X-symmetry, while on the top face a displacement profile is prescribed along direction-Y for all the nodes. All the nodes have the same initial temperature of 298 K. The FEM sim-



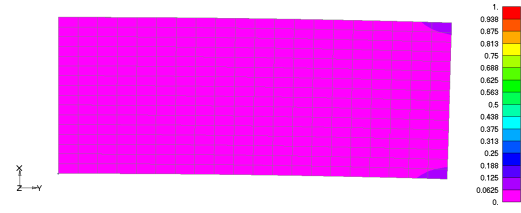
(a) Stress distribution along the cantilever length in the 6th step



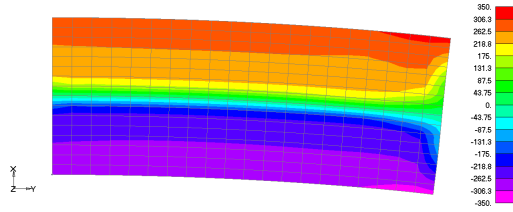
(b) Martensitic volume fraction in the 6th step



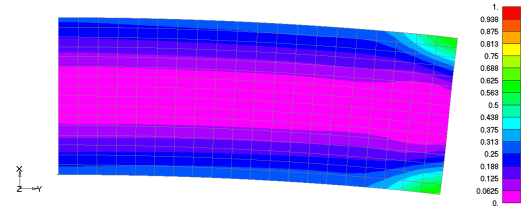
(c) Stress distribution along the cantilever length in the 8th step



(d) Martensitic volume fraction in the 8th step



(e) Stress distribution along the cantilever length in the 10th step



(f) Martensitic volume fraction in the 10th step

Figure 7.19: Stress distribution along the cantilever length and martensitic volume fraction in chosen steps during the loading

ulation was conducted with and without influence of thermo-mechanical coupling on material behavior. In Figure 7.23, the force vs. displacement dependency obtained from the loading–unloading cycle with thermo-mechanical coupling and with constant temperature prescribed in nodes is presented. The force is obtained as constrained forces along the Y-direction for all the nodes at the top face. From the curve presented in Figure 7.23, one can notice pseudoelastic uniaxial response (flag-like). Also, it can be observed that thermo-mechanical coupling strongly influences force-displacement diagram, what was also noticed during the model verification in uniaxial tension tests [16]. Presented dependency show that during the exploitation of SMA structures, significant temperature change is possible what is very important for cyclic loading and high loading rate deformation.

From the curve given in Figure 7.23, it can be noticed that the uniaxial (flag-like) pseudoelastic response exhibited. Also, the martensitic volume fraction throughout the stent unit cell is determined at any point of the loading process. In Fig-

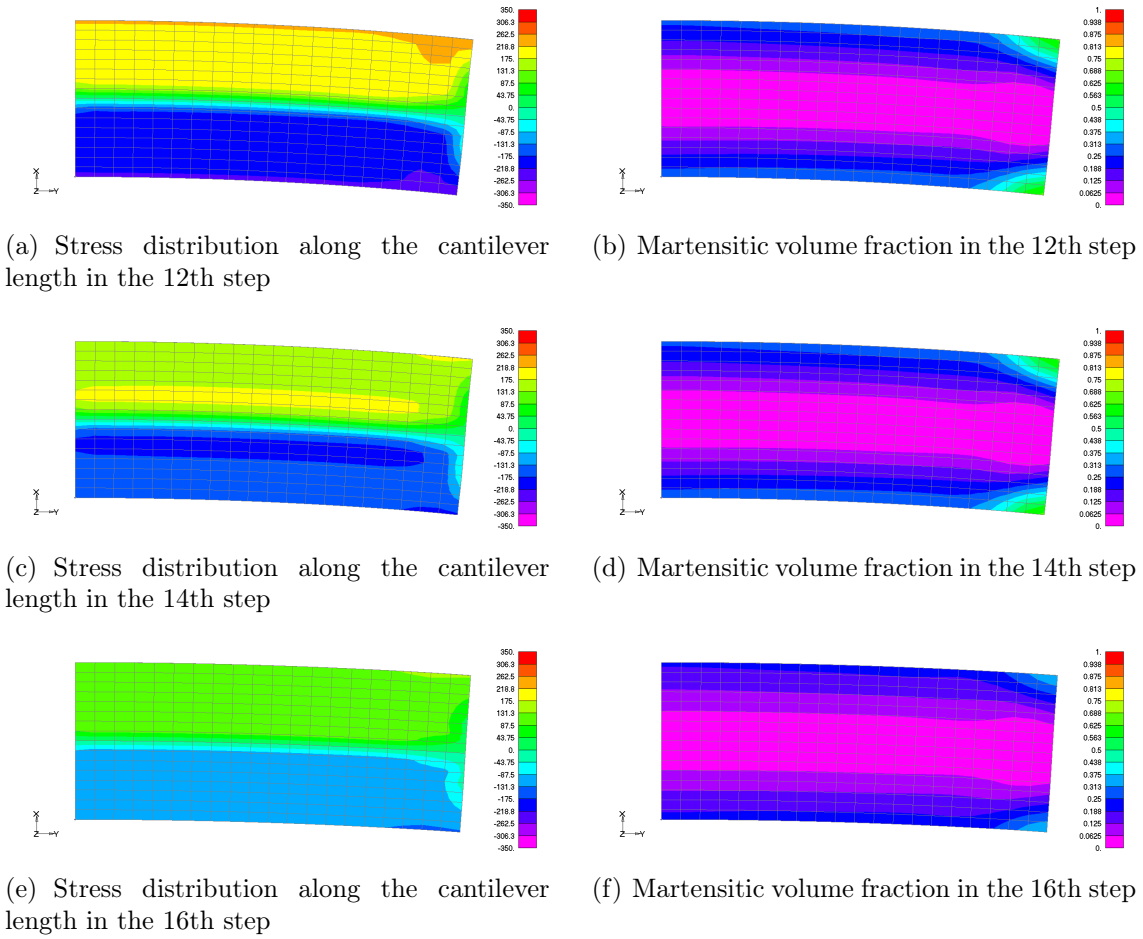


Figure 7.20: Stress distribution along the cantilever length and martensitic volume fraction in chosen steps during the unloading

ure 7.24 are given contours of the martensitic volume fraction at the initial state (Figure 7.24(a)) and at the maximum loading i.e. the highest concentration of martensite volume fraction (Figure 7.24(b)).

Also, martensitic volume fraction in stent unit cell is determined in each point of loading process. In Figure 7.24, martensitic volume fraction in initial state (Figure 7.24(a)) and at the maximal loading i.e. the highest concentration of martensitic volume fraction (Figure 7.24(b)) are given. Change of stent temperature in adiabatic conditions, is presented in Figures 7.25 to 7.27. The initial temperature is given in Figure 7.25. After the loading by displacement rate $v = 2.82mm/s$ in 20 time steps to the maximal displacement of $2.82mm$, phase transformation energy transformed into the heat imposed the temperature change presented in Figure 7.26. In the next 20 steps, the same displacement rate was used during the unloading, what imposed the reverse phase transformation and temperature change given in Figure 7.27. As it can be noticed, forward phase transformation release the heat

Table 7.3: Material parameters of SMA for stent unit cell

Parameter	Value
Austenitic Young modulus	$E_A = 6.20 \cdot 10^5 \text{ MPa}$
Martensitic Young modulus	$E_M = 3.10 \cdot 10^5 \text{ MPa}$
Poisson's ratio	$\nu = 0.33$
Maximal transformation strain	$H = 0.047$
Density	$\rho = 6290 \frac{\text{kg}}{\text{m}^3}$
Austenitic coefficient of thermal expansion	$\alpha = 1.0 \cdot 10^{-5}$
Martensitic coefficient of thermal expansion	$\alpha = 1.0 \cdot 10^{-5}$
Conductivity	$k = 18 \frac{\text{W}}{\text{m}^2 \text{K}}$
Convectivity	$\lambda_c = 6.5 \frac{\text{W}}{\text{m}^2 \text{K}}$
Capacity	$c = 0.46 \cdot 10^{-9} \frac{\text{MJ}}{\text{kgK}}$
Austenitic stress influence coefficient	$\rho \Delta s_A = -0.364 \frac{\text{MPa}}{\text{K}}$
Martensitic stress influence coefficient	$\rho \Delta s_M = -0.364 \frac{\text{MPa}}{\text{K}}$
Martensitic start temperature	$M_{0s} = 251.3 \text{ K}$
Martensitic finish temperature	$M_{0f} = 213 \text{ K}$
Austenitic start temperature	$A_{0s} = 260.3 \text{ K}$
Austenitic finish temperature	$A_{0f} = 268.5 \text{ K}$

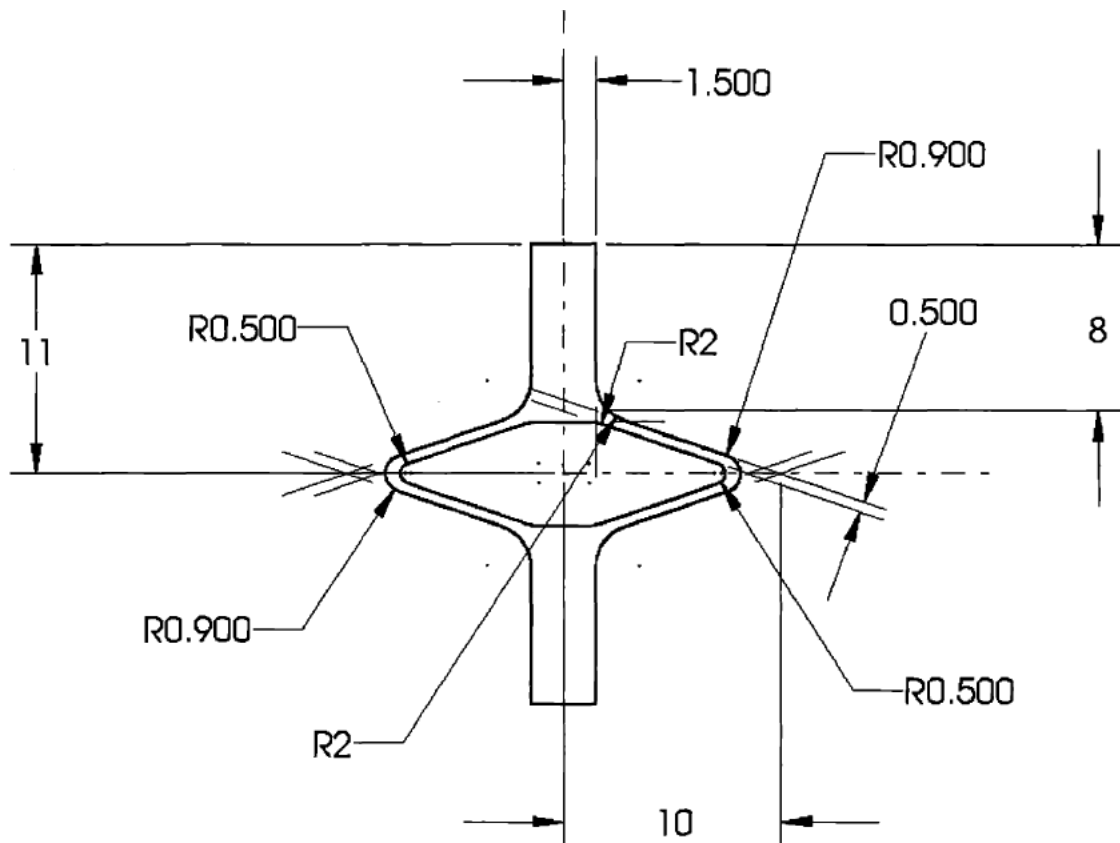


Figure 7.21: Specimen geometry for a stent unit cell of thickness 0.53 mm [49, 94]

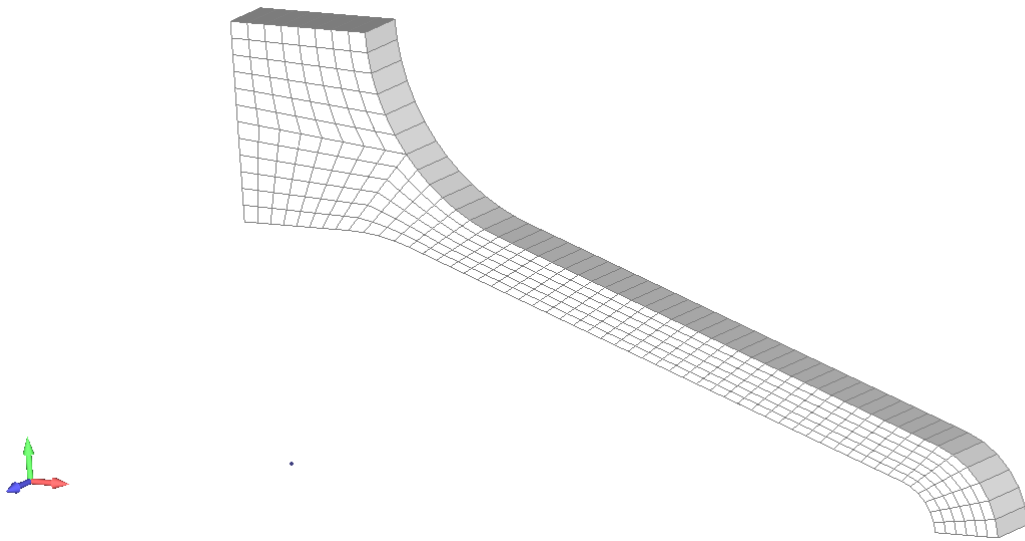


Figure 7.22: Undeformed mesh of one-quarter of the tested stent unit cell

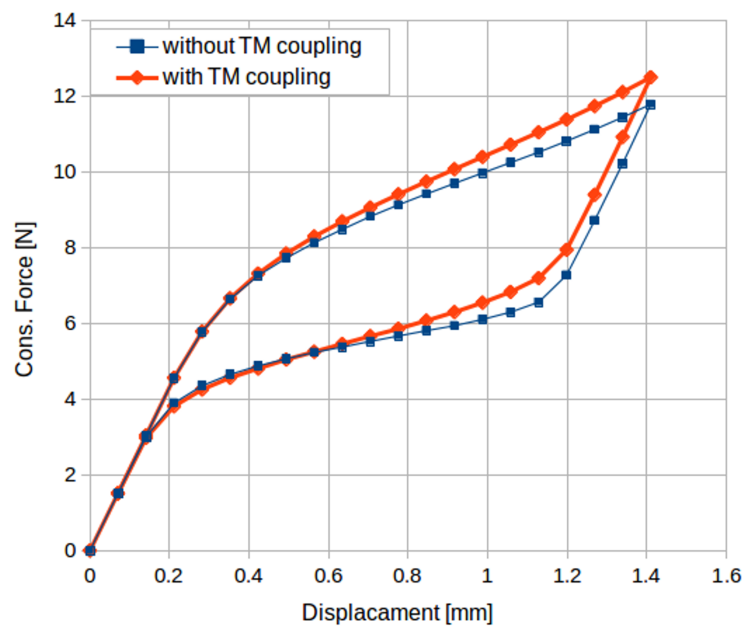
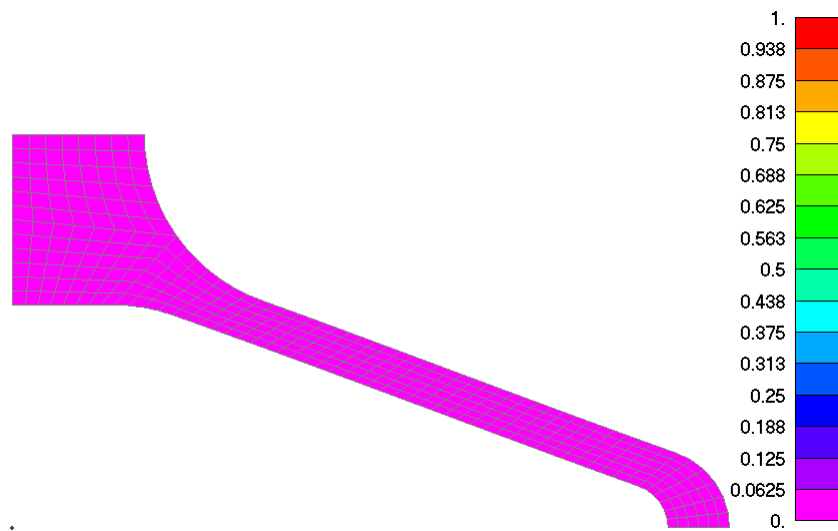


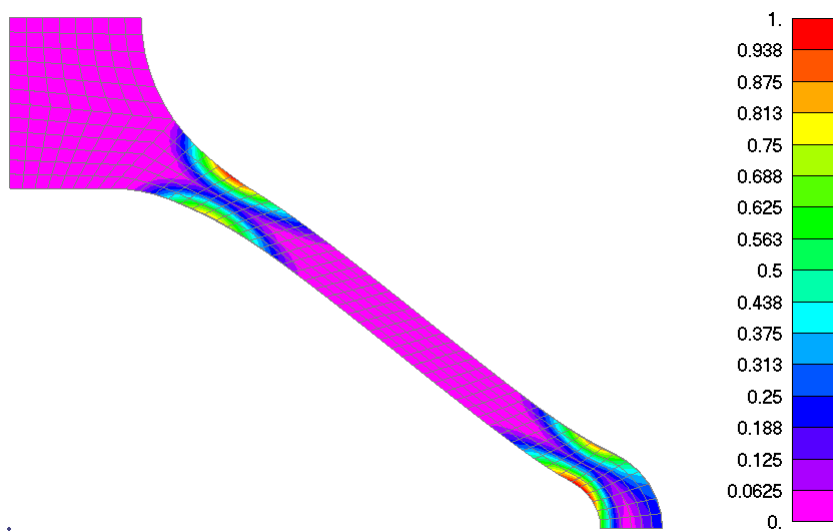
Figure 7.23: Одзив сила-померање добијена FEM анализом јединичне ћелије стента под псеудоеластичним условом

and material temperature increases, while the reverse phase transformation, absorbs the heat and some parts of the stent are cooled below the initial temperature.

This phenomenon has been already observed for the various strain rates in experimental and numerical investigation of SMA samples. It was noticed that the specimen temperature after unloading, for the small strain rates, drops under the initial temperature. This verifies functionality of thermo-mechanical implementation of SMA constitutive model for the large strain problems.



(a) the initial state and upon full reversal of the deformation to the initial position



(b) the state at the maximum loading conditions

Figure 7.24: Contours of martensite volume fraction within the stent unit cell without thermo-mechanical coupling

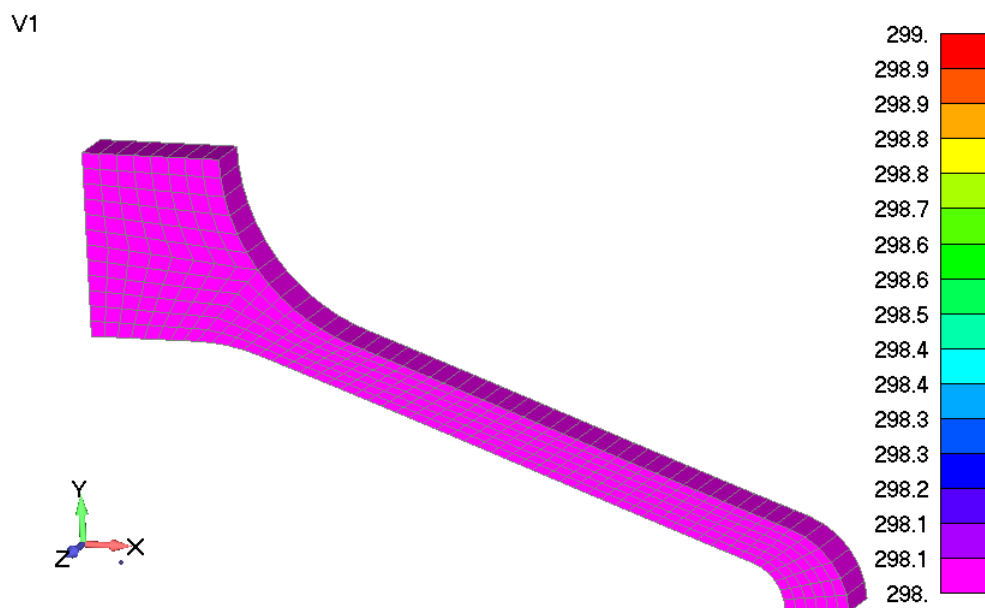


Figure 7.25: Temperature field of stent unit cell at initial state

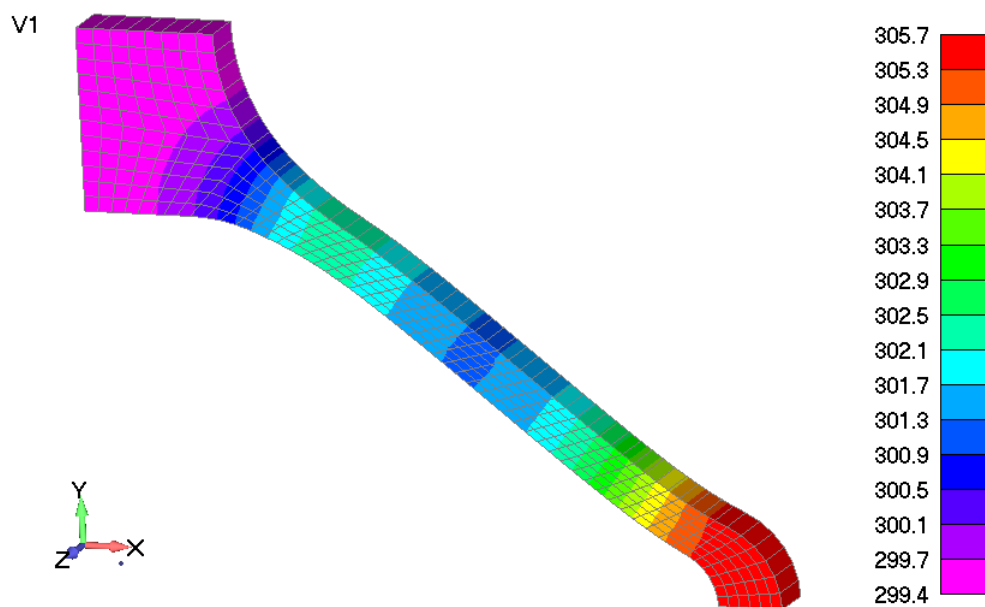


Figure 7.26: Temperature field of stent unit cell at maximal loading

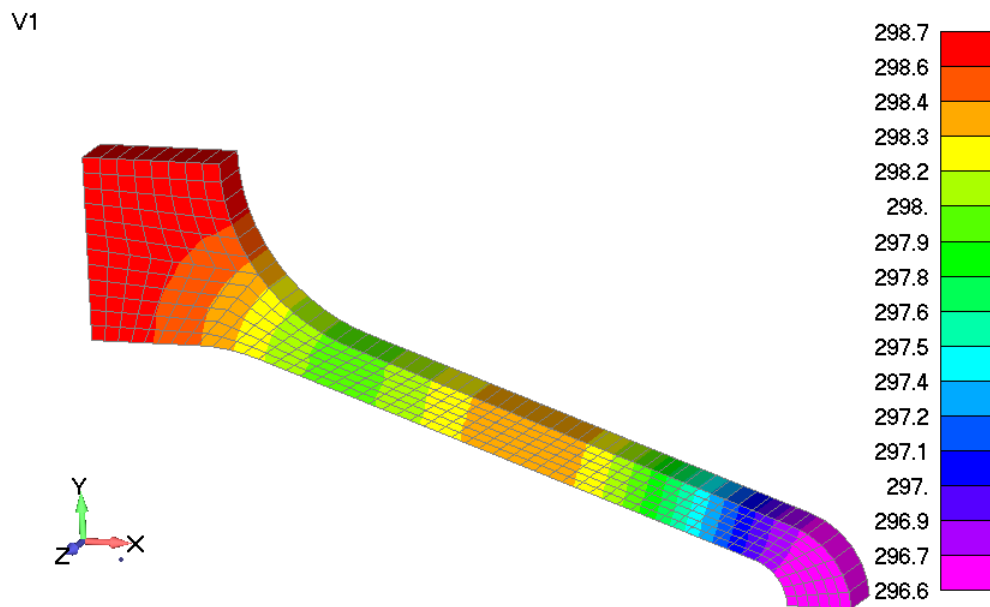


Figure 7.27: Temperature field of stent unit cell at unloaded state

Chapter 8

Conclusions

Fascinating properties of SMA and phenomenon exhibits during its behavior, provide wide application of SMA in reliable constructions. Demands appointed by the researchers and engineers around the world, motivated the author to start an investigation of the SMA behavior. The idea to efficiently and accurately simulate SMA behavior is very useful for many scientific problems and industrial solutions where SMA finds application. There are many mathematical models and several approaches which describe phenomenological behavior of SMA, so, it is difficult to choose the proper solution. So, the simplification and improvements are obligatory if we want to make the implementation more efficient and accurate. Decomposition of the deformation gradient to deviatoric and volumetric part and using the effective variables, provided possibility of further extension of the constitutive model.

One of the important properties is high thermal sensitivity of SMA, noticed during the experimental investigation. This causes problems during the exploitation and production, but also this motivates analysis of temperature change influence. Beside the external factors which causes the temperature change of SMA, the dissipative energy of martensitic phase transformation and its influence on the SMA behavior are of great importance for the correct simulation of the material behavior. As the most appropriate solution, the partitioned approach for the coupling of structural analysis and heat transfer components is chosen as the most powerful solution for thermo-mechanical problems.

The simulation of the complex stress states and 3D FEM models for large strains up to 10% for SMA, makes the need for extension of the constitutive model to the large strain theory problems. Using the multiplicative decomposition, the well known techniques of constitutive models extension for large strain problems and the improvements of the constitutive model, give a popular software solution powerful

to solve thermo-mechanical SMA problems for complex stress states.

For the successful realization of the objectives several tasks were necessary to be solved:

1.
 - The theory presented by Lagoudas in his book [3], was inspiration and the base for the thinking about the mathematical description of the SMA behavior. Details given in the book and published papers, motivated the author to extend the research in the framework of the phenomenological SMA models.
 - After the starting application of the given theory, necessary simplifications were adopted in order to use the method proposed by Kojić and Bathe [64] for the efficient integration of the constitutive equations.
 - It was necessary to modify the critical thermodynamic force to match new integration method. The total stress is decomposed into deviatoric and mean part and the stress integration is done in direction of the trial deviatoric stress or the trial transformation strain. That simplified the constitutive model to solution of only one scalar non-linear equation in iterative procedure. Already given examples given by Lagoudas in [78] are investigated as benchmark tests for the correctness and functionality of the implemented constitutive model. Three uni-axially loaded examples [78] are analyzed to verify described modifications and the same results were obtained.
2.
 - Furthermore, the results of wide program of the experimental tests performed at the IPPT, PAN and AIT in Japan, available in published papers, verified strong thermo-mechanical coupling during the pseudoelastic loading and unloading. The experiments were performed under the various stress and strain rates, what was necessary request for the correct numerical analysis. The experiments have been carefully conducted and the important data were measured, systemized and compared to show influence of the various loading rates on the material behaviour. The obtained results show great sensitivity of the SMA stress-strain curves to the loading rates and their related temperature changes due to the strong thermomechanical coupling.
 - Thermal sensitivity and the specific behavior of the SMA under the various loading rate are new demands which need to be achieved for the accurate and correct numerical simulation.

- Those observations imposed further extension of the SMA constitutive equations. The necessary capability of the SMA constitutive model to simulate thermo-mechanical coupled problems expanded the field of interest to thermal properties of phase transformation. Separate FEM software components for the structural and the heat transfer analysis were available. The partitioned coupling approach was established as considerable solution due to possibility to model complex stress and thermal states and to take into account mutual influence.
 - Further, such coupling approach provides re-use of existing FEM software in order to accurately predict the SMA behavior. To show the advantages of the coupled analysis, the experiments have been modeled realistically with included boundary and loading condition for both structural and heat transfer analysis.
 - The obtained results have been compared with the experimental one for all stress and strain rates. The comparison of the experimental and numerical results indicates good qualitative and quantitative agreement, since the model confirms stress as well as temperature variations.
 - Both the experimental and numerical data significantly depend on the applied loading rate.
 - The numerical model also confirms the saturation stage of the exothermic martensitic forward transformation, as well as the temperature decrease during the reverse transformation and even its decline below the initial SMA specimen temperature after the unloading. The temperature change caused by the exothermic phase transformation, has a significant influence on the SMA behavior.
- 3.
- As an answer on the request to model the complex SMA structures, the multiplicative decomposition of total deformation gradient is assumed.
 - The trial elastic deviatoric strain can be calculated by using the Green-Lagrange or logarithmic strain tensor and the further integration procedure is the same as in the case of small strains.
 - That provides possibility to use same iterative procedure for computing of large strain problems. As the benchmark verification examples several multiaxial loading examples have been prepared.
 - To extend the application of the introduced implementation, the cantilever beam loaded by the moment at the free end is modeled. The

presented results show that the contours for the stress and the martensitic volume fraction are obtained as expected. At the end, the stent unit cell is modeled to show applicability of the implementation. The obtained results are compared with the literature results and the satisfying matching of the results have been achieved.

Further research

During the research presented in this thesis, several possible directions of further investigation have been recognized.

Experimental research of the cyclic loading of SMA specimens has become the challenging because of the change of material characteristic. The numerical simulation of such problems is one of the task which should present the applicability of the given implementation and to define necessary improvements. Also, one of the possible problems observed during the experimental investigation is accumulation of martensitic volume fraction during the cyclic loading.

A special case of the subloop cyclic loading is necessary to be examined as real demand in SMA exploitation. In this scope, also there are question about the fatigue investigation of SMA.

In this thesis, benchmark examples have been presented as well as selected examples from literature which present functionality of the given approach. Further FEM modeling of real structures and simulation of the possible complex stress states is challenge and commitment in the further research of such materials. Details which should be investigated with special care are possibility of plastic deformation along the transformation strains due to higher stress states and maximal transformation strain dependency on stress. Also, different tension-compression behavior (asymmetry) of SMA is interesting phenomenon which need to be described.

Also, various multiphysical problems which require interaction of several physical fields can be interesting i.e. during the stent implementation into the human body there are interaction between the stent and the blood vessel what is dangerous operation. After the implementation, the stent is in the specific environment in permanent contact with fluid flow, so a simulation of such behavior using the fluid-structure interaction could help to prevent undesired consequences. Also, due to the good electro-conductivity, SMA effects can be used by Joule heating effect in electric cables.

A special group of SMA with the magnetic properties have been recognized as useful and applicable. So, it is necessary to extend the coupling to thermo-magneto-

mechanical level and provide possibility to solve such multiphysics problems. A separate component capable to solve magnetic field problems is necessary to be developed and coupled with the already used components. Also, according to already published papers of experimental investigation of such materials [18], it is necessary to analyse physical demands of the coupling.

Bibliography

- [1] K. Otsuka and C. Wayman, eds., *Shape memory materials*. Cambridge University Press, Cambridge, 1998.
- [2] T. Duering, K. Melton, D. Stockel, and C. Wayman, *Engineering Aspects of Shape Memory Alloys*. Butterworth-Heinemann, London, 1990.
- [3] D. Lagoudas, *Shape Memory Alloys: Modeling and Engineering Applications*. Springer, 2010.
- [4] C. Grabe, *Experimental testing and parameter identification on the multidimensional material behavior of shape memory alloys*. PhD thesis, Institut für Mechanik, Ruhr-Universität Bochum, Germany, Jun 2007.
- [5] M. Jovanović, V. Lazić, D. Adamović, and N. Ratković, *Mašinski materijali*. Univerzitet u Kragujevcu, Mašinski fakultet u Kragujevcu, 2003.
- [6] W. Buehler, J. Gilfrich, and R. Wiley, “Effect of low-temperature phase changes on the mechanical properties of alloys near composition TiNi,” *Journal of Applied Physics*, vol. 34, no. 5, pp. 1475–1477, 1963.
- [7] S. Barbarino, E. Saavedra Flores, R. Ajaj, I. Dayyani, and M. Friswell, “A review on shape memory alloys with applications to morphing aircraft,” *Smart Materials and Structures*, vol. 23, no. 6, p. 063001, 2014.
- [8] E. Pieczyska, H. Tobushi, and K. Kulasinski, “Development of transformation bands in TiNi SMA for various stress and strain rates studied by a fast and sensitive infrared camera,” *Smart Materials and Structures*, vol. 22, no. 3, p. 035007, 2013.
- [9] M. Panico and L. Brinson, “A three-dimensional phenomenological model for martensite reorientation in shape memory alloys,” *Journal of the Mechanics and Physics of Solids*, vol. 55, no. 11, pp. 2491 – 2511, 2007.

- [10] J. Shaw and S. Kyriakides, “Thermomechanical aspects of NiTi,” *J. Mech. Phys. Solids*, vol. 43, no. 8, pp. 1243 – 1281, 1995.
- [11] J. Hallai and S. Kyriakides, “Underlying material response for Lüders-like instabilities,” *International Journal of Plasticity*, vol. 47, no. 0, pp. 1 – 12, 2013.
- [12] E. Pieczyska, S. Gadaj, W. Nowacki, and H. Tobushi, “Phase–transformation fronts evolution for stress– and strain–controlled tension tests in TiNi shape memory alloy,” *Experimental Mechanics*, vol. 46, no. 4, pp. 531–542, 2006.
- [13] E. Pieczyska, *Analiza doświadczalna właściwości termomechanicznych stopów TiNi oraz poliuretanu z pamięci kształtu (Experimental Analysis of Thermomechanical Properties of TiNi Shape Memory Alloys and Shape Memory Polyurethane)*. Prace IPPT-IFTR Reports, Institute of Fundamental Technological Research of the Polish Academy of Sciences, 2008. in Polish, graphs in English, Habilitation thesis.
- [14] E. Pieczyska, “Experimental investigation of stress–induced martensite transformation activity in shape memory alloy,” report grant No NN501 2208 37, Institute of Fundamental Technological Research of the Polish Academy of Sciences, 2012.
- [15] E. Pieczyska, M. Staszczak, V. Dunić, R. Slavković, H. Tobushi, and K. Takeda, “Development of Stress-Induced Martensitic Transformation in TiNi Shape Memory Alloy,” *Journal of Materials Engineering and Performance*, vol. 23, no. 7, pp. 2505–2514, 2014.
- [16] V. Dunić, E. Pieczyska, H. Tobushi, M. Staszczak, and R. Slavković, “Experimental and numerical thermo-mechanical analysis of shape memory alloy subjected to tension with various stress and strain rates,” *Smart Materials and Structures*, vol. 23, no. 5, p. 055026, 2014.
- [17] H. Tobushi, R. Matsui, K. Takeda, and E. Pieczyska, *Mechanical Properties of Shape Memory Materials*. Materials Science and Technologies, Mechanical Engineering Theory and Applications, NOVA Publishers, 2013.
- [18] E. Pieczyska, “Mechanical behavior and infrared imaging of ferromagnetic NiFe–GaCo SMA single crystal subjected to subsequent compression cycles,” *Meccanica*, vol. 50, no. 2, pp. 585–590, 2015.

- [19] F. Auricchio, E. Boatti, and M. Conti, “Chapter 11 - SMA Biomedical Applications,” in *Shape Memory Alloy Engineering* (L. L. Concilio, ed.), pp. 307 – 341, Boston: Butterworth-Heinemann, 2015.
- [20] J. Arghavani, *Thermo-mechanical behavior of shape memory alloys under multi-axial loadings: constitutive modeling and numerical implementation at small and finite strains*. PhD thesis, Sharif University of Technology, Tehran, Iran, September 2010.
- [21] F. Auricchio, E. Boatti, and M. Conti, “Chapter 12 - SMA Cardiovascular Applications and Computer-Based Design,” in *Shape Memory Alloy Engineering* (L. L. Concilio, ed.), pp. 343 – 367, Boston: Butterworth-Heinemann, 2015.
- [22] D. Christ and S. Reese, “A finite element model for shape memory alloys considering thermomechanical couplings at large strains,” *International Journal of Solids and Structures*, vol. 46, no. 20, pp. 3694–3709, 2009.
- [23] C. Menna, F. Auricchio, and D. Asprone, “Chapter 13 - applications of Shape Memory Alloys in Structural Engineering,” in *Shape Memory Alloy Engineering* (L. L. Concilio, ed.), pp. 369 – 403, Boston: Butterworth-Heinemann, 2015.
- [24] D. Helm, “Numerical simulation of martensitic phase transitions in shape memory alloys using an improved integration algorithm,” *International Journal for Numerical Methods in Engineering*, vol. 69, no. 10, pp. 1997–2035, 2007.
- [25] I. Aerofit, “Shape Memory Alloy (SMA), Fluid Fitting System, Product Handbook and Engineering Data,” 2015.
- [26] G. Song, N. Ma, and H.-N. Li, “Applications of shape memory alloys in civil structures,” *Engineering Structures*, vol. 28, no. 9, pp. 1266–1274, 2006.
- [27] V. Torra, C. Auguet, A. Isalgue, G. Carreras, P. Terriault, and F. Lovey, “Built in dampers for stayed cables in bridges via SMA. The SMARTeR-ESF project: A mesoscopic and macroscopic experimental analysis with numerical simulations,” *Engineering Structures*, vol. 49, no. 0, pp. 43 – 57, 2013.
- [28] D. Lagoudas, D. Hartl, Y. Chemisky, L. Machado, and P. Popov, “Constitutive model for the numerical analysis of phase transformation in polycrystalline shape memory alloys,” *International Journal of Plasticity*, vol. 32–33, no. 0, pp. 155–183, 2012.

- [29] J. Arghavani, F. Auricchio, R. Naghdabadi, A. Reali, and S. Sohrabpour, “A 3D finite strain phenomenological constitutive model for shape memory alloys considering martensite reorientation,” *Continuum Mechanics and Thermodynamics*, vol. 22, no. 5, pp. 345–362, 2010.
- [30] D. Hartl, *Modeling of shape memory alloys considering rate-independent and rate-dependent irrecoverable strains*. PhD thesis, Texas A&M University, USA, December 2009.
- [31] C. Liang and C. Rogers, “A multi-dimensional constitutive model for shape memory alloys,” *Journal of Engineering Mathematics*, vol. 26, no. 3, pp. 429–443, 1992.
- [32] B. Raniecki and C. Lexcellent, “RL-models of pseudoelasticity and their specification for some shape memory solids,” *European Journal of Mechanics - A/Solids*, vol. 13, no. 1, pp. 21 – 50, 1994.
- [33] S. Leclercq and C. Lexcellent, “A general macroscopic description of the thermomechanical behavior of shape memory alloys,” *Journal of the Mechanics and Physics of Solids*, vol. 44, no. 6, pp. 953 – 980, 1996.
- [34] J. Boyd and D. Lagoudas, “A thermodynamical constitutive model for shape memory materials. part I. The monolithic shape memory alloy,” *International Journal of Plasticity*, vol. 12, no. 6, pp. 805–842, 1996.
- [35] B. Raniecki and C. Lexcellent, “Thermodynamics of isotropic pseudoelasticity in shape memory alloys,” *European Journal of Mechanics - A/Solids*, vol. 17, no. 2, pp. 185 – 205, 1998.
- [36] A. Souza, E. Mamiya, and N. Zouain, “Three-dimensional model for solids undergoing stress-induced phase transformations,” *European Journal of Mechanics - A/Solids*, vol. 17, no. 5, pp. 789 – 806, 1998.
- [37] M. Qidwai and D. Lagoudas, “Numerical implementation of a shape memory alloy thermomechanical constitutive model using return mapping algorithms,” *International Journal for Numerical Methods in Engineering*, vol. 47, no. 6, pp. 1123–1168, 2000.
- [38] M. Qidwai and D. Lagoudas, “On thermomechanics and transformation surfaces of polycrystalline NiTi shape memory alloy material,” *International Journal of Plasticity*, vol. 16, no. 10–11, pp. 1309 – 1343, 2000.

- [39] F. Auricchio, “A robust integration–algorithm for a finite-strain shape memory alloy superelastic model,” *International Journal of Plasticity*, vol. 17, no. 7, pp. 971–990, 2001.
- [40] P. Thamburaja and L. Anand, “Polycrystalline shape-memory materials: effect of crystallographic texture,” *Journal of the Mechanics and Physics of Solids*, vol. 49, no. 4, pp. 709–737, 2001.
- [41] C. Lexcellent, A. Vivet, C. Bouvet, S. Calloch, and P. Blanc, “Experimental and numerical determinations of the initial surface of phase transformation under biaxial loading in some polycrystalline shape–memory alloys,” *Journal of the Mechanics and Physics of Solids*, vol. 50, no. 12, pp. 2717–2735, 2002.
- [42] F. Auricchio and L. Petrini, “Improvements and algorithmical considerations on a recent three–dimensional model describing stress-induced solid phase transformations,” *International Journal for Numerical Methods in Engineering*, vol. 55, no. 11, pp. 1255–1284, 2002.
- [43] F. Auricchio and L. Petrini, “A three-dimensional model describing stress–temperature induced solid phase transformations: solution algorithm and boundary value problems,” *International Journal for Numerical Methods in Engineering*, vol. 61, no. 6, pp. 807–836, 2004.
- [44] F. Auricchio and L. Petrini, “A three–dimensional model describing stress–temperature induced solid phase transformations: thermomechanical coupling and hybrid composite applications,” *International Journal for Numerical Methods in Engineering*, vol. 61, no. 5, pp. 716–737, 2004.
- [45] D. Helm and P. Haupt, “Shape memory behaviour: modelling within continuum thermomechanics,” *International Journal of Solids and Structures*, vol. 40, no. 4, pp. 827 – 849, 2003.
- [46] P. Popov and D. Lagoudas, “A 3-D constitutive model for shape memory alloys incorporating pseudoelasticity and detwinning of self–accommodated martensite,” *International Journal of Plasticity*, vol. 23, no. 10–11, pp. 1679 – 1720, 2007. In honor of Professor Dusan Krajcinovic.
- [47] W. Zaki and Z. Moumni, “A three–dimensional model of the thermomechanical behavior of shape memory alloys,” *Journal of the Mechanics and Physics of Solids*, vol. 55, no. 11, pp. 2455 – 2490, 2007.

- [48] S. Reese and D. Christ, “Finite deformation pseudo–elasticity of shape memory alloys – constitutive modelling and finite element implementation,” *International Journal of Plasticity*, vol. 24, no. 3, pp. 455 – 482, 2008.
- [49] P. Thamburaja, “A finite–deformation–based phenomenological theory for shape–memory alloys,” *International Journal of Plasticity*, vol. 26, no. 8, pp. 1195 – 1219, 2010. Special Issue In Honor of Lallit Anand.
- [50] J. Arghavani, F. Auricchio, R. Naghdabadi, A. Reali, and S. Sohrabpour, “A 3–D phenomenological constitutive model for shape memory alloys under multi–axial loadings,” *International Journal of Plasticity*, vol. 26, no. 7, pp. 976 – 991, 2010.
- [51] J. Arghavani, F. Auricchio, R. Naghdabadi, A. Reali, and S. Sohrabpour, “A 3D finite strain phenomenological constitutive model for shape memory alloys considering martensite reorientation,” *Continuum Mechanics and Thermodynamics*, vol. 22, no. 5, pp. 345–362, 2010.
- [52] D. Hartl, G. Chatzigeorgiou, and D. Lagoudas, “Three-dimensional modeling and numerical analysis of rate-dependent irrecoverable deformation in shape memory alloys,” *International Journal of Plasticity*, vol. 26, no. 10, pp. 1485–1507, 2010.
- [53] J.-P. Teeriaho, “An extension of a shape memory alloy model for large deformations based on an exactly integrable eulerian rate formulation with changing elastic properties,” *International Journal of Plasticity*, vol. 43, no. 0, pp. 153–176, 2013.
- [54] S. Stupkiewicz and H. Petryk, “A robust model of pseudoelasticity in shape memory alloys,” *International Journal for Numerical Methods in Engineering*, vol. 93, no. 7, pp. 747–769, 2013.
- [55] R. Mirzaeifar, R. DesRoches, and A. Yavari, “Analysis of the rate–dependent coupled thermo–mechanical response of shape memory alloy bars and wires in tension,” *Continuum Mechanics and Thermodynamics*, vol. 23, no. 4, pp. 363–385, 2011.
- [56] C. Morin, Z. Moumni, and W. Zaki, “A constitutive model for shape memory alloys accounting for thermomechanical coupling,” *International Journal of Plasticity*, vol. 27, no. 5, pp. 748–767, 2011.

- [57] D. Grandi, M. Maraldi, and L. Molari, “A macroscale phase-field model for shape memory alloys with non-isothermal effects: Influence of strain rate and environmental conditions on the mechanical response,” *Acta Materialia*, vol. 60, no. 1, pp. 179–191, 2012.
- [58] S. Yang and G. Dui, “Temperature analysis of one-dimensional NiTi shape memory alloys under different loading rates and boundary conditions,” *International Journal of Solids and Structures*, vol. 50, no. 20–21, pp. 3254 – 3265, 2013.
- [59] M. Kojić, R. Slavković, M. Živković, and N. Grujović, *PAK-S: Program for FE Structural Analysis*. Faculty of Mechanical Engineering, University of Kragujevac, Kragujevac, 1999.
- [60] M. Kojić, R. Slavković, M. Živković, and N. Grujović, *PAK-T: Program for Heat Transfer Analysis*. Faculty of Mechanical Engineering, University of Kragujevac, Kragujevac, 1999.
- [61] H. Matthies, R. Niekamp, and J. Steindorf, “Algorithms for strong coupling procedures,” *Computer Methods in Applied Mechanics and Engineering*, vol. 195, no. 17–18, pp. 2028–2049, 2006. Fluid–Structure Interaction.
- [62] H. Matthies and J. Steindorf, “Partitioned strong coupling algorithms for fluid–structure–interaction,” informatikbericht, Institute of Scientific Computing, Technische Universit at Braunschweig, 2002.
- [63] R. Niekamp, *CTL Manual for Linux/Unix for the Usage with C++*. Institut fur Wissenschaftliches Rechnen – TU Braunschweig, Germany, 2005.
- [64] M. Kojić and K.-J. Bathe, *Inelastic Analysis of Solids and Structures*. Computational Fluid and Solid Mechanics, Berlin: Springer-Verlag Berlin and Heidelberg GmbH KG, 1st edition. ed., Dec. 2005.
- [65] A. Cuitiño and M. Ortiz, “A material-independent method for extending stress update algorithms from small-strain plasticity to finite plasticity with multiplicative kinematics,” *Engineering Computations*, vol. 9, no. 4, pp. 437–451, 1992.
- [66] K.-J. Bathe, *Finite Element Procedures*. Cambridge, MA: K.-J. Bathe, Feb. 2006.
- [67] G. Holzapfel, *Nonlinear Solid Mechanics. A continuum approach for engineering*. Chichester: J. Wiley and Sons, 2000.

- [68] M. Mićunović, *Primenjena mehanika kontinuuma*. Naučna knjiga, 1990.
- [69] J. Jarić, *Mehanika kontinuuma*. Gradjevinska knjiga, 1988.
- [70] M. Živković, *Nelinearna analiza konstrukcija*. Univerzitet u Kragujevcu, Mašinski fakultet, 2006.
- [71] R. Hill, “Aspects of invariance in solid mechanics,” vol. 18 of *Advances in Applied Mechanics*, pp. 1 – 75, Elsevier, 1979.
- [72] T. Brepols, I. Vladimirov, and S. Reese, “Numerical comparison of isotropic hypo- and hyperelastic-based plasticity models with application to industrial forming processes,” *International Journal of Plasticity*, vol. 63, no. 0, pp. 18 – 48, 2014. Deformation Tensors in Material Modeling in Honor of Prof. Otto T. Bruhns.
- [73] H. Xiao, O. Bruhns, and A. Meyers, “Elastoplasticity beyond small deformations,” *Acta Mechanica*, vol. 182, no. 0, pp. 31–111, 2006.
- [74] H. Xiao, O. Bruhns, and A. Meyers, “Logarithmic strain, logarithmic spin and logarithmic rate,” *Acta Mechanica*, vol. 124, no. 1-4, pp. 89–105, 1997.
- [75] H. Xiao, O. Bruhns, and A. Meyers, “On objective corotational rates and their defining spin tensors,” *International Journal of Solids and Structures*, vol. 35, no. 30, pp. 4001 – 4014, 1998.
- [76] J. Simo and M. Ortiz, “A unified approach to finite deformation elastoplastic analysis based on the use of hyperelastic constitutive equations,” *Computer Methods in Applied Mechanics and Engineering*, vol. 49, no. -, pp. 221 – 245, 1985.
- [77] E. Lee, “Elastic-plastic deformation at finite strains,” *Journal of Applied Mechanics*, vol. 36, no. 1, pp. 1–36, 1969.
- [78] D. Lagoudas, Z. Bo, M. Qidwai, and P. Entchev, “SMA–UM: User Material subroutine for thermomechanical constitutive model of shape memory alloys,” tech. rep., Texas A&M University, College Station, TX, 2003.
- [79] K. Tanaka, “A thermomechanical sketch of shape memory effect: Onedimensional tensile behavior,” *Res Mechanica*, vol. 18, pp. 251 – 263, 1986.
- [80] C. Liang and C. Rogers, “A multi-dimensional constitutive model for shape memory alloys,” *Journal of Engineering Mathematics*, vol. 26, no. 3, pp. 429–443, 1992.

- [81] L. Machado, *Shape Memory Alloys for vibration isolation and damping*. PhD thesis, Texas A&M University, USA, December 2007.
- [82] J. Simó and T. Hughes, *Computational Inelasticity*. Interdisciplinary applied mathematics: Mechanics and materials, Springer New York, 1998.
- [83] G. Weber and L. Anand, “Finite deformation constitutive equations and a time integration procedure for isotropic, hyperelastic–viscoplastic solids,” *Computer Methods in Applied Mechanics and Engineering*, vol. 79, no. 2, pp. 173 – 202, 1990.
- [84] D. Henann and L. Anand, “A large deformation theory for rate-dependent elastic–plastic materials with combined isotropic and kinematic hardening,” *International Journal of Plasticity*, vol. 25, no. 10, pp. 1833–1878, 2009.
- [85] M. Caminero, F. Montáns, and K.-J. Bathe, “Modeling large strain anisotropic elasto-plasticity with logarithmic strain and stress measures,” *Computers & Structures*, vol. 89, no. 11–12, pp. 826–843, 2011. Computational Fluid and Solid Mechanics 2011 Proceedings Sixth {MIT} Conference on Computational Fluid and Solid Mechanics.
- [86] J. Simo, “A framework for finite strain elastoplasticity based on maximum plastic dissipation and the multiplicative decomposition: Part i. continuum formulation,” *Computer Methods in Applied Mechanics and Engineering*, vol. 66, no. 2, pp. 199 – 219, 1988.
- [87] M. Kojić, R. Slavković, M. Živković, and N. Grujović, *Metod konačnih elemenata - Linearna analiza*. Kragujevac: Mašinski fakultet Kragujevac, Univerzitet u Kragujevcu, 1998. Serbian.
- [88] B. Schweizer and J. Wauer, “Atomistic explanation of the Gough-Joule-effect,” *The European Physical Journal B – Condensed Matter and Complex Systems*, vol. 23, no. 3, pp. 383–390, 2001.
- [89] P. Høakansson, M. Wallin, and M. Ristinmaa, “Comparison of isotropic hardening and kinematic hardening in thermoplasticity,” *International Journal of Plasticity*, vol. 21, no. 7, pp. 1435 – 1460, 2005.
- [90] A. Yeckel, L. Lun, and J. Derby, “An approximate block newton method for coupled iterations of nonlinear solvers: Theory and conjugate heat transfer applications,” *Journal of Computational Physics*, vol. 228, no. 23, pp. 8566–8588, 2009.

- [91] M. Maraldi, L. Molari, and D. Grandi, “A non-isothermal phase-field model for shape memory alloys: Numerical simulations of superelasticity and shape memory effect under stress-controlled conditions,” *Journal of Intelligent Material Systems and Structures*, vol. 23, no. 10, pp. 1083–1092, 2012.
- [92] P. Šittner, Y. Hara, and M. Tokuda, “Experimental study on the thermoelastic martensitic transformation in shape memory alloy polycrystal induced by combined external forces,” *Metallurgical and Materials Transactions A*, vol. 26, no. 11, pp. 2923–2935, 1995.
- [93] G. Weber, A. Lush, A. Zavaliangos, and L. Anand, “An objective time-integration procedure for isotropic rate-independent and rate-dependent elastic-plastic constitutive equations,” *International Journal of Plasticity*, vol. 6, no. 6, pp. 701 – 744, 1990.
- [94] P. Thamburaja, *Constitutive equations for superelasticity in crystalline shape-memory alloys*. PhD thesis, Massachusetts Institute of Technology, Cambridge, USA, October 2002.

Appendix A

Time integration procedure

In this appendix, the detail about the time - integration procedure for the rate independent phenomenological constitutive model are presented. By t is denoted the current time, Δt is the time increment.

Given : $\{ {}^t_0\mathbf{F}, {}^{t+\Delta t}_0\mathbf{F}, {}^t\zeta, {}^t\mathbf{e}_{tr}, {}^tT, {}^{t+\Delta t}T, {}^t\boldsymbol{\sigma}, {}^t\mathbf{b}^E \}$

Calculate : $\{ {}^{t+\Delta t}\boldsymbol{\sigma}, {}^{t+\Delta t}\zeta, {}^{t+\Delta t}\mathbf{e}_{tr}, {}^{t+\Delta t}\mathbf{b}^E \}$

The steps of the computation procedure:

Step 1. Calculate the trial deviatoric elastic strain ${}^{t+\Delta t}\mathbf{e}'_*$:

$${}^{t+\Delta t}\bar{\mathbf{b}} = {}^{t+\Delta t}\bar{\mathbf{F}} {}^{t+\Delta t}\bar{\mathbf{F}}^T.$$

$${}^{t+\Delta t}\bar{\mathbf{F}} = (\det {}^{t+\Delta t}\mathbf{F})^{-\frac{1}{3}} {}^{t+\Delta t}\mathbf{F} \quad {}^{t+\Delta t}\bar{\mathbf{F}} = (\det {}^{t+\Delta t}\mathbf{F})^{-\frac{1}{3}} {}^{t+\Delta t}\mathbf{F},$$

$${}^{t+\Delta t}\bar{\mathbf{b}}_*^E = {}^{t+\Delta t}\bar{\mathbf{F}} {}^t\bar{\mathbf{b}}^E {}^{t+\Delta t}\bar{\mathbf{F}}^T.$$

$${}^{t+\Delta t}\mathbf{e}'_*{}^E = {}^{t+\Delta t}\mathbf{h}_*{}^E = \frac{1}{2} \ln {}^{t+\Delta t}\bar{\mathbf{b}}_*^E = \sum_{k=1}^3 \ln \left({}^{t+\Delta t}\bar{\lambda}_{k*}{}^E \right) {}^{t+\Delta t}\mathbf{q}_k {}^{t+\Delta t}\mathbf{q}_k,$$

Step 2. Calculate the trial mean strain ${}^{t+\Delta t}e_m$ and the thermal strain ${}^{t+\Delta t}e_{th}$:

$${}^{t+\Delta t}e_m = \frac{1}{3} \ln [\det ({}^{t+\Delta t}\mathbf{F})]$$

$${}^{t+\Delta t}e_{th} = {}^{t+\Delta t}\alpha \Delta T$$

Step 3. The trial transformation strain:

$${}^{t+\Delta t}\mathbf{h} = \frac{1}{2} \ln {}^{t+\Delta t}\bar{\mathbf{b}} = \sum_{k=1}^3 \ln \left({}^{t+\Delta t}\bar{\lambda}_k \right) {}^{t+\Delta t}\mathbf{q}_k {}^{t+\Delta t}\mathbf{q}_k,$$

$${}^{t+\Delta t}\mathbf{e}_{tr*} = {}^{t+\Delta t}\mathbf{h} - {}^{t+\Delta t}\mathbf{h}^E,$$

Step 4. Calculate the trial deviatoric stress ${}^{t+\Delta t}\mathbf{S}'_*$ and the mean stress ${}^{t+\Delta t}\sigma_m$:

$$\begin{aligned} {}^{t+\Delta t}\mathbf{S}'_* &= 2{}^{t+\Delta t}G {}^{t+\Delta t}\mathbf{e}'_* \\ {}^{t+\Delta t}\sigma_m &= {}^{t+\Delta t}c_m \left({}^{t+\Delta t}e_m - {}^{t+\Delta t}e_{th} \right), \end{aligned}$$

Step 5. Calculate transformation function Φ :

$$\Phi = \begin{cases} H\bar{S} + \frac{1}{2} \left(\frac{1}{3}\bar{S}^2 \left(\frac{1}{G^M} - \frac{1}{G^A} \right) + 3\sigma_m^2 \left(\frac{1}{c_m^M} - \frac{1}{c_m^A} \right) \right) + 3\sigma_m (\alpha^M - \alpha^A) \Delta T + \\ \quad \rho \Delta s_0 (T - M_s) - \frac{\partial f(\xi)}{\partial \xi}; & \dot{\xi} > 0 \\ -\mathbf{S}'_* : {}^t\mathbf{e}_{tr*} \frac{H}{t\bar{e}_{tr}} + 3G\Delta\xi H^2 - \frac{1}{2} \left(\frac{1}{3}\bar{S}^2 \left(\frac{1}{G^M} - \frac{1}{G^A} \right) + 3\sigma_m^2 \left(\frac{1}{c_m^M} - \frac{1}{c_m^A} \right) \right) - \\ \quad 3\sigma_m (\alpha^M - \alpha^A) \Delta T - \rho \Delta s_0 (T - A_f) + \frac{\partial f(\xi)}{\partial \xi}; & \dot{\xi} < 0 \end{cases}$$

Step 6. If ${}^{t+\Delta t}\Phi^{(k)} \leq \textit{tolerance}$ then

$$\Delta\xi = 0$$

Solution is correct - go to step 11.

Step 7. Compute increment of martensitic volume fraction in iteration

$${}^{t+\Delta t}\Phi^{(k)} + d^{t+\Delta t}\Phi^{(k)} = {}^{t+\Delta t}\Phi^{(k+1)} = {}^{t+\Delta t}\Phi^{(k)} + \frac{\partial {}^{t+\Delta t}\Phi^{(k)}}{\partial \xi} d^{t+\Delta t}\xi^{(k)} \simeq 0$$

$$d^{t+\Delta t}\xi^{(k)} = -\frac{{}^{t+\Delta t}\Phi^{(k)}}{\frac{\partial {}^{t+\Delta t}\Phi^{(k)}}{\partial \xi}}$$

Step 8. The step increment of martensitic volume fraction and the current martensitic volume fraction are updated as follows:

$$\Delta {}^{t+\Delta t}\xi^{(k+1)} = \Delta {}^{t+\Delta t}\xi^{(k)} + d^{t+\Delta t}\xi^{(k)}; \quad {}^{t+\Delta t}\xi = {}^t\xi + \Delta {}^{t+\Delta t}\xi^{(k+1)}$$

Step 9. Update of the effective deviatoric stress:

$${}^{t+\Delta t}\bar{\mathbf{S}} = \begin{cases} {}^{t+\Delta t}\bar{\mathbf{S}}_* - 3{}^{t+\Delta t}GH\Delta^{t+\Delta t}\xi; & \dot{\xi} > 0 \\ \sqrt{{}^{t+\Delta t}\bar{\mathbf{S}}_*^2 - 6{}^{t+\Delta t}GH\Delta^{t+\Delta t}\xi \frac{{}^{t+\Delta t}\mathbf{S}'_* : {}^t\mathbf{e}_{tr}}{t\bar{e}_{tr}} + 9{}^{t+\Delta t}G^2H^2\Delta^{t+\Delta t}\xi^2}; & \dot{\xi} < 0 \end{cases}$$

Let $k = k + 1$ and go to the step 5.

Step 10. The deviatoric stress at the end of time step ${}^{t+\Delta t}\mathbf{S}'$:

$${}^{t+\Delta t}\mathbf{S}' = \begin{cases} \frac{{}^{t+\Delta t}\bar{\mathbf{S}}}{{}^{t+\Delta t}\bar{\mathbf{S}}_*} {}^{t+\Delta t}\mathbf{S}'_*; & \dot{\xi} > 0 \\ {}^{t+\Delta t}\mathbf{S}'_* - 2{}^{t+\Delta t}GH\Delta^{t+\Delta t}\xi \frac{{}^t\mathbf{e}_{tr}}{t\bar{e}_{tr}}; & \dot{\xi} < 0 \end{cases}.$$

Step 11. The total stress ${}^{t+\Delta t}\boldsymbol{\sigma}$ and the increment of the transformation strain at the end of time step are given as:

$${}^{t+\Delta t}\boldsymbol{\sigma} = {}^{t+\Delta t}\mathbf{S}' + {}^{t+\Delta t}\sigma_m \mathbf{I}; \quad {}^{t+\Delta t}\Delta \mathbf{e}_{tr} = \begin{cases} \frac{3H\Delta^{t+\Delta t}\xi}{2{}^{t+\Delta t}\bar{\mathbf{S}}} {}^{t+\Delta t}\mathbf{S}'_*; & \dot{\xi} > 0 \\ \frac{H\Delta^{t+\Delta t}\xi}{t\bar{e}_{tr}} {}^t\mathbf{e}_{tr}; & \dot{\xi} < 0 \end{cases}.$$

Step 12. Update of the left Cauchy-Green tensor ${}^{t+\Delta t}\bar{\mathbf{b}}^{-E}$

$${}^{t+\Delta t}\bar{\mathbf{b}}^{-E} = {}^{t+\Delta t}\bar{\mathbf{b}}_*^{-E} (\mathbf{I} - 2\Delta^{t+\Delta t}\mathbf{e}_{tr}).$$

Step 13. The update of transformation strain at the end of time step ${}^{t+\Delta t}\mathbf{e}_{tr}$:

$${}^{t+\Delta t}\mathbf{e}_{tr} = {}^{t+\Delta t}\mathbf{h} - {}^{t+\Delta t}\mathbf{h}^E,$$

где je:

$${}^{t+\Delta t}\mathbf{h}^E = \frac{1}{2} \ln {}^{t+\Delta t}\bar{\mathbf{b}}^{-E}.$$